MODELING AND APPLICATIONS OF HEAT TRANSFER IN WELLBORE AND ITS SURROUNDING FORMATION

A Dissertation

by

BOYUE XU

Submitted to the Office of Graduate and Professional Studies of
Texas A&M University
in partial fulfillment of the requirements for the degree of

DOCTOR OF PHILOSOPHY

Chair of Committee,	A. Rashid Hasan
Committee Members,	Ibere Alves
	Hadi Nasrabadi
	M.M. Faruque Hasan
Head of Department,	Jeff Spath

May 2019

Major Subject: Petroleum Engineering

ABSTRACT

The development of underground oil and gas resources involves significant heat transfer between fluid, downhole tubulars and the surrounding formation. Understanding the heat transfer between wellbore and the surrounding formation has significant impacts for all thermal related operations. Different engineers need to understand the heat transfer for different purposes: drilling engineers need to know the temperature profiles in the wellbore during drilling mud circulation for drilling mud properties variance; reservoir engineers need to know the fluid temperature distribution in the reservoir; production engineers need to know the temperature profiles in the wellbore for downhole equipment efficiency and flow assurance purposes. Studying the heat transfer during drilling, completion and reservoir development periods are necessary and challenging. Usually the "rule-of-thumb" value or complicated numerical simulation is either not reliable or impractical.

This research studies the heat transfer during drilling, completion and reservoir development periods. Specifically, it includes four parts: (1) the temperature profiles during drilling circulation (2) transient temperature behavior during clean-up period (3) fluid nonisothermal behavior during reservoir development, and (4) fluid flow in the wellbore during production. All the models are solved either fully analytically or semi-analytically with several reasonable assumptions and provide engineers an easy way to estimate and make quick decisions. This research concentrates on offshore assets due to their complication since heat transfer is occurring in between the wellbore and the positive surrounding temperature gradient (formation) and the negative surrounding temperature gradient (seawater). A real offshore well is used to illustrate the approach.

In addition, this research also applied the heat transfer between the wellbore and the formation to geothermal resource recovery. Abandoned oil wells can be further recompleted as a closed-loop heat exchanger for underground geothermal resource recovery. This engineering operation not only minimizes the cost associated with drilling a new well, but also avoids the pollution associated with drilling and completion. Three different models are proposed and compared: a fully analytical model, a semi-numerical model and a fully numerical model. The research found that the fully analytical model is an ideal choice for designing and optimizing geothermal energy recovery from abandoned oil wells.

DEDICATION

This work is dedicated to my family, friends and advisor. I appreciate their help and support since my studying at Texas A&M.

ACKNOWLEDGEMENTS

I would like to thank my advisor, Dr. Rashid Hasan for his guidance and kind help in both my research and life in Texas A&M. I also appreciate Metrol UK for their funding support. Additionally, I wish to thank David Fyfe of Metrol for his interest in my research project, explanations of Metrol sensors, and for offering field data.

Thanks to my committee members: Dr. Ibere Alves, Dr. Hadi Nasrabadi and Dr. Farugue Hasan. I really appreciate their invaluable advice and help.

Thanks also go to my friends and colleagues and the department faculty and staff in Petroleum Engineering Department for making my time at Texas A&M University a great experience.

Last but not the least, thanks to my wife Yang Xu for her sacrifice; thanks to my parents for their love; thanks to my daughter Vicky Xu for her smile.

CONTRIBUTORS AND FUNDING SOURCES

This work was supported by a dissertation committee consisting of Professor Rashid Hasan, Ibere Alves and Hadi Nasrabadi of the Department of Petroleum Engineering, Professor Farugue Hasan of the Department of Chemical Engineering.

The work in Chapter 7 was collaborated with Hewei Tang of the Department of Petroleum Engineering in Texas A&M University.

All other work conducted for the dissertation was completed by Boyue Xu independently.

Graduate study was supported by research funding from Metrol UK as well as teaching assistantship from Texas A&M University.

NOMENCLATURE

A	pipe area, ft^2
B_o	oil-formation volume factor, RB/STB
B_g	gas formation volume factor, Mscf/STB
c_p	specific heat capacity, Btu/lbm-°F
c_t	total compressibility, psi^{-1}
C_{JT}	Joule-Thomson coefficient, °F/ft
d	diameter, ft
d_e	equivalent diameter, ft
f	friction factor, dimensionless
g	gravitational acceleration, ft s^{-2}
g_c	conversion factor, 32.17 (lbm-ft)/lbf-s^2
g_G	surrounding temperature gradient, °F/psi
h	formation thickness, ft
h_c	heat transfer coefficient of the reservoir, Btu/hr.ft^2.°F
h_f	convective heat-transfer coefficient, Btu/hr.ft^2.°F
H	enthalpy, BTU/lbm
$\dot{H}$	heat transfer rate with over- and under-, Btu/hr/ ft^2
J	conversion factor, 778 (ft-lbf)/Btu
k	reservoir permeability, md
K	thermal conductivity, Btu/(hr.ft.°F)
L_w	water depth, ft

L_R	relaxation parameter, hr^{-1}
m_a	affected formation mass, lbm
m(p)	pseudopressure, psi
P	pressure, psi
P_r	prandtl number, dimensionless
q_m	drilling mud circulating rate, gallon/min
q	volumetric flow rate, ft^3/hr
Q	heat flow rate, Btu/hr
Q_F	heat flow between formationand wellbore, Btu/hr
r	radius, ft
r_d	dimensionless radius, dimensionless
r_a	affected formation radius, ft
r_e	external reservoir radius, ft
R_e	Reynolds number, dimensionless
t_c	circulation time, hr
R	ideal gas-law constant, J/(kg·°K)
s	Laplace transform variable, dimensionless
s_f	reservoir fluid saturation, dimensionless
S	saturatuion, dimensionless
t	time, hr
t_D	dimensionless time, dimensionless
t_r	relaxation time, hr
T	temperature, °F

T_a	annulus fluid temperature, °F
T_{dp}	drill pipe fluid temperature, °F
T_{fe}	reservoir fluids existing temperature, °F
T_{ea}	average near wellbore formation temperature, °F
T_D	dimensionless temperature, dimensionless
T_{ei}	undisturbed formation temperature, °F
T_{inj}	injecting/inlet temperature, °F
T_s	surrounding surface static temperature, °F
TVD	True Vertical Depth, ft
u	fluid velocity, ft/hr
U	overall heat-transfer coefficient, Btu/hr.ft^2.°F
V	specific volume, ft3/lbm
w	mass flow rate, lbm/hr
x	viscosity coefficient in two-steps calculation, dimensionless
z	wellbore depth, ft
z_L	wellbore total depth, ft
Z	gas compressibility factor, dimensionless
η	thermal diffusivity, ft^2/hr
α	well inclination angle, degree
β	volume expansion coefficient, $^oF^{-1}$
μ	viscosity, cp
ϕ	formation porosity, dimensionless
ρ	density, lbm/ft^3

σ	fluid J-T throttling coefficient, Btu/lbm-psi
ε	pipe absolute roughness, ft

Subscripts

a	annulus
c	casing
ci	casing inside
co	casing outside
cem	cementing
dp	drill pipe
dpi	drill pipe inside
dpo	drill pipe outside
e	formation
f	fluid
g	gas
i	injecting
ins	insulation
ID	inside diameter
m	drilling mud
ml	mudline
o	oil
OD	outside diameter
p	producing

ti	tubing inside
to	tubing outside
s	seawater
wb	wellbore formation interface

TABLE OF CONTENTS

Page

LIST OF FIGURES

Page

LIST OF TABLES

1. INTRODUCTION AND OBJECTIVES

1.1 Background

To meet the energy demand all over the world, the petroleum industry is exploring in deepwater and ultra-deepwater environment. Global offshore oil production has reached 28 million barrels per day in 2015, which is about 30% of global crude oil production, shown in Figure 1 (EIA, 2016). The global offshore production can be classified by water depth: shallow water in the shelf (up to 125 meters); deepwater with water depth in between 125 m and 1,500 m; and ultra-deepwater with more than 1,500 m water depth. The global offshore production by water depth from 2005 to 2015 is shown in Figure 2 (EIA, 2016). United States and Brazil are the leading countries in developing ultra-deep assets and account for more than 90% of global offshore production (EIA, 2016). The capital cost of a deepwater project is huge. Affected by the downturn in oil price since 2014, many deepwater projects have been stopped. It is hard to develop deepwater asset at low oil price environment. As the oil price is recovered to 70 $/bbl in 2018, the deepwater project becomes more active.

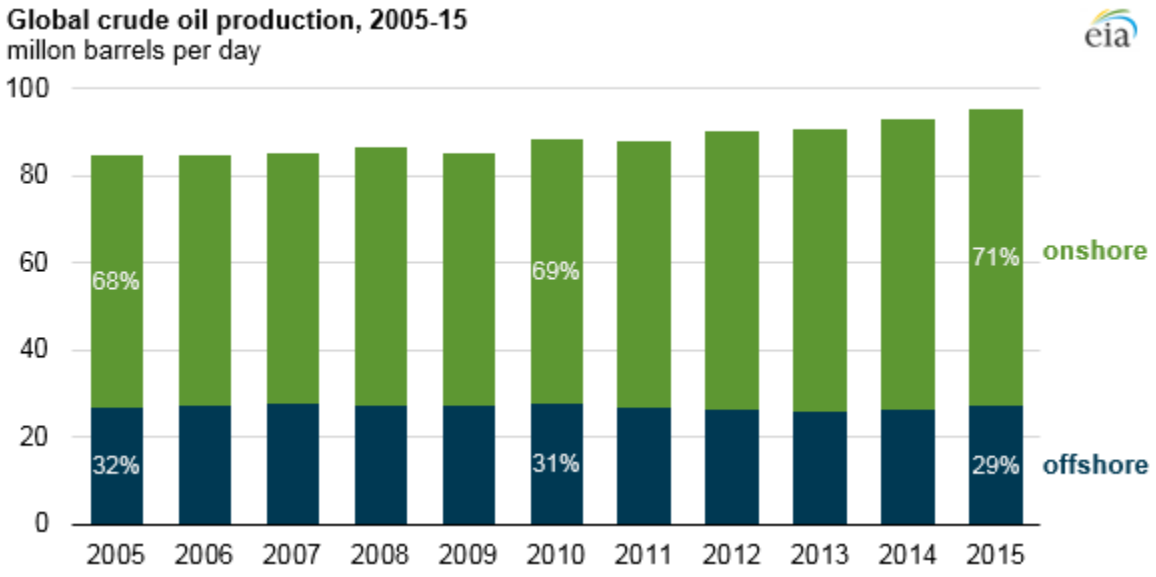

Figure 1-Global crude oil production from 2005 to 2015 (reprinted from EIA, 2016)

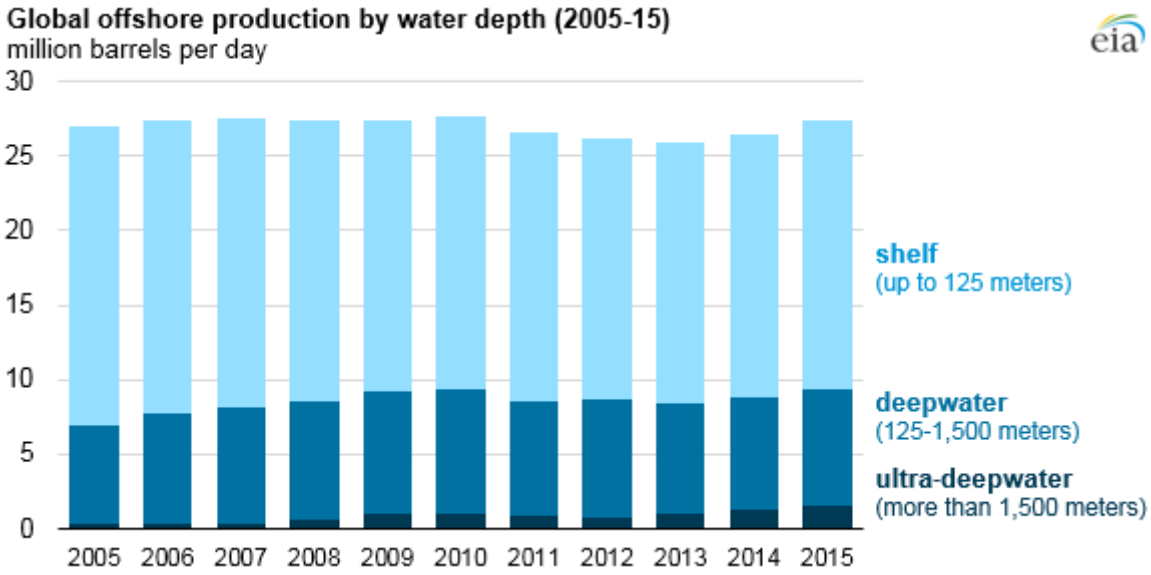

Figure 2-Global crude oil production by water depth from 2005 to 2015 (reprinted from EIA, 2016)

1.2 Statement of the problem

It is necessary to better understand the heat transfer during the development of a deepwater project since it is highly related to safety issues, which is always the most important factor of a deepwater project. Understanding the heat transfer between wellbore and surrounding formation/seawater is one of the important factors for the success of a deepwater asset development. During deepwater drilling circulation, the changes of fluid temperature during circulation will alter fluid properties, such as viscosity and density. A specific drilling fluid formula should be prepared for a given temperature range; otherwise it may lose its functions and cause serious problems (Bourgoyne et al., 1986). The drilling fluid temperature also has an influence on gas solubility, which should be determined for gas kick detection purpose (Thomas et al., 1984; Feng et al., 2016). Deepwater drilling may encounter a hydrate prone zone. If the temperature is above the hydrate equilibrium temperature, the hydrate dissociation will happen. It may cause wellbore instability, gas kick, blowout-preventer (BOP) lock and even blowout disaster (Gao et al., 2017). Also, hydrate may be formed near the mudline and block the circulation path. The design and selection of drill pipe, casing, cementing and drill bit all require an estimation of drilling fluid temperature since the metal thermal stress is highly dependent on the temperature (Wong and Yeung, 2006; Wooley, 1980; Maruyama et al., 1990). In addition to the points mentioned above, understanding the temperature is important to cementing design and accurate estimation of setting time and logging tool design and interpretation (Hasan, 2018).

The heat transfer between wellbore and formation not only causes the drilling fluid temperature variance along its circulation path, but also alters the near wellbore formation temperature. Edwardson et al. (1962) evaluated the temperature disturbances produced by circulation drilling mud. They found that temperature disturbance caused by drilling circulation is

within 10 ft beyond the wellbore. After drilling circulation, the target zone is perforated and warmer reservoir fluid flows though the cooled near wellbore formation, enters the wellbore at a lower temperature than that of the undisturbed formation. The near wellbore formation gets gradually heated back by the warmer reservoir fluid. Temperature changes in the near wellbore formation needs to be estimated so that useful interpretation can be made. For example, the fluid flow rate estimation during clean-up period is possible given the MDTS (Multi-Distributed Temperature Sensors) measured temperature data.

For deepwater assets with high rates and large consequent drawdown reservoirs, the nonisothermal in the reservoir becomes the norm due to the Joule-Thomson (J-T) effect. Other factors, such as a fluid's adiabatic expansion (AE), heat convection, and the heat exchange with surrounding formations may also make contributions. Accounting for this nonisothermal flow behavior becomes a necessity for accurately estimating a well's performance due to changes in fluid properties and also from the standpoints of wellbore mechanical integrity. As the reservoir fluid is flowing into the wellbore, the hydrocarbon is produced to the surface through the wellbore. Presence of seawater in the riser adds complexity to the heat transfer process in the offshore environment. During production, the hot fluid continues to lose heat to the increasingly cold surroundings as it ascends the borehole. The temperature difference between the wellbore fluid and the formation causes the heat transfer from fluid to its surroundings. When reservoir fluid is produced, the sandface temperature is not always the same as that of the formation. When large drawdown happens, it will precipitate a temperature increase or decrease. In this situation, fluid temperature at the sandface may be estimated from the knowledge of nonisothermal fluid flow in the reservoir.

1.3 Research objectives

Heat transfer occurs between fluid, downhole tubulars, and surrounding formation during the whole development process: drilling circulation, fluid flowing in the reservoir, and fluid producing in the wellbore. The objective of this research is to study heat transfer during deepwater drilling, completion and development periods. In addition, we want to apply the heat transfer to the area of geothermal recovery from abandoned oil well. Figure 3 illustrates the working steps in this research.

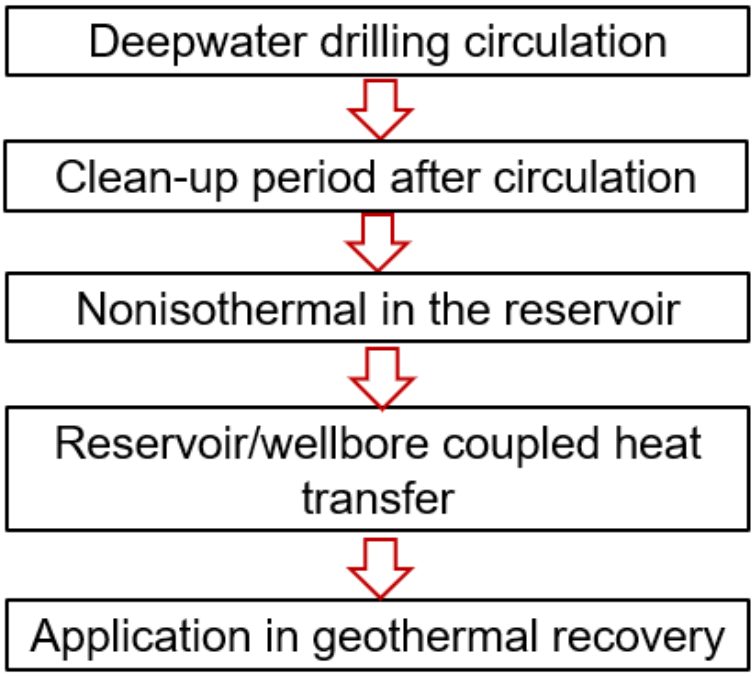

Figure 3-Working steps in this research

1.4 Outline of the dissertation

This dissertation has 8 chapters. Chapter 1 introduces the problems and research objectives. Chapter 2 presents the literature review related to this research for readers to better understand previous work and innovations of this research. Chapter 3 describes the heat transfer during deepwater drilling circulation. An analytical solution to estimate fluid temperature in the drill pipe

and annulus are derived. Chapter 4 studies the transient temperature behavior during clean-up period and proposed a novel method to estimate flow rates across the perforation zone with given MDTS data. Chapter 5 presents the nonisothermal fluid flow heat transfer model in the reservoir. Model validation, sensitivity studies and a simplified two-steps calculation method are discussed. Chapter 6 discussed a classic heat transfer model in the wellbore and coupled it with the reservoir heat transfer model in Chapter 5. Chapter 7 gives three mathematical models to describe geothermal recovery from abandoned oil well. Chapter 8 summaries this research and makes the conclusions.

2. LITERATURE REVIEW

2.1 Deepwater drilling circulation heat transfer

The circulation temperature during deepwater drilling is complicated by the transient temperature behavior and heat transfer between wellbore and surroundings. The transient temperature behavior has been studied by many researchers. The pioneer model to estimate injecting fluid temperature was by Ramey (1962). Ramey presented a simple time dependent function to describe the transient temperature behavior between formation and wellbore. Horne and Shinohara (1979) presented a transient heat transfer model to estimate heat-loss of production and injecting wells by modifying Ramey's model. Hagoort (2004) pointed out that Ramey's approximation overestimated the temperature during early transient period. Hagoort also gave a graphical correlation to estimate the length of this early transient period. Hasan and Kabir (1994) presented an approximate solution to fit transient temperature behavior from moderate to later periods. For later transient periods, the approximation is the same as Ramey's solution. Instead of assuming constant rate at wellbore formation interface, Kutasov (1989) gave a solution to estimate transient wellbore temperature by assuming a line source solution could represent the well. Wu et al. (2015) proposed a semianalytical solution to estimate transient temperature along the wellbore after the well shut-in. In general, two approaches were used to estimate circulation drilling fluid temperature. In numerical efforts, Raymond (1969) first presented a numerical model to estimate circulating fluid temperature during both unsteady-state and pseudosteady-state for onshore well. Raymond found that after one or two circulation trips, the temperature inside the wellbore tends to be stable. Schoeppel and Bennett (1971) developed a transient numerical simulator for circulation fluid and formation temperature. Their model assumed that forced heat convection in

the wellbore and heat conduction in the adjacent formation. Later, Keller et al. (1973), Wooley (1980) and Beirute (1991) improved the work and gave numerical models to calculate the temperature profile during drilling circulation. Recently, Gao et al. (2017) numerically coupled the wellbore and formation by assuming steady-state heat transfer inside the wellbore and transient temperature in the formation to estimate offshore drilling circulation temperature numerically. Li et al. (2017) set up a transient energy balance inside the wellbore for drilling circulation system in deepwater by assuming constant injecting temperature at the mudline. In analytical efforts, Holmes and Swift (1970) presented a steady-state heat transfer model to determine circulating fluid profile in the drill pipe and annulus. Oster and Scheffler (1976) presented a quasi steady-state model to determine temperature distribution when aquifers are present in the formation. Durrant and Thambynayagam (1986) presented an iteration approach to estimate fluid temperature in the wellbore during upward/downward fluid circulation. The transient model was solved by successive Fourier and Laplace transformations. Hasan et al. (1996) developed an analytical model to estimate forward/reverse circulation fluid temperature as a function of depth and circulation time for onshore well. However, no further studies were spent on deepwater drilling and its effect on near wellbore formation temperature disturbance.

2.2 Intelligent completion: Multi-Distributed-Temperature-Sensor (MDTS)

The widely accepted definition of intelligent completion is a system capable of remote monitor and control the reservoir and production process (Robinson, 2003). To provide remote monitor and control function, the system should be able to collect, transmit, store and analyze the downhole data. The intelligent completion was introduced to oil and gas industry since 1980s. With the fast development since 2000s, modern intelligent completion system primary consists of downhole inflow control valves (ICVs), zonal isolation packers, pressure and temperature sensors,

electric cables and surface data acquisition system. Now, most offshore operators have accepted intelligent completion as part of regular wellbore design to better monitor and control of downhole activities because the well intervention cost is huge in offshore wells (Imomoh, 2013). In addition, intelligent completion can increase hydrocarbon production by commingling production from multi zones. It enables selective zonal control, thus increase the efficiency of reservoir development (Konopczynski et al., 2002). Another attractive point is that intelligent completion provides millions of real-time downhole pressure and temperature data, which provides better understanding of the reservoir characteristic (Duru and Horne, 2010).

Multi distributed temperature sensor (MDTS) one of the key important parts of intelligent completion. It permits a continuous high-resolution temperature measurement across the target interval in a high frequency. Horne (2007) reported that 32 million data points were collected per year. The real-time temperature profiles can be monitored at surface and avoid the time-consuming production logs and reduce operation costs. MDTS can be deployed on perforating guns, tubing, casing, or sand screens. The conventional MDTS use fiber-optic technology to transmit the data. In recent years, wireless MDTS was introduced to the industry and applied. It is constructed with multiple discrete temperature sensors enclosed within a control line and attached to a memory processor that time stamps and transmits the data. The telemetry relay station has memories and temperature recording ability. It is able to work up to 25, 000 psi and 377 ^{o}F condition and record up to 2 million data sets (Metrol, https://www.metrol.co.uk/pages/products/paragon). These advanced electrical tools provide engineers tons of data, which were impossible in old days. However, how to utilize these data are still a challenge and requires rigorous modelling and analysis. Duru and Horne (2010) proposed a method to estimate the porosity and permeability by using history matching with MDTS measured transient data. Wu et al. (2015) presented a semi-

analytical model to estimate single phase oil transient temperature after the well shut-in, however, they did not consider the superposition effect. Hashmi et al. (2015) estimated a gas well production rate and permeability by the proposed transient temperature model with/without superposition effects. Tardy et al. (2012), Li et al. (2011) and Zayed et al. (2017) have demonstrated the use of downhole temperature measurement for zonal contribution estimations. Recently, Ribeiro and Horne (2016), Zhang et al. (2017) and Zhu et al. (2018) extended the application of downhole temperature data to diagnose the fracture performance and treatment.

2.3 Fluid flow and heat transfer in the reservoir

Most analytical and numerical flow modeling presupposes isothermal flow behavior in the reservoir. Although fluid enthalpy depends on both temperature and pressure, most reservoir engineering computations ignore the pressure component of enthalpy because the Joule-Thompson (J-T) coefficient, C_{JT}, is orders of magnitude smaller than the fluid specific heat, c_p. Therefore, early investigators ignored the J-T effect when estimating reservoir fluid temperature in thermal recovery operations. The studies of Lauwerier (1955), Rubenstein (1959), Avdonin (1964a, b), Spillette (1965), and Satman et al. (1979) are cases in point. The nonisothermal behavior has been studied by several researchers. App (2009, 2010) developed a transient numerical reservoir simulator for single-phase oil flow that included the J-T effect, AE effect, and heat exchange with the over- and under-burden formations. Subsequently, App and Yoshikawa (2013) offered an analytical solution for steady-state flow for the same problem. Ramazanov et al. (2010) derived an analytical solution for the reservoir temperature by using the method of characteristics to solve the partial differential equation. Muradov and Davies (2012a, 2012b) presented fully analytical solutions to estimate reservoir temperature distribution for producing horizontal wells. The transient temperature behavior in hydraulic fractures are also considered in their models. More

recently, Onur and Cinar (2017) presented a transient analytical solution that accounts for the J-T effect and AE expansion, but neglected heat exchange with over- and under-burden formations. Also, Onur and Palabiyik (2015) and Mao and Zeidouni (2017) offered similar solutions that included near wellbore damage but also excluded fluid's heat exchange with the over- and under-burden formations. In this context, Chevarunotai et al. (2015) showed that significant error in estimated temperature might be incurred if heat exchange between over- and under-burden formations is neglected, especially at high production rates. They offered an analytical solution for transient oil temperature that includes the J-T effect, and heat exchange with the over- and under-burden, but excluded the AE effect.

2.4 Geothermal recovery heat transfer models

In the area of geothermal recovery, the basic ideal is same as the drilling circulation except that cold fluid is injected through annulus and flowing upward in the tubing. Geothermal energy is regarded as a possible supplement to fossil fuels because of its abundance and renewable nature (Gupta and Roy, 2006; Sayigh, 1999). It has been exploited for space heating and electricity generation since the beginning of the 20^{th} century. Electricity generated from geothermal energy sources has expanded 7 times from 1975 to 2010, and is expected to reach 16,000 Mwe by 2020 (Bertani, 2012; Gallup, 2009). It is also a common practice to directly use the geothermal energy for space heating in areas that suffer from severe air pollution generated by fossil fuels (Guo et al. 2017). Hydraulic stimulation technology is commonly applied to exploit geothermal energy from Hot Dry Rock (HDR) (Huenges and Ledru, 2011). However, the cost associated with drilling and hydraulic fracturing is huge, and the extraction and recharge of ground water raise environmental issues (Barbier, 2002). To avoid these issues, high geothermal gradient abandoned oil wells have been proposed to recomplete as double-pipe heat exchangers to produce geothermal energy (Cheng

et al., 2013; Cheng et al., 2014; Davis and Michaelides, 2009; Bu et al., 2012). Instead of producing groundwater, the closed-loop, recompleted oil well technology only extracts heat from the formation, saving drilling cost and avoiding environmental issues. Huabei oilfield in China has designed an organic Rankine cycle (ORC) system to generate electric power by using geothermal heat from abandoned wells (Yang et al., 2017). Closed-loop, recompleted oil well technology to extract heat from formation requires rigorous modeling. Many researchers have made modeling efforts, with Kujawa et al. (2006) being the first to present the idea for the Jachowka-K2 well. Their study showed that geothermal exploration using abandoned wells as double-pipe heat exchangers may be feasible. Kujawa et al. (2006) analytically solved heat transfer between the formation and the wellbore fluid. However, they unrealistic assumed that perfect insulation between injecting and producing pipes. Davis and Michaelides (2009) proposed a model to estimate power produced from abandoned wells with isobutene as the working fluid. They numerically solved steady-state mass and energy balance equations in wellbore and assumed the formation temperature to be constant. Bu et al. (2012) presented a model that numerically solves transient energy balances in both wellbore and surrounding formation. The model assumes unchanging fluid properties. Their simulation results indicated that the fluid injecting rate and geothermal gradient are key parameters for geothermal energy production. Templeton et al. (2014) proposed a two-dimensional transient heat transfer model for the geothermal well and compared it with models proposed by other researchers. Their simulation indicated that Dittus-Boelter correlation overestimates convective heat transfer in the annulus. Cheng et al. (2013) built a model that numerically solved transient energy balance in wellbore. Their results indicated the existence of an optimal injecting rate for maximum net power and outlet temperature. Nian and Cheng (2018) further applied the model to analyze formation temperature recovery after heating periods. The

model solved transient formation energy balance analytically by assuming constant heat flow rate at the wellbore formation interface. Cui et al. (2017) proposed to produce geothermal energy using horizontal wells to extend the contact area of the working fluid and the formation. They numerically solved transient energy balance equations in wellbore and formation assuming that fluid properties do not change with space and time. They performed sensitivity studies with economic analysis to estimate the optimal lateral length. Some other researchers used either in-house code or commercial simulators to estimate the fluid temperature distribution in a closed loop system (Alimonti et al., 2018). The summary of the models is shown in Table 1.

Reference	Reservoir model	Wellbore model
Kohl et al. (2002)	FRACTure	FRACTure
Nalla et al. (2005)	TETRAD/GEOTEMP	TETRAD/GEOTEMP
Kujawa et al. (2006)	Analytical model	Analytical model
Wang et al. (2009)	AUTOUGH2	Numerical model
Davis and Michaelides (2009)	Numerical model	Numerical model
Cheng et al. (2013, 2014)	Analytical model	Analytical model
Cei et al. (2013)	Tough2/Analytical model	/
Taleghani et al. (2013)	FlexPDE	FlexPDE
Akhmadullin and Tyagi (2014)	/	Simulink
Feng et al. (2015)	Cactus	Numerical model
Galoppi et al. (2015)	Fluent	Numerical model
Le Lous et al. (2015)	Feflow	Feflow
Noorollahi et al. (2015)	ANSYS	ANSYS
Sliwa et al. (2015)	BoHEx	BoHEx
Alimonti and Soldo (2016)	Analytical model	Numerical model

Table 1-Literature reviews of different reservoir and wellbore heat transfer models in geothermal recovery (Modified after Alimonti et al., 2018)

3. DEEPWATER DRILLING CIRCULATION HEAT TRANSFER

3.1 Model development

The physical process of deepwater drilling and heat transfer is illustrated in Figure 4. The drilling fluid is pumped into the wellbore at the platform through the drill pipe. Initially, the drilling fluid in the drill pipe is losing heat to the surrounding cold seawater. As the drilling fluid is circulating deeper into the formation, it starts to gain heat from the surrounding hot formation. At the bottomhole, the fluid temperature in the drill pipe reaches its maximum due to the large amount of heat received from the surrounding formation. In return, the near wellbore formation temperature is cooled by the drilling fluid. Then, the drilling fluid flows upward through the annulus. The annulus fluid continuously receives heat from the hot formation, but also loses heat to the drill pipe. As the annulus fluid is reaching the seawater portion, it begins to lose heat to the surrounding seawater. However, it may gain or lose heat from/to the "fresh" injected drilling fluid in the drill pipe. Gaining or losing heat depends on the temperature difference between fluid temperature in the annulus and drill pipe. The heat transfer process during deepwater drilling can be summarized as: drilling fluid is carrying heat from deep hot formation and losing heat to the cold seawater.

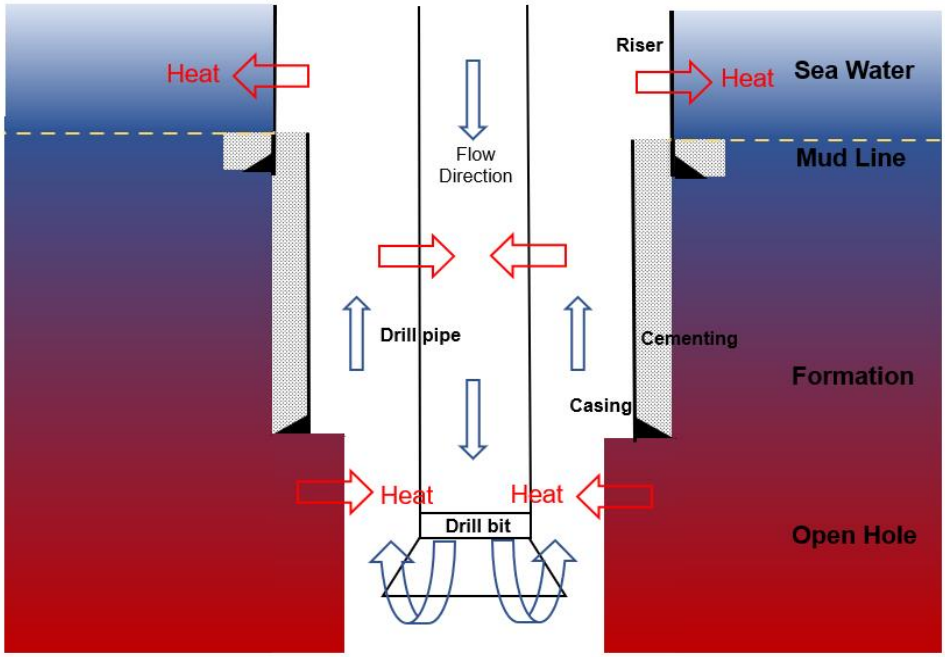

Figure 4-Deepwater drilling process and heat transfer

To set up the mathematical model, we make the following assumptions:

- Geothermal temperature is a known function of depth in both seawater and formation.
- Transient heat transfer in the formation; steady-state heat transfer in the wellbore.
- Constant formation and wellbore thermal properties.
- No wellbore heat storage effect.
- Ignore friction induced heat.
- No mud filtration loss.

Figure 5 presents the schematic of a control volume indicating fluid flow and heat transfer in a fluid circulating system, using the depth coordinate, *z*, to be positive in the downward direction. An energy balance is set up between the convective heat transfer in the drill pipe with the energy

accumulation and heat flow to the annulus. For the annulus, convective heat transfer and energy accumulation was balanced with heat transfer between drill pipe fluid and formation. These energy balances can be expressed as Eq. 1 and Eq. 2:

In the drill pipe:

$$Q_{dp}(z) - Q_{dp}(z + dz) = -Q_{ta} \tag{1}$$

In the annulus:

$$Q_a(z + dz) - Q_a(z) = Q_{ta} - Q_F \tag{2}$$

Where, Q_{ta} represents the heat flow rate between the drill pipe and annulus, Q_F represents the heat flow rate between the formation and the wellbore. The following governing equation is derived to describe the heat transfer during deepwater drill circulation:

$$\frac{B}{L_R}\frac{d^2T_{dp}}{dz^2} - B\frac{dT_{dp}}{dz} - T_{dp} + T_s + g_G z = 0 \tag{3}$$

$$T_a = T_{dp} + B\frac{dT_{dp}}{dz} \tag{4}$$

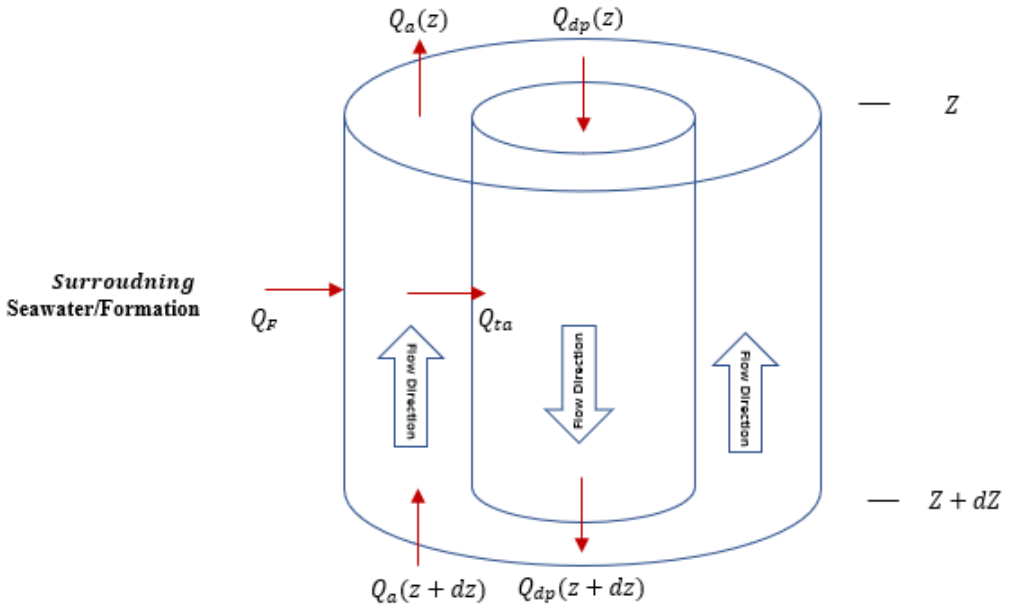

Figure 5-Schematic of fluid flow and heat transfer to set up energy balance in drill pipe and annulus

The general solutions of Eq. 3 and Eq. 4 are expressed as

$$T_{dp} = \alpha e^{\lambda_1 z} + \beta e^{\lambda_2 z} + g_G z - B g_G + T_s \tag{5}$$

$$T_a = (1 + \lambda_1 B)\alpha e^{\lambda_1 z} + (1 + \lambda_2 B)\beta e^{\lambda_2 z} + g_G z + T_s \tag{6}$$

The heat loss between the wellbore and the undisturbed formation is:

$$Q = c_{pm} L_R (T_{ei} - T_a) \tag{7}$$

Where T_{dp} is the fluid temperature in the drill pipe, T_a is the fluid temperature in the annulus, g_G is the temperature gradient of the surroundings while T_s is the surrounding surface static temperature. L_R and B are heat transfer coefficient related parameters, α, β, λ_1 and λ_2 are coefficients dependent on boundary conditions and surrounding thermal properties. Treating seawater and formation portions separately, the fluid temperature in the drill pipe and annulus are continuous.

In other words, the drill pipe/annulus fluid temperatures at the mudline are the same in both the seawater portion and the formation portion. An iteration approach is used to estimate the temperature in both the seawater and formation portions. The detailed derivations and the calculation approach are described in Appendix A.

3.2 Field case study

Well A is a subsea gas well in deepwater environment. The related formation, fluids and tubular properties are shown in Table 2. This offshore well has a total vertical depth (TVD) of 13412 ft and includes 5118 ft seawater. The wellbore geometry is summarized in Table 3.

Parameter	Value	Unit
Seawater Surface Temper.	60	^{o}F
Seawater Bottom Temper.	35	^{o}F
Formation Temperature Grad.	0.0124	^{o}F/ft
Formation Thermal Conduc.	1.6	Btu/(hr-ft-^{o}F)
Formation Specific Density	2.65	/
Formation Specific Heat	0.24	Btu/(lb-^{o}F)
Tubing Thermal Conduc.	25	Btu/(hr-ft-^{o}F)
Casing Thermal Conduc.	25	Btu/(hr-ft-^{o}F)
Cementing Thermal Conduc.	1.4	Btu/(hr-ft-^{o}F)
Mud Thermal Conduc.	0.42	Btu/(hr-ft-^{o}F)
Mud Specific Heat	0.94	Btu/(lb-^{o}F)
Mud Density	1.2	/
Mud Effective Viscosity	15	cp
Mud Flow Rate	600	gpm
Mud Injecting Temperature	60	^{o}F
Drill Circulation Time	24	hours
Formation Fluid Density	0.601	/
Formation Fluid Specific Heat	0.78	Btu/(lb-^{o}F)

Table 2-Related formation, fluids and tubulars properties

Parameter	Value	Unit
TVD	13412	ft
Water Depth	5118	ft
Wellbore Deviation	0	o
Drill pipe ID	4.276	in
Drill pipe OD	5	in
Casing ID	12.615	in
Casing OD	13.375	in
Casing Shoe Depth.	12118	ft
Bit OD	12.25	in
Cementing OD	15	in
Riser OD	16.375	in

Table 3-Wellbore geometry parameters

Using the developed drilling circulation model, Figure 6 shows the first hour circulation drilling fluid temperature distribution in the drill pipe and annulus. The solid lines represent the fluid temperature in the drill pipe; the dashed lines represent the fluid temperature in the annulus; the black solid line represents the surrounding seawater/formation temperature. The transient temperature behavior is observed in Figure 6. As circulation time increases, more heat is carried upward by the drilling fluid. It is observed that maximum fluid temperature in the drill pipe is at the bottomhole; however, the maximum annulus fluid temperature is at some depth above the bottomhole. This can be explained by the fact that the annulus fluid receives heat from hot formation near the bottomhole, while loses heat to the cold drill pipe fluid as it moves upward. Initially, it gains more heat from hot formation than heat loss to the drill pipe fluid, so the annulus fluid temperature increases. The rate of heat gain diminishes as the annulus fluid encounters cooler

formation with decreasing depth. At the depth where the heat gain from formation is equal to the heat loss to the drill pipe fluid, the maximum annulus fluid temperature is reached. When the engineers design and select the casing, the maximum temperature in the casing at this depth should be considered for its thermal stress purpose. Above the annulus maximum temperature depth, annulus fluid gains less heat from formation and finally loses heat to both surrounding formation and drill pipe fluid. At a certain depth above the mudline, annulus fluid will gain heat from the injected drill pipe fluid. Similarly, the lowest annulus fluid temperature is at the depth where heat-loss from seawater is equal to the heat gain from the drill pipe fluid. Figure **7** shows the temperature distribution after 6 hours, 12 hours and 24 hours circulation. It can be observed that the temperature in both drill pipe and annulus become more stable. A pseudo-steady state temperature distribution has been reached in the wellbore.

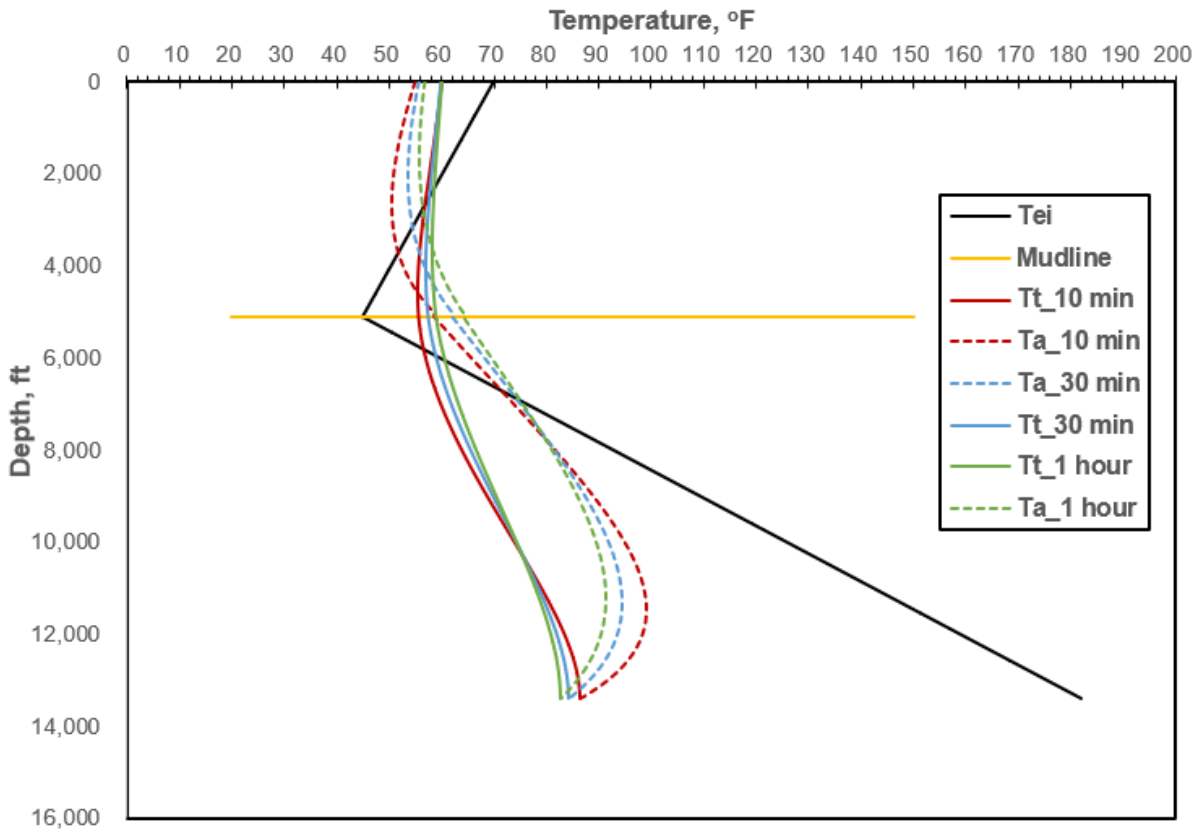

Figure 6-Circulation drilling fluid temperature distribution at 10-min, 30-min and 1-hour

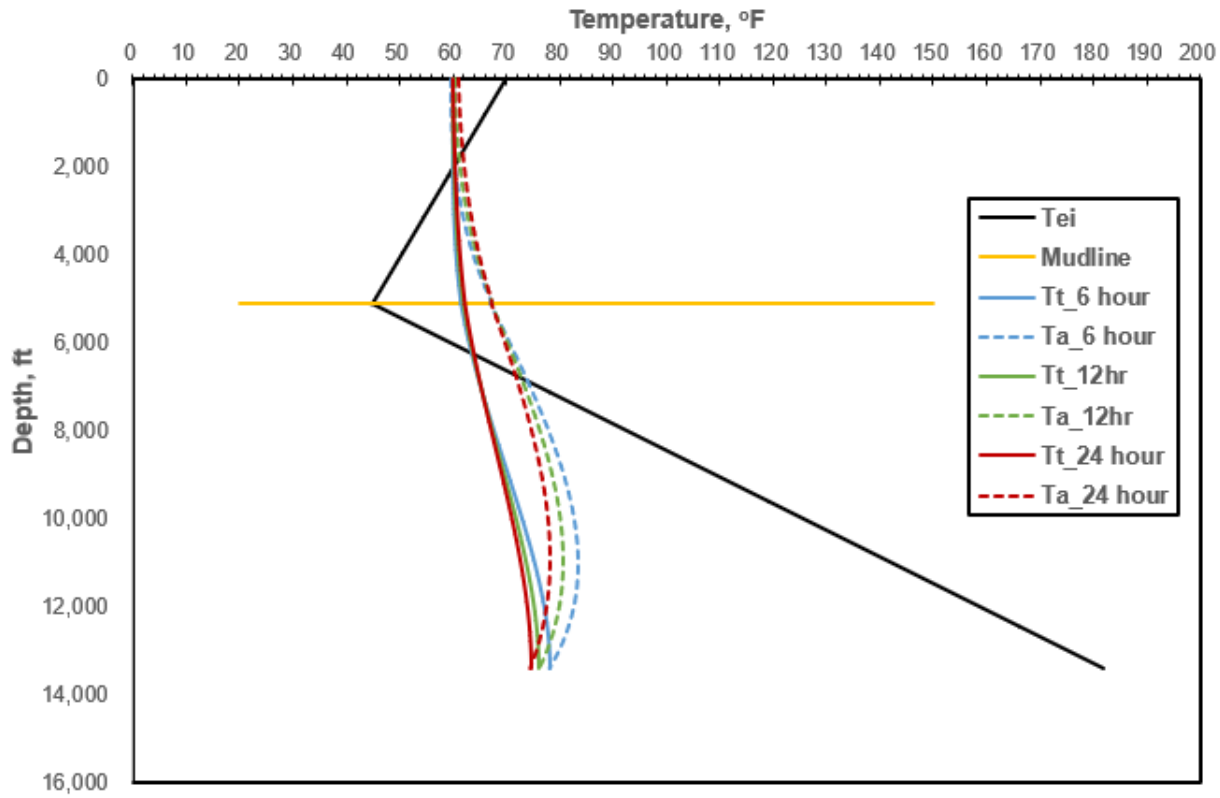

Figure 7-Circulation drilling fluid temperature distribution at 6-hour, 12-hour and 24-hour

3.3 Sensitivity studies

Setting 24 hours circulation time, 60 ^{o}F fluid injecting temperature, 600 gpm fluid injecting rate and 0.0124 ^{o}F/ft formation geothermal gradient as the base case. Using the field case in previous section, sensitivity studies on injecting rate, fluid injecting temperature and formation geothermal gradient are shown in this section. Figure 8 shows the temperature distribution in the wellbore with 100 gpm, 300 gpm, 600 gpm circulation rates. It indicates that lower circulation rate causes higher fluid temperature in the deep formation, however, it tends to lower the fluid temperature in the seawater portion. The maximum annulus fluid temperature is at the depth above the bottomhole and the minimum annulus fluid temperature is at the depth between surface and mudline. The maximum annulus fluid temperature with 100, 300, 600 gpm circulation rate are

102.4 °F at 11891 ft, 87.3 °F at 11355 ft, 78.3 °F at 10885 ft. The minimum annulus fluid temperature with 100 gpm, 300 gpm, 600 gpm circulation rates are 50.2 °F at 3018 ft, 58.3 °F at 939 ft, 60.9 °F at 30 ft.

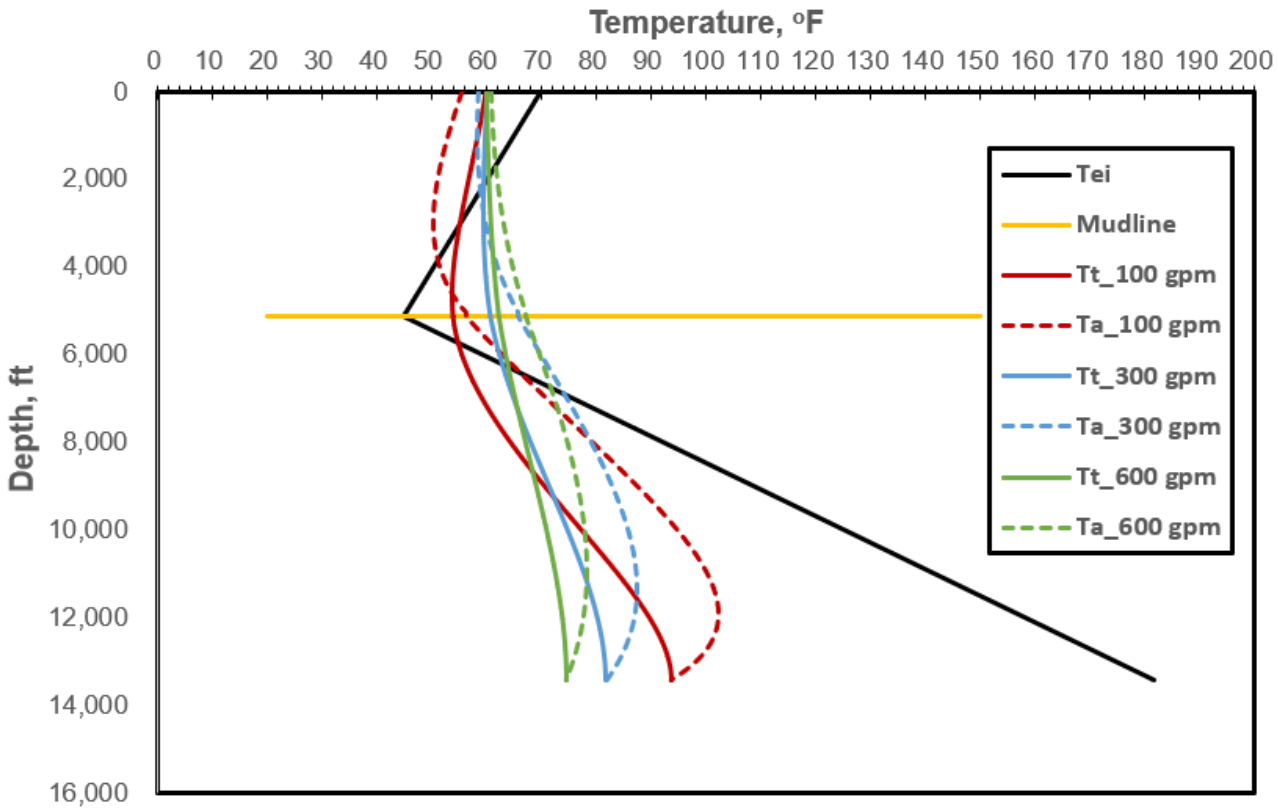

Figure 8-Circulation drilling fluid temperature: sensitivity study on injecting rate

Figure 9 illustrates the circulating fluid temperature with 60 °F, 70 °F and 80 °F fluid injecting temperature. It is obvious that higher injecting temperature tends to have higher temperature in the formation portion. At the bottomhole, every 10 °F increment in injecting fluid temperature raises about 5 °F fluid temperature in both drill pipe and annulus.

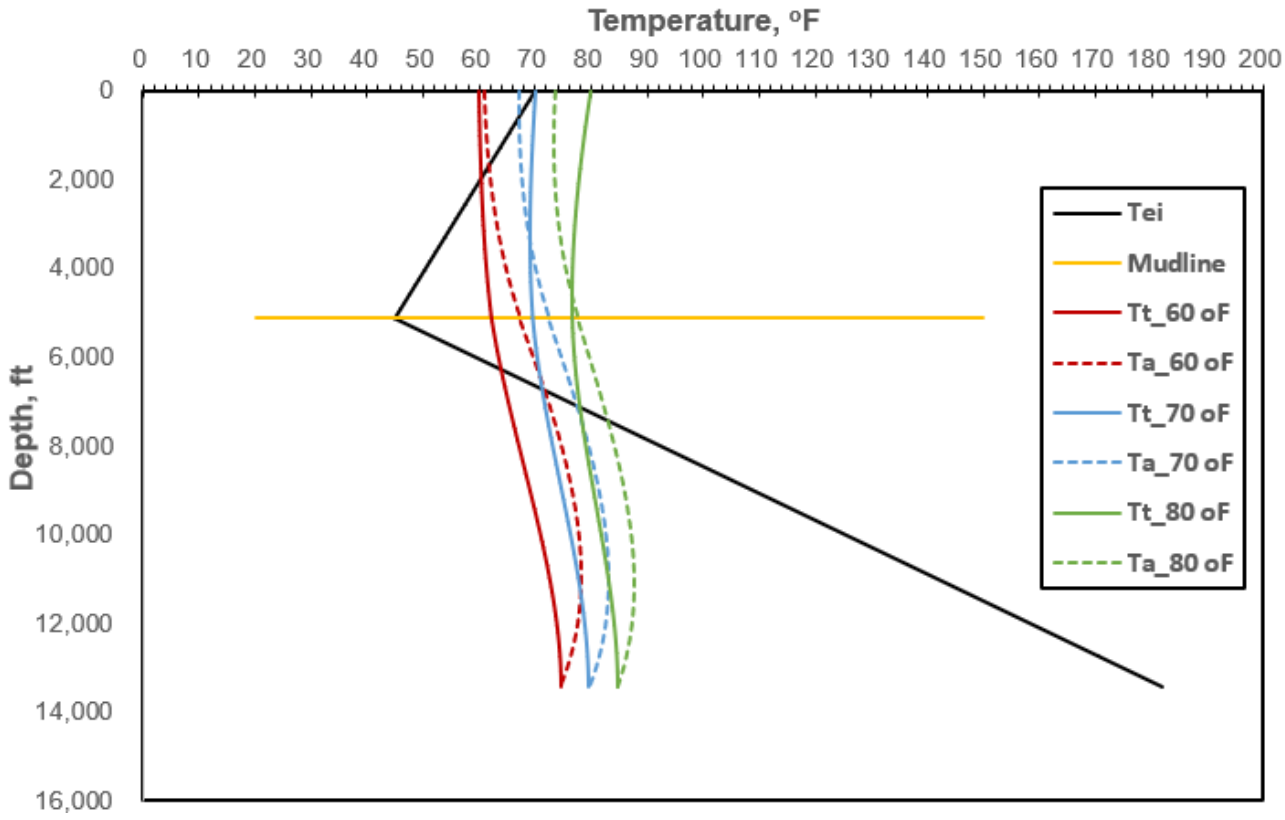

Figure 9-Circulation drilling fluid temperature: sensitivity study on injecting temperature

Figure 10 shows the wellbore fluid temperature distribution with different geothermal gradient. Increasing the geothermal gradient will increase the fluid temperature difference between drill pipe and annulus. In addition, it will cause larger heat transfer between wellbore and formation.

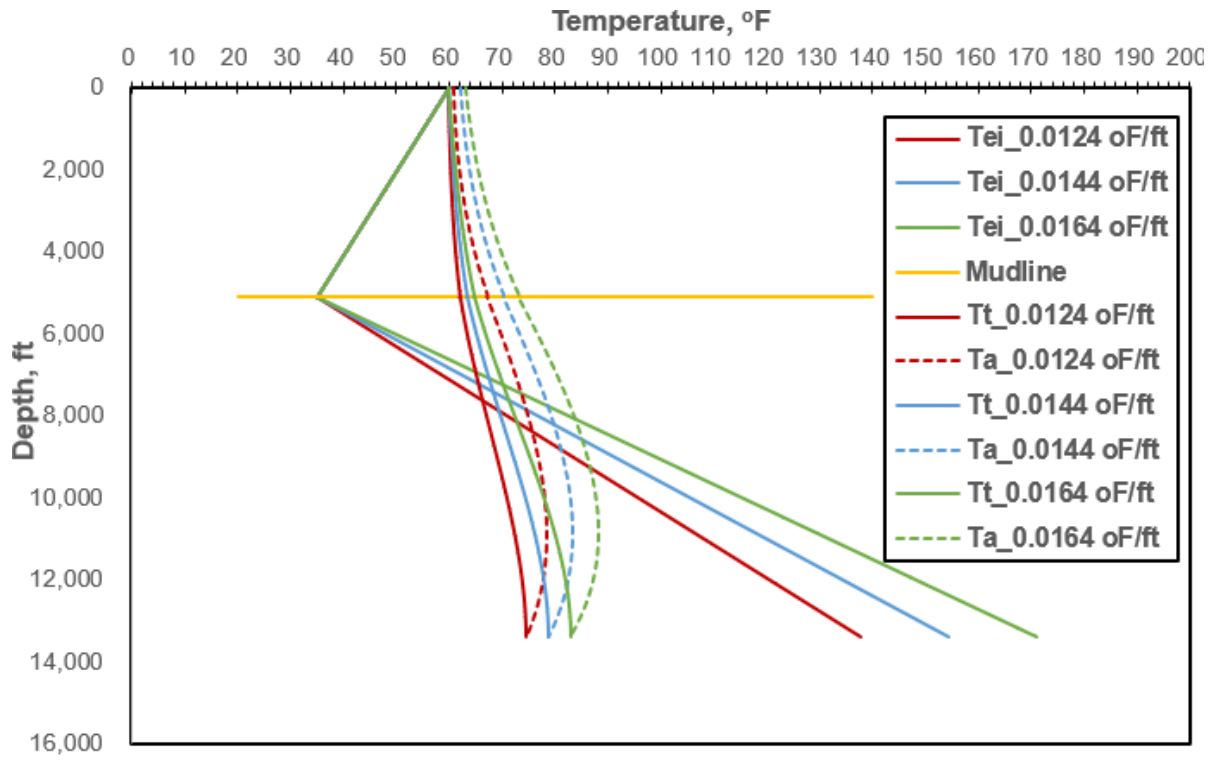

Figure 10-Circulation drilling fluid temperature: sensitivity study on formation geothermal gradient

3.4 Discussions

Estimation of deepwater drilling fluid circulating temperature is important for drilling design, well control and flow assurance purposes. This part proposes an analytical model by assuming steady-state heat transfer in the wellbore and transient heat transfer in the formation. The model applies an iterative approach to estimate circulating fluid temperature of deepwater wells because of the lack of knowledge of drill pipe/annulus fluid temperature at the mudline. The temperature difference between the drill pipe and annulus fluid is not large, therefore the iteration process is quite efficient. Instead of using this iteration approach, a complicated but rigorous analytical expression to estimate drilling/annulus fluid temperature at the mudline is given in Appendix A. The early transient behavior is observed in the simulated results of this study. The simulated results indicate that transient temperature behavior is obvious during first hour

circulation, however, a thermal equilibrium is reached after about 6-hours circulation. This result is consistent with the findings by Raymond (1969) and Gao et al. (2017). It is quick and reasonable to use this simple analytical solution to estimate drilling circulation temperature under moderate to long circulation time conditions. In addition, the simulated results show that the maximum annulus fluid temperature is at the depth above the bottomhole; the minimum annulus fluid temperature is at the depth between surface and mudline. When design and select tubulars, this fact should be taken into account. Bingham plastic model is assumed for drilling fluid in this analytical model, which means an effective viscosity is used for the calculations. The variations of drilling fluid viscosity, density and thermal properties as a function of temperature and pressure can be taken into consideration in the model by dividing the wellbore into small computational nodes and making a small spatial step at each computational node.

4. TRANSIENT TEMPERATURE PROFILES DURING CLEAN-UP PERIOD

4.1 Introduction

Early rate data can be very useful for transient analysis for clean-up periods. Such early analyses may offer reasonable formation properties, allow better design for more rigorous tests, and offer early estimates of a well's productivity. Flow rates can be measured using many types of flow meters. Unfortunately, most of these meters have many issues. MDTS data, can be a better alternative for rate estimations under many circumstances, especially for production from multiple zones in deepwater assets. However, early-time temperature data are affected by the fact that drilling process causes near-wellbore cooling. The temperature of the reservoir fluid flowing through this cooled near-wellbore zone gradually warms back. The physical process of reservoir fluid getting cooled as it flows through this cooled zone and the consequent heat-back of the zone needs to be modelled to properly utilize transient MDTS data.

Drilling fluid pumped from the wellhead through the drill pipe during drilling is at a much lower temperature than the target zone at the bottom of the well. Thus, drilling causes cooling of the near wellbore formation temperature at the well bottom. Knowledge of the extent of near wellbore cooling is essential for estimating flow rate from temperature during clean-up period because reservoir fluid flowing through the colder near wellbore area will get cooled down. In flowing through this zone, the reservoir fluid, in turn, will gradually start heat up this affected zone. The MDTS, at the central line of the well, reads fluid temperature at the well center. At the bottommost perforation, MDTS data represents the temperature of the fluid entering from the reservoir because it does not get mixed with fluid from any other zone. This transient fluid temperature becomes the basis for the rate estimation model developed below.

4.2 Model development

A schematic of near wellbore zone is illustrated in Figure 11. Akin to the concept of radius of investigation in pressure transient analysis, we assume that all the cooling occurs in an affected of radius, r_a. Although the affected zone temperature will asymptotically approach the undisturbed formation temperature, T_{ei}, we use a linear approximation of the affected zone temperature profile as shown by the red-to-blue straight line. During the clean-up period, warmer reservoir fluid will flow toward the wellbore through the cooled affected zone and enter the wellbore at a lower temperature, T_{fe}. In turn, the affected zone will get heated up gradually by the warmer reservoir fluid. Thus, T_{fe} will gradually rise with time.

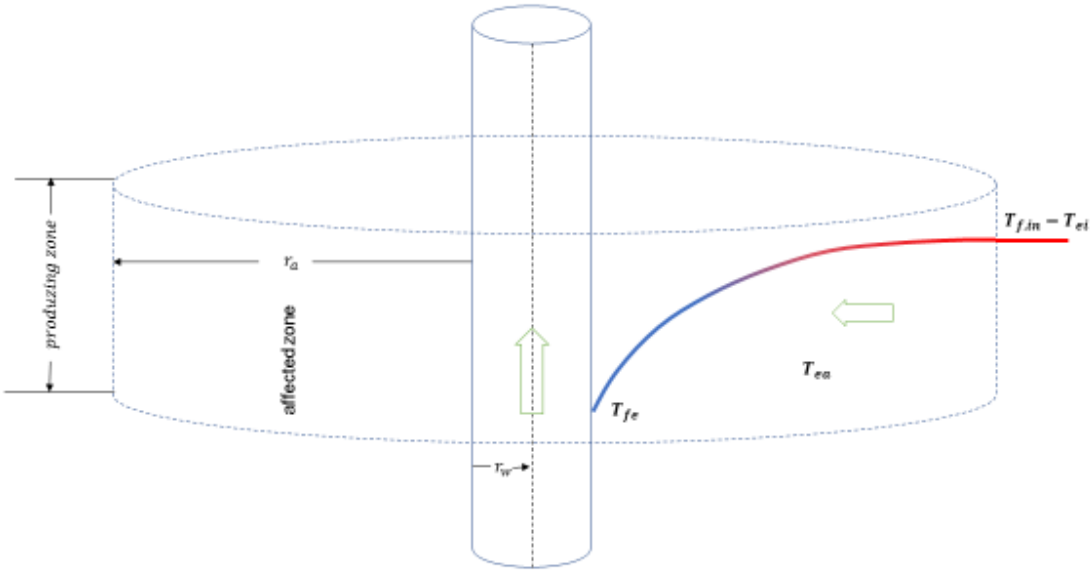

Figure 11-Schematic of near wellbore formation cooled by drilling circulation

To model this transient process, following assumptions are made:

- Geothermal temperature, T_{ei}, is a known function of depth.
- Geothermal temperature, T_{ei}, is a known function of depth.

- The formation and fluid have constant thermal properties.
- Fluid mass flow rate, w, is constant.
- Reservoir fluid enters cooled near wellbore formation at the undisturbed formation temperature, T_{ei}; it exists the cooled near wellbore formation and enters the wellbore at a time varying temperature at wellbore formation interface, T_{fe}.
- To consider the fact that more cooling effect occurring near the wellbore, the average temperature of cooled near wellbore formation, T_{ea}, is assumed to be a weighted average of entering and exiting temperature; $T_{ea} = (1\text{-}x)T_{ei} + xT_{fe.}$
- Wellbore heat storage is assumed to be negligible.

Hence, heat loss by the fluid passing through the affected zone is $wc_{pf}(T_{ei} - T_{fe})dt$, where c_{pf} is the specific heat of the fluid. Using m_a as the mass of the affected formation and c_{pe} is its specific heat, heat gained by the affected zone is given by $m_a c_{pe} dT_{ea}$. Thus,

$$wc_{pf}\left(T_{ei} - T_{fe}\right)dt = m_a c_{pe} dT_{ea} \tag{8}$$

For this energy balance purposes, we have assumed that a lumped temperature, T_{ea}, can represent the affected zone temperature which is a weighted average of the entering and exiting fluid temperatures. Total time required for heat back from cold temperature of T_c to the higher temperature, T_{ea}, approaching (but never reaching) earth temperature T_{ei} is obtained by integrating Eq. 8,

$$t = \frac{m_e c_{pe}}{wc_{pf}} \int_{T_c}^{T_{ea}} \frac{dT_{ea}}{(T_{ei} - T_{ea})} \tag{9}$$

Noting that $dT_{ea} = x dT_{fe}$ and designating the lumped parameter ($xm_a c_{pe}/wc_{pf}$) as relaxation time, t_r, we rewrite Eq. 9,

$$\frac{t}{t_r} = \int_{T_c}^{T_{fe}} \frac{dT_{fe}}{(T_{ei} - T_{fe})} \tag{10}$$

Solve Eq. 10 could obtain:

$$T_{fe} = T_{ei} - (T_{ei} - T_c) \cdot e^{-t/t_r} \tag{11}$$

In Eq. 11, T_c is the initial temperature of the fluid entering from the reservoir. MDTS data available at the bottommost perforation offers entering fluid temperature, T_{fe} as a function of time. Using Eq. 11 then allows estimation of $t_r = xm_ac_{pe}/wc_{pf}$. If mass of the affected zone, m_a, can be estimated, mass flow rate, w, can be obtain from this procedure. This procedure also requires a value of the weight, x. A linear temperature profile of the affected zone would have been led to a value of ½ for x. However, the curved nature of the temperature profile and examination of the bottommost perforation fluid data led us to use $x = 2/3$.

At any position other than the bottommost perforation, fluid coming up from below gets mixed with fluid entering from the reservoir; the MDTS data indicate the mixing temperature, Figure 12 illustrates this process. The red squares in Figure 12 are the temperature sensors. Thus, T_{fe1} represents the bottommost zone fluid temperature entering the wellbore and T_{fe2} is the second zone fluid temperature flowing into the wellbore; T_f is the fluid temperature in the wellbore recorded by the temperature sensor.

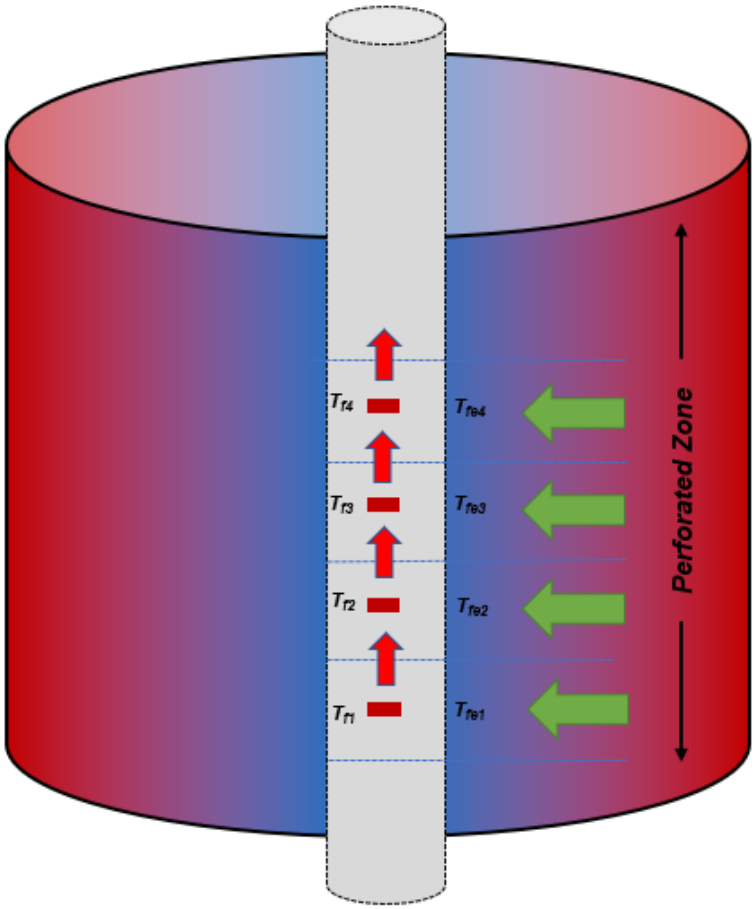

Figure 12-Fluids coming from the lower zone is mixing with the fluid from the formation

Neglecting potential and kinetic energy changes and assuming enthalpy change is accounted for through temperature change only, we get:

$$c_{pf} w_1 T_{f1} + c_{pf} w_2 T_{fe2} = c_{pf} (w_1 + w_2) T_{f2} \qquad (12)$$

There are two unknowns in Eq. 12, mass flow rate from the second zone, w_2, and second zone fluid temperature flowing into the wellbore (T_{fe2}). T_{fe2} is an unknown because temperature sensor, placed at the center of the well, reads temperature of the fluid that is already partially mixed with the fluid flowing up from below. So, we use the near wellbore cooling relationship, Eq. 11, to estimate temperature of the reservoir fluid entering at the sandface. Although Eq. 11 and 12 is a "two equations – two unknown" system, the solution is not straight forward because

the equations are non-linear in rate. We use an iterative approach to solve these equations to obtain w_2. Similarly, the mixing rule for bottom three zones are:

$$c_{pf}(w_1 + w_2)T_{f2} + c_{pf}w_3T_{fe3} = c_{pf}(w_1 + w_2 + w_3)T_{f3} \quad (13)$$

4.3 Field example

We used a real field MDTS data for illustration purpose. A summary of the related data is shown below in Table 4. The bottommost producing zone is at 13,389 ft. (4080.9 m). With the given parameters in Table 4 and the transient temperature data, Eq. 11 was used to obtain the optimum flow rate of 6,000 *Mscf/D* that minimized the sum of square of errors between the estimated T_{fe} and the data. Figure 13 shows the comparison of measured and the calculated fluid temperatures. The circles are the data from the sensor while the curved line represents temperature values calculated using the proposed model.

Parameter	Value	Unit
Affected radius	15	ft
Wellbore radius	0.5	ft
Gas specific gravity	0.6	/
Initial formation pressure	7500	psi
Gas specific heat	0.478	Btu/(lb-^{o}F)
Formation specific heat	0.215	Btu/(lb-^{o}F)
Formation density	144	lb/ft^3

Table 4-A summary of related parameters in this field example

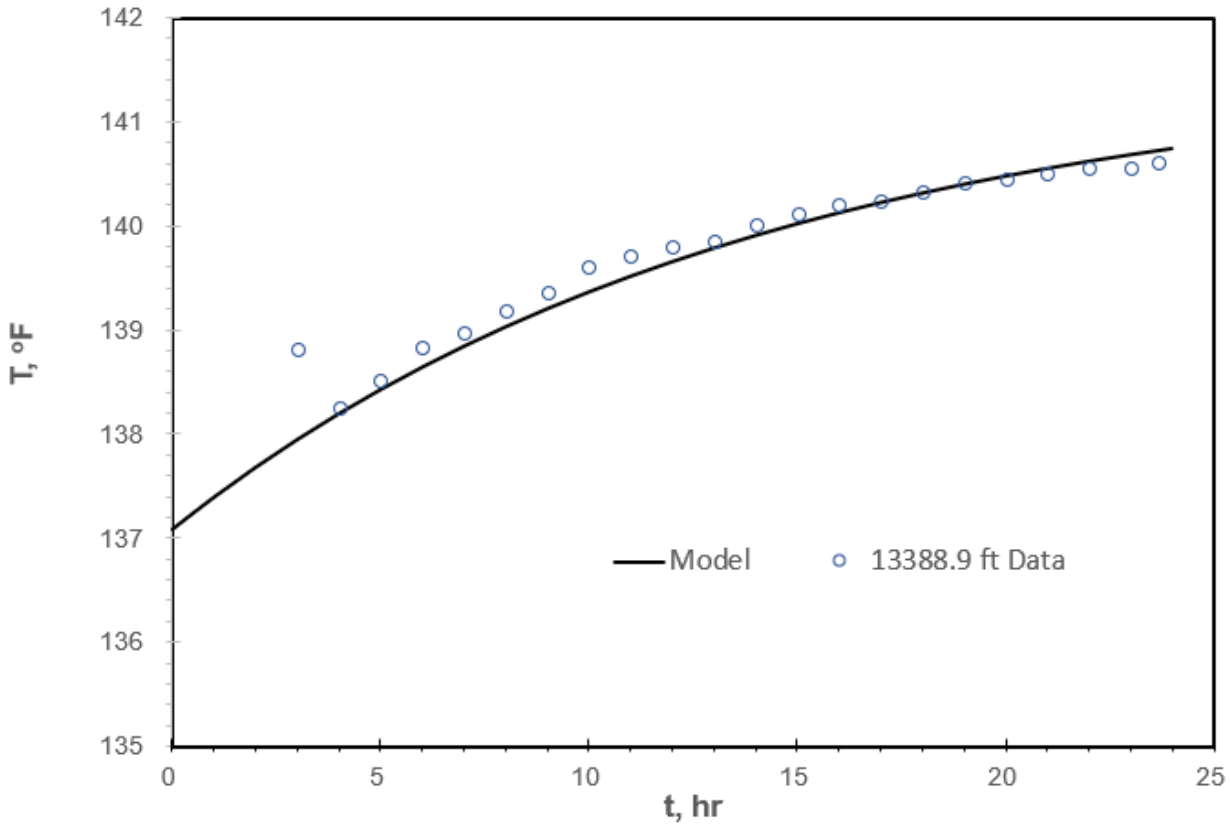

Figure 13-Matching bottommost zone calculated fluid temperature with MDTS measured temperature to estimate flow rate

The optimization process excluded the first five hours of data that were affected by the energy released during the firing of perforating guns. The heat generated during perforation caused a dramatical increase in fluid temperature. As fluid started moving in from the reservoir, these hot fluids were swept away. The data after five hours were essentially unaffected by the energy release during perforation. These unaffected data show how the fluid coming in from the reservoir is cooled down as it flows through the affected zone. The rise in entering fluid temperature with time also show that the affected zone gradually gets heated up.

The second sensor is located at 13,384 ft (4079.3 m). Figure 14 shows the MDTS measured as red and black circles respectively. The estimated temperature of fluid entering the well from the

reservoir at second zone is the solid blue line; the estimated mixing fluid temperature is the black dashed line. The flow rate from second zone is estimated to be 2,400 *Mscf/D*.

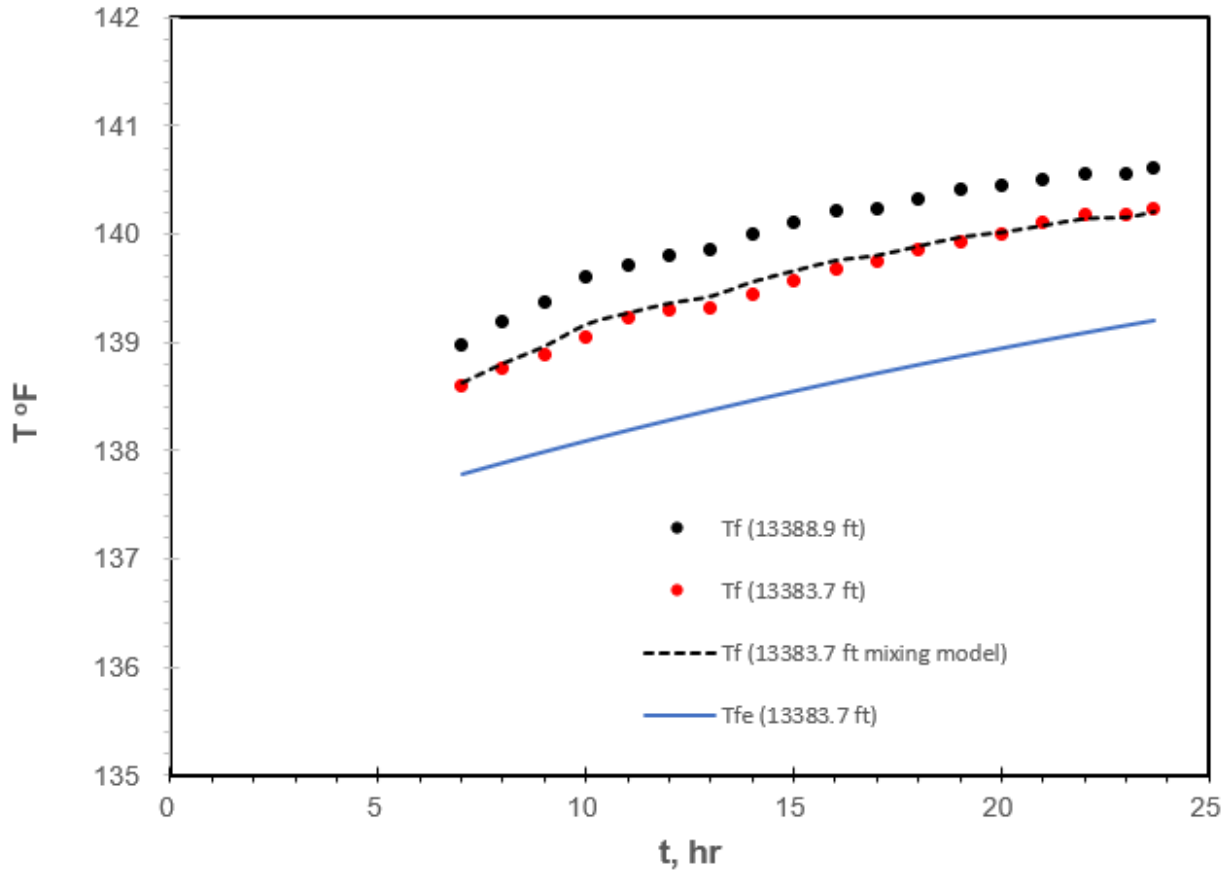

Figure 14-Matching second zone calculated fluid temperature with MDTS measured temperature to estimate flow rate

Continuous with other 76 MDTS across the whole perforation zones, we are able to estimate the flow rate from each zone. Figure 15 shows the flow rate distribution across the perforation zone. It is obvious that the bottom half perforation zones (13,250 ft – 13,389 ft) contributes much more than the top half perforation zones (13,040 ft – 13,250 ft). Figure 16 shows the cumulative flow rate distribution across the perforation zone. The bottom half perforation zones contribute about 94% of the total production.

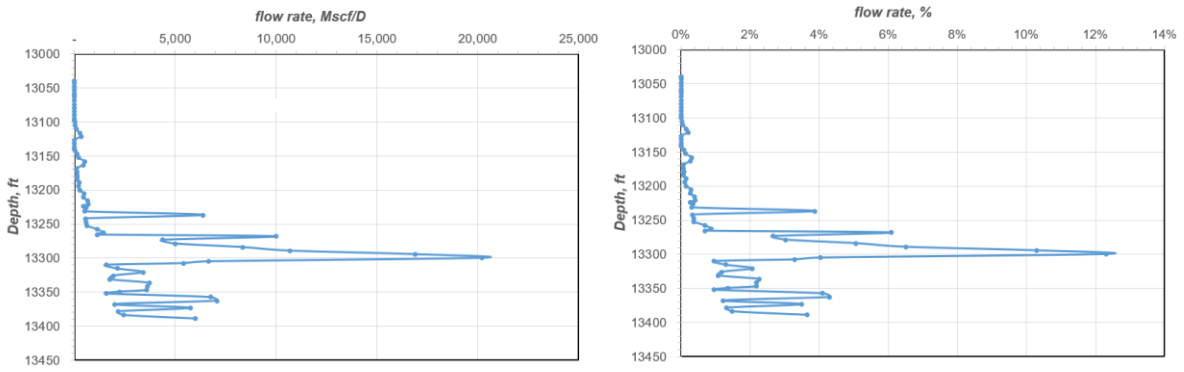

(a) (b)

Figure 15-(a) Flow rate distribution across the perforation zone;(b) Flow rate distribution in percentage across the perforation zone

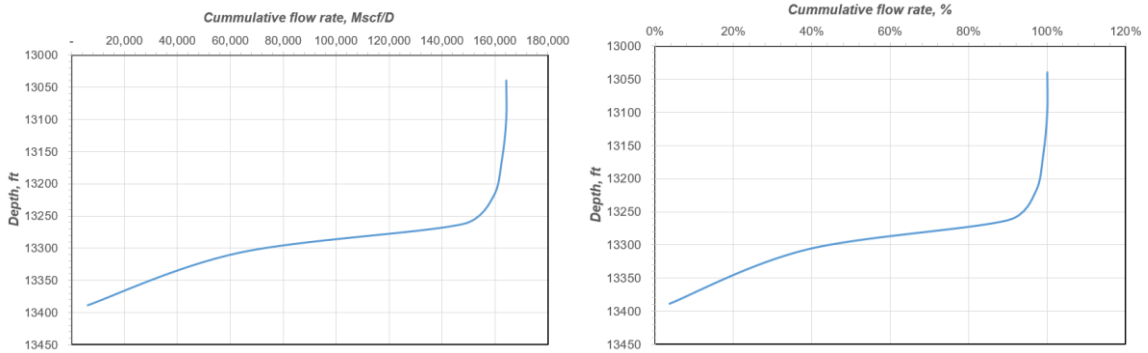

(a) (b)

Figure 16-(a) Cumulative flow rate distribution across the perforation zone;(b) Cumulative flow rate distribution in percentage across the perforation zone

5. FLUID FLOW AND HEAT TRANSFER IN THE RESERVOIR[1]

5.1 Model development

The reservoir model, schematically shown in Figure 17, represents single-phase fluid flowing from the reservoir boundary r_e toward the wellbore in the radial direction (without any vertical component of velocity) at a constant rate.

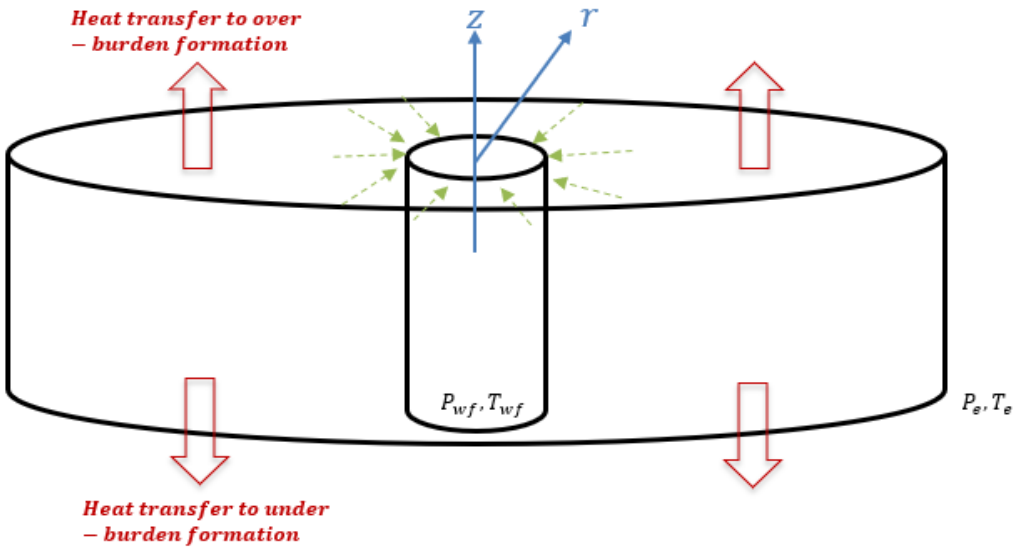

Figure 17-Schematic of the reservoir/wellbore model

The comprehensive energy-balance equation for a single-phase flow in the reservoir, can be reduced to the partial-differential equation shown below:

[1] *Part of the work in this chapter is reprinted with permission from "Modeling Coupled Nonisothermal Reservoir/Wellbore Flow Behavior in Gas Reservoir Systems" by B. Xu, S. Kabir, A.R. Hasan. 2018, SPE Proceedings. Copyright by Society of Petroleum Engineers.

$$\left[\emptyset s_f \rho_f c_{pf} + \emptyset s_w \rho_w c_{pw} + (1-\emptyset)\rho_e c_{pe}\right]\frac{\partial T}{\partial t} + \rho_f u_r c_{pf}\frac{\partial T}{\partial r} + \rho_f u_r \sigma_f \frac{\partial p}{\partial r} +$$

$$\left[\emptyset s_f \rho_f \sigma_f + \emptyset s_w \rho_w \sigma_w - 1\right]\frac{\partial p}{\partial t} = \frac{1}{r}\frac{\partial}{\partial r}\left[\lambda r \frac{\partial T}{\partial r}\right] + \dot{H} \qquad (14)$$

In Eq. 14, subscripts *f*, *w*, and *e* refer to properties of the fluid (gas or oil), water, and earth (formation), respectively. We assumed that permeability, porosity, and fluids' thermal properties of the formation and fluids remain unchanged, radial conductive heat transfer is negligible, and fluid temperature and pressure at the reservoir boundary are constant. For the case of a gas reservoir, we replace pressure *p* by pseudopressure, m(*p*). The first two terms of Eq. 14 are energy change due to temperature transient and convective heat transfer, respectively. The third term represents the J-T effect and the fourth term is the AE effect. The first term on the right-hand side is radial heat conduction (ignored) and second term $\dot{H}$ represents heat exchange with over- and under-burden formations. The solution of Eq.16 in Laplace domain can be written as:

$$\bar{T}(r,s) = \frac{T_{ei}}{s} e^{-\left(\frac{As+D}{2B}\right)(r_e^2 - r^2)} + e^{\left(\frac{As+D}{2B}\right)r^2}\int_r^{r_e} M(x,s)dx \qquad (15)$$

In Eq. 15, T_{ei} is the initial formation temperature, and *s* is the Laplace variable. Appendix B presents the derivation of Eq. 15 and various terms in Eq. 15. We used numerical Laplace inverse transform and integration algorithm to solve Eq. 15. However, when the AE effect term is neglected, we obtained the following fully analytical solution:

$$T(r,t) = T_{ei} + \frac{C}{2B} e^{\frac{Dr^2}{2B}} Ei\left[-\frac{D(Ar^2+2Bt)}{2AB}\right] - \frac{C}{2B}\, e^{\frac{Dr^2}{2B}} Ei\left[-\frac{Dr^2}{2B}\right] \qquad (16)$$

The detailed derivation of Eq. 16 is shown in Appendix C. Note that if ignoring the effect of AE in the semianalytical solution, the results of Eq. 15 will become the same as that in the analytical

solution given in Eq. 16. The analytical solution provides a quick way to estimate the temperature distribution. At the sandface, Eq. 16 can be further simplified in natural logarithm of the variables inside the bracket of term two and term three are smaller than 0.01. Ignoring both the AE effect and heat exchange with over- and under-burden formations, the resulting analytical solution of Eq. 14 may be written as:

$$T(r,t) = T_{ei} - \frac{C}{2B}\ln\left(\frac{r^2 A}{r^2 A + 2Bt}\right) \tag{17}$$

The preceding assumptions may be quite reasonable at low production rates and short producing times. Note that the reservoir pressure distribution is calculated using the radial diffusivity equation. The formation damage may be treated as a constant by assuming the steady-state pressure distribution in the near wellbore region. The variations of viscosity, density, J-T coefficient as a function of temperature and pressure could be taken into consideration by making a very small spatial step at each computational node. Appendix D presents the approach for estimating the J-T coefficient from the PVT relationship.

5.2 Model validation

Before we applied the nonisothermal reservoir flow model and wellbore heat transfer model to Well A, we first need to validate the models. In this section, we used the numerical simulations performed with a commercial software package (CMG) by Mao and Zeidouni (2017) for a gas reservoir and a high-drawdown gas well test by App (2009) to verify the nonisothermal reservoir flow model. Then, an offshore well in West Australia with permanent downhole gauge (PDG) measured temperature data validated the coupled reservoir/wellbore heat transfer model.

Figure 18 shows the temperature distribution in a gas reservoir. The red open circles represent the numerical simulations by Mao and Zeidouni (2017); the solid black line represents the semianalytical solution with AE effect but without the heat exchange, $\dot{H}$. Note that Mao and Zeidouni activated the AE effect, but neglected $\dot{H}$. The estimation of our model agrees well with those obtained by the rigorous numerical simulations. For this low pressure (725 psia) reservoir with a drawdown of 75 psi, the sandface temperature drops from $176°\mathrm{F}$ to $174.5°\mathrm{F}$. The temperature drop occurs in the near wellbore due to J-T cooling dominating in this region. Also, Figure 18 directly compares the AE effect and heat exchange as shown by the solid green line (with $\dot{H}$ and without AE) and the blue dashed line (with $\dot{H}$ and with AE). One observes that inclusion of the AE effect causes the gas temperature to drop a little. This phenomenon can be explained by the work performed by the fluid expansion. This energy loss translates into lower fluid temperature. However, including the $\dot{H}$ term is different. As the cooled gas flows toward the wellbore, it gains energy from the surroundings, leading to the increased fluid temperature. Comparing the solid black line with the blue dashed line in Figure 18, it is clear that the effect of heat exchange is more important than the AE effect. For this case, the gas temperature increased by about $0.1°\mathrm{F}$ at the sandface by heat exchange with surroundings, but negligible value by the AE effect. For higher gas production rate, the heat exchange with over- and under- burden formations will be more pronounced and, therefore, the AE effect can be safely neglected.

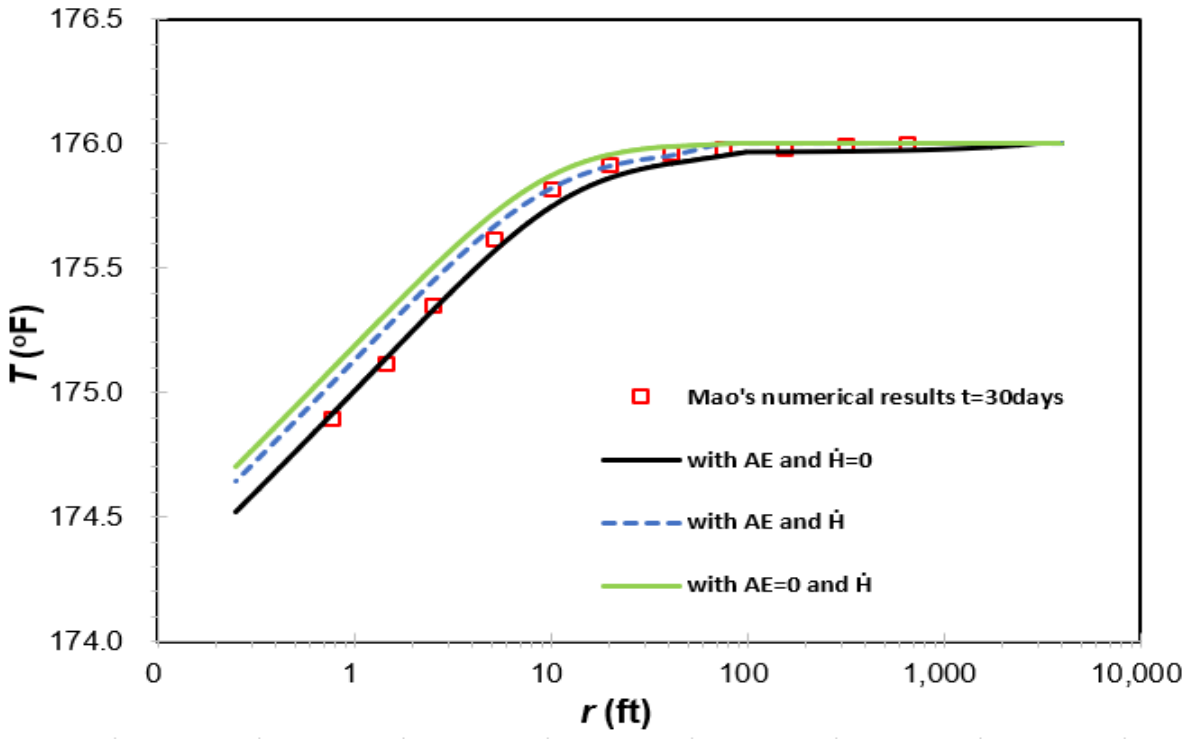

Figure 18-Model validation for a gas reservoir

Figure 19 shows the temperature distribution in an oil reservoir. The solid black line represents the semianalytical solution with AE effect but without the heat exchange, $\dot{H}$. Note that Mao and Zeidouni activated the AE effect, but neglected $\dot{H}$. The estimation of our model agrees well with those obtained by the rigorous numerical simulations. For this high pressure (21,000 psia) reservoir with a drawdown of 3800 psi, the sandface temperature increases from 302 °F to 309 °F due to J-T heating effect. Similar to the gas reservoir, as the fluid expands, it works against the external pressure. This energy loss manifests in terms of lower fluid temperature. Interestingly, the adiabatic expansion or the AE effect induces a small temperature drop in the far-away field, but the temperature continues to increase in the near wellbore region. The reason for this phenomenon relates to the J-T heating effect, which is dominant in the near wellbore region. As the fluids flow from the far-field toward the wellbore, the AE effect first cools the fluid a little,

then the J-T heating effect dominates in the near wellbore region, thereby raising the fluid temperature. When the heat exchange with over- and under- formations is accounted for, the fluid loses heat to the surroundings due to the elevated fluid temperature caused by the J-T heating. The solid green line in Figure 19 shows lower oil temperature due to the increased heat loss to the surroundings (with the heat transfer coefficient, $h_c = 0.92\ \mathrm{Btu/(hr \cdot ft^2 \cdot °F)}$). The blue dashed line shows that the temperature decreases further when both the AE effect and the heat exchange are considered. For this case with flow rate at $2{,}000\ \mathrm{STB/D}$, the heat exchange effect $\dot{H}$ is more than twice than that due to the AE effect near the wellbore. For higher oil production rate, the heat exchange effect could be more important than that due to the AE effect.

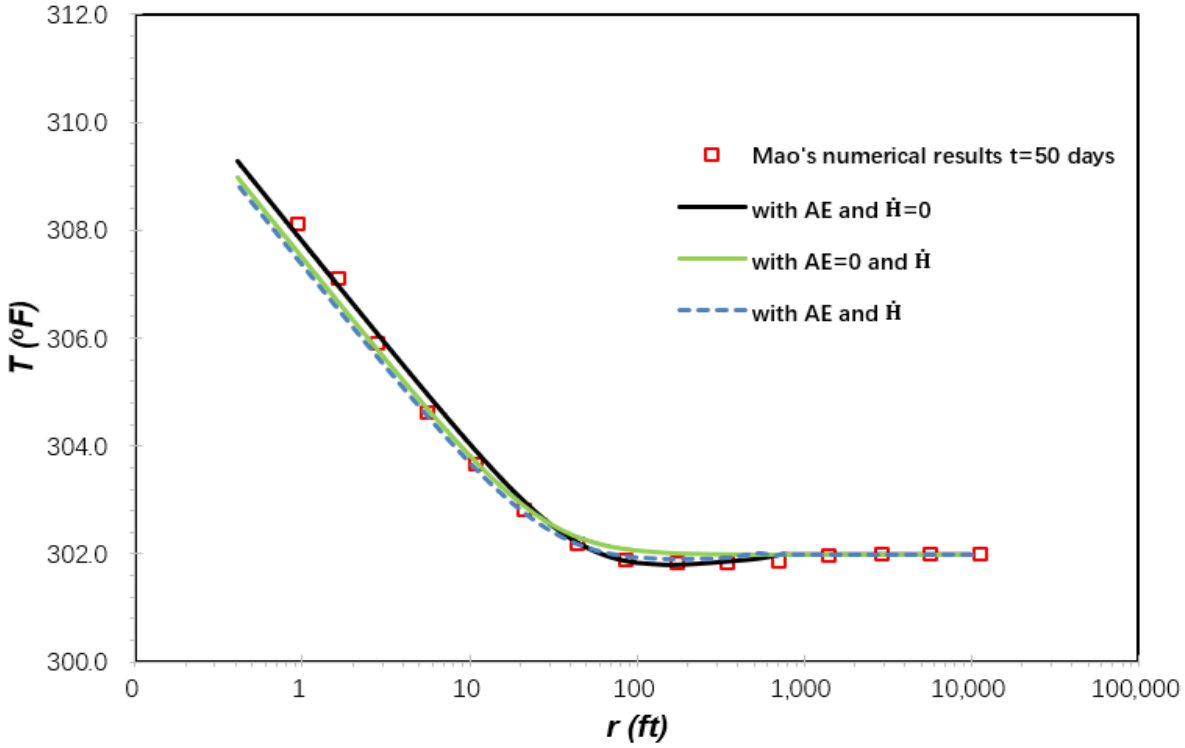

Figure 19-Model validation for an oil reservoir

Using the proposed reservoir heat transfer model, we can generate the bottomhole pressure and temperature at various producing times with consideration of the variations of viscosity, density, and the J-T coefficient as a function of temperature and pressure. Figure 20 shows the results during the main flow period: the solid black and red lines are fully numerical simulated pressure and temperature presented earlier by App (2009); the black and red dashed lines represent the simulated pressure and temperature, respectively, obtained by the proposed model in this study. The simulated pressure and temperature in this study matched with the numerical simulation very well. The magnitudes of both pressure and temperature drawdown at the end of the main flow period are all reproduced accurately. As Figure 20 indicates, the sudden drop of pressure triggers the proportionate temperature response.

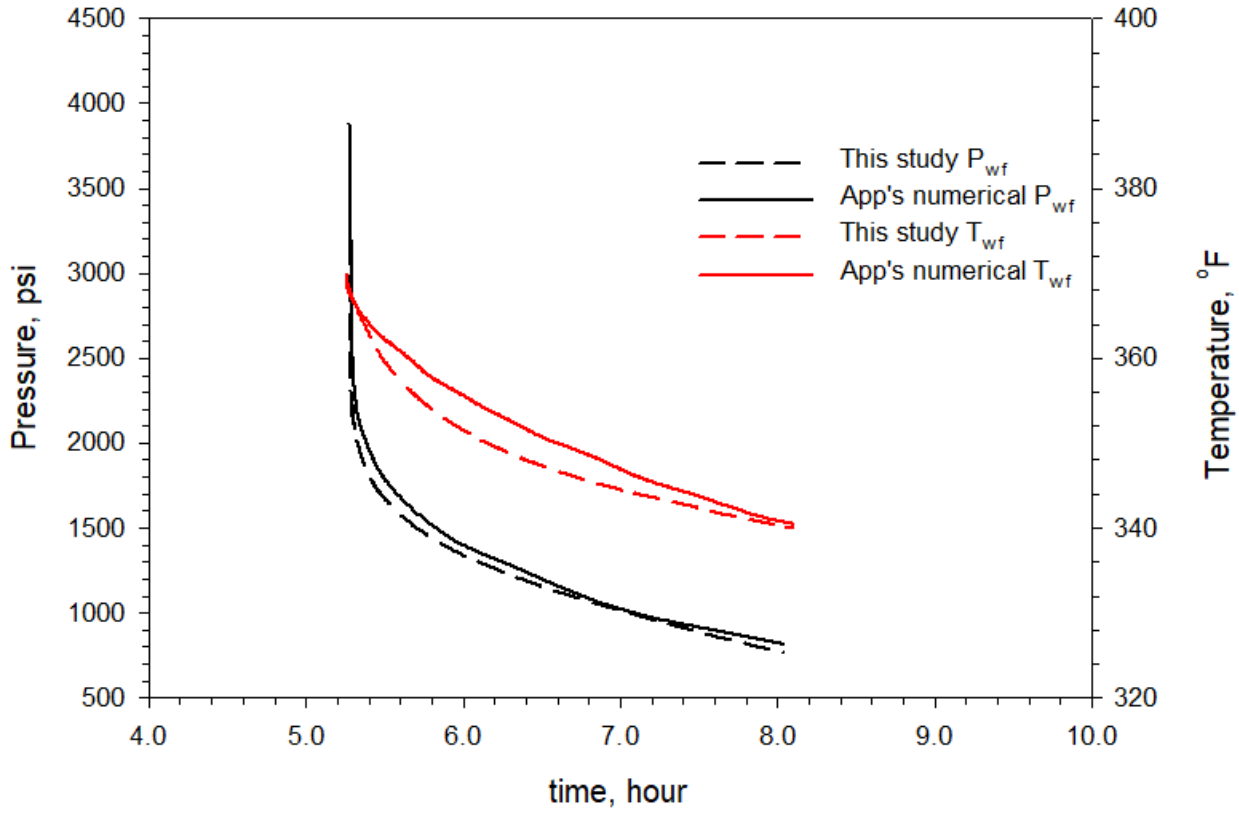

Figure 20-High drawdown gas test (Modified after App, 2009)

5.3 Sensitivity studies

Continued with the field case presented by App (2009). This section presents a sensitivity study of the influence of reservoir pressure to illuminate both heating and cooling behavior. We will focus on gas reservoir since it is more complicated. For a gas reservoir, the J-T coefficient is positive at low pressures implying the cooling effect and is negative at high pressures condition, when the heating occurs. Overall, an equation-of-state helps to determine the J-T coefficient involving the gas composition and changes in pressure at different reservoir temperatures. We explored this phase of the sensitivity study with the field example presented in the previous section. First, we played with the initial pressure by keeping all other parameters the same. Figure 21 illustrates the pressure and temperature distributions with different initial pressures. The solid lines represent the temperature distribution, and the dashed lines represent the pressure difference, $p_i - p_{wf}$. Here, we used Δp for ease of visual clarity. For initial pressures less than 7,000 psia, the cooling effect is transparent, whereas that above 10,000 psia, the gas behaves similar to the liquid, thereby explaining the heating effect. For pressures between 9,000 psia and 10,000 psia, it has neither heating nor cooling effect. Note that these solutions pertain to the gas composition that we used; therefore, some variations of these findings will occur depending on the fluid composition of interest.

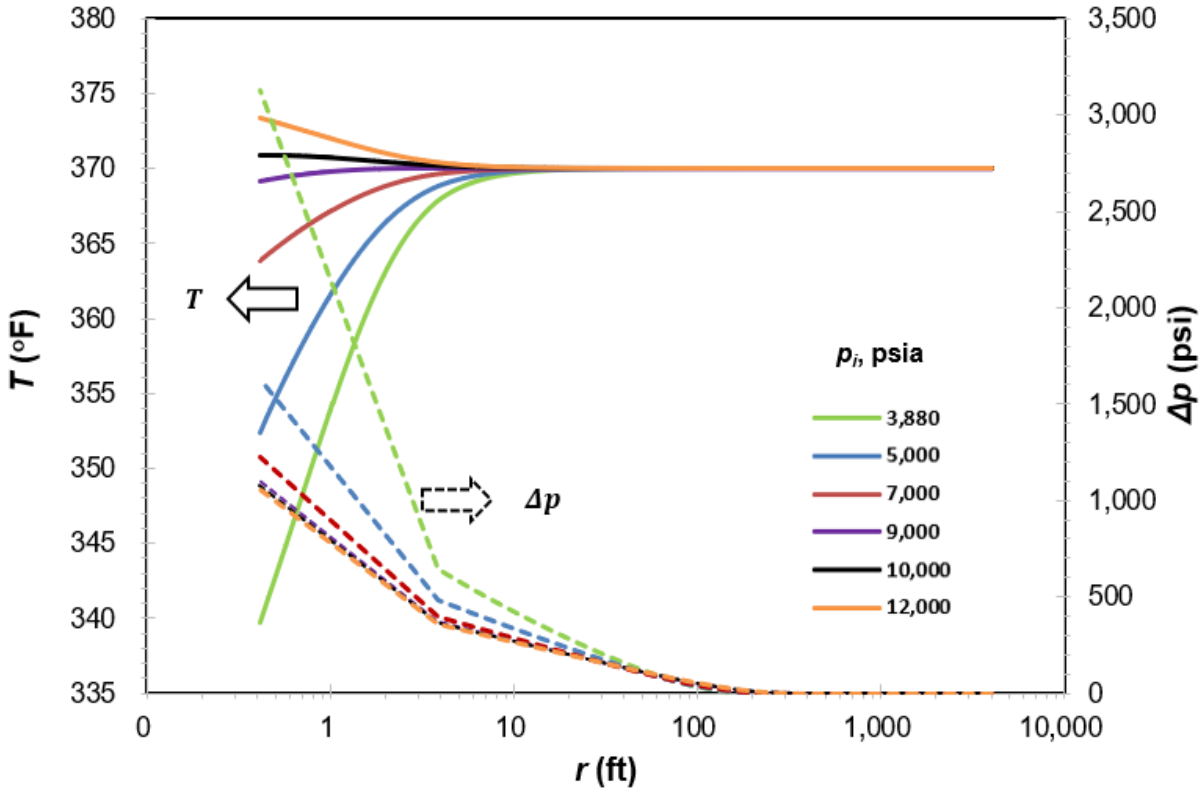

Figure 21-Pressure and temperature distribution with different initial pressures

To gain clarity, let us consider the pressure range of 9,000 psia and 10,000 psia, wherein minor variations of temperature occurred. Figure 22 shows the temperature distribution for this pressure range. Interestingly, the gas temperature slightly increases with expansion, reach a plateau, and then gradually starts to decline to correspond to the declining bottom hole pressure. Although the influence of this phenomenon on fluid temperature is small, less than $1^{o}F$ in this case, it can still provide a good indication of the existence of a damaged zone, which precipitates a sudden pressure change in the near wellbore region.

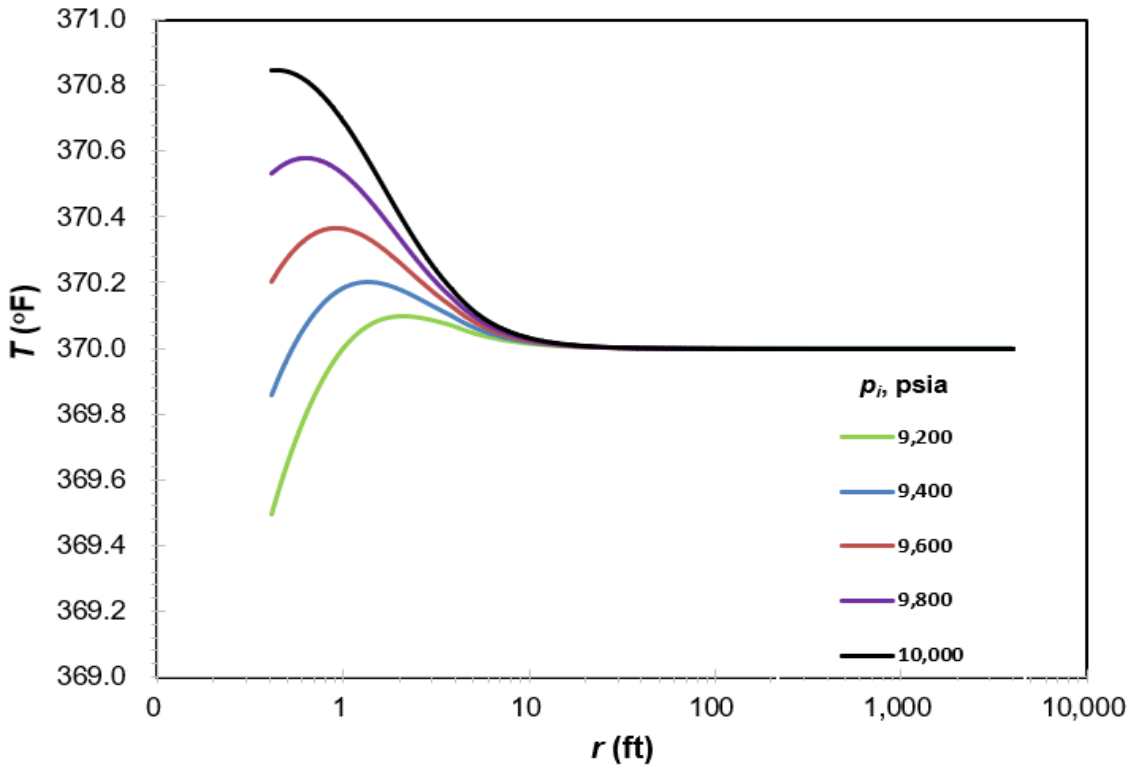

Figure 22-Temperature distribution between 9,000-10,000 psia initial pressure

Figure 23 displays the J-T coefficient distribution at different pressures. At low pressures, the J-T coefficient keeps changing from the infinite reservoir to the wellbore and this change grows in the near wellbore region due to the increased pressure drop. Besides, the J-T coefficient is more stable in the high-pressure condition. One also observes that between 9,000 psia to 10,000 psia, the J-T coefficient approaches zero. To summarize, for the initial pressure less than 7,000 psia, the cooling effect (positive J-T coefficient) sets in, whereas that for pressures larger than 9,000 psia, the heating effect (negative J-T coefficient) predominates.

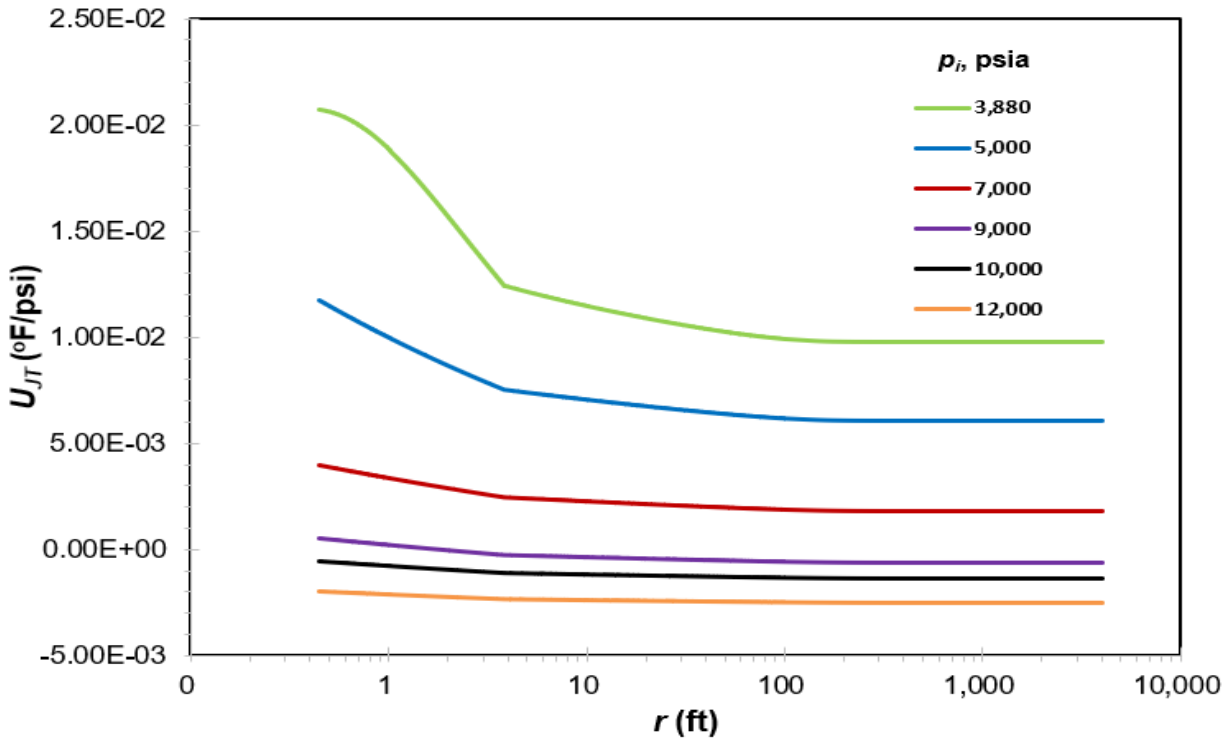

Figure 23-Joule-Thomson coefficient distribution with different pressures

Figure 24 shows the sensitive study on the gas production rate. Here we assumed the initial pressure to be constant at 3,880 psia. With higher gas production rate, the dominating J-T cooling effect in the near wellbore causes lower temperature profiles.

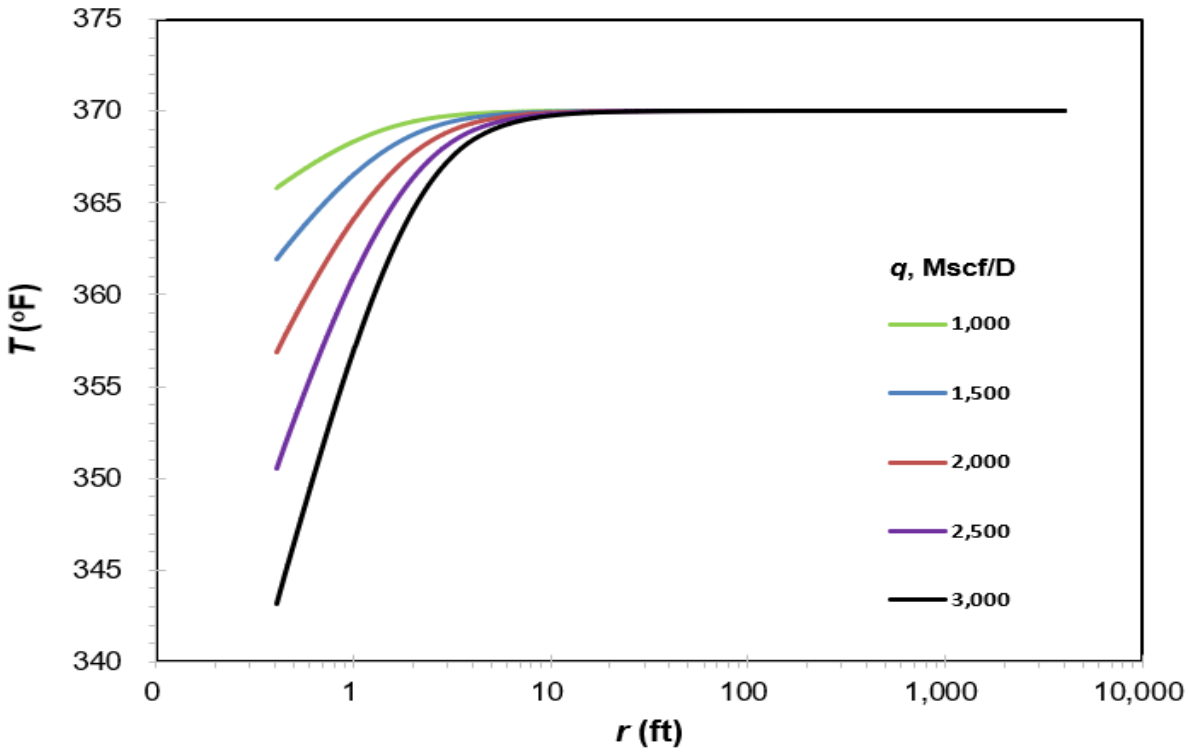

Figure 24-Temperature distribution with different flow rates

5.4 Discussions

This part presents a semianalytical solution to estimate the fluid temperature in the reservoir, which includes the J-T effect, AE effect, and the heat exchange with surrounding formations. The impact of the J-T effect dominates in the near wellbore region, and changes in fluid temperature usually occurred within 10 to 50 ft from the wellbore. These calculations also facilitate identifying the near wellbore formation damage due to sudden pressure change. In general, the J-T coefficient is always negative for oil reservoir with heating effect; positive in a low-pressure gas reservoir (usually less than 7,000 psia) with the cooling effect, while it is the opposite for high-pressure gas reservoir (more than 10,000 psia) wherein the gas behaves like a liquid. We observed an unusual phenomenon for the gas reservoir pressure between 9,000 psia and 10,000 psia; that is, the reservoir fluid temperature slightly increases with expansion, reaches a

plateau, and then gradually starts to decline as the lower pressure gas moves towards the wellbore. The reason is that the gas reservoir heating/cooling is due to J-T coefficient variations, which is sensitive to pressure changes and could be calculated by an equation of state. Mao and Zeidouni (2017) presented an analytical solution with consideration of the AE effect but ignored the heat exchange with the over- and under-burden formations. By investigating their analytical solutions, we found that the effect of AE is very small and it is two orders of magnitude smaller than the J-T effect. The J-T effect is dominating in the near wellbore region and the radius investigation of AE effect is larger than that of J-T effect. To quantify the effect of AE at the wellbore, we give the expression

$$T_D(r_D = 1) = C_1[\ln(t_D + 2t_D^2) + 0.809 - \ln(C_2)] \quad (18)$$

where $T = \frac{\sigma_{JT} q \mu}{2\pi k h} T_D + T_i$, $r_D = r/r_w$. C_1 and C_2 are constant parameters defined in Mao and Zeridouni (2017). Based on our comprehensive semianalytical solution, we found that the heat exchange of fluid with over- and under-burden formations appear more important than the adiabatic expansion effect, especially at high-production rates. For gas reservoirs, the gas gains heat by exchanging heat with the surroundings at low pressures but loses heat to the surroundings at high pressures. At high gas rates, ignoring the AE effect may be appropriate, and a fully analytical solution was given to estimate the flowing-fluid temperature without sacrificing any accuracy.

5.5 Two-steps calculation

As shown in above sections, fluids pressure and temperature in the reservoir are dependent on each other. For an oil reservoir large pressure drop leads to temperature increment due to Joule-Thompson heating effect, in return, the increasing of temperature decreases the fluid viscosity,

thus alters the pressure. It requires to calculate fluids pressure and temperature in the reservoir simultaneously. The conventional method splits the reservoir into many calculation nodes and calculate each node pressure and temperature from reservoir outer boundary (r_e) to reservoir inner boundary (r_w). The calculation is still complicated even though we proposed simple analytical solutions. Usually the temperature and pressure at wellbore (r_w) are what we cared and can be coupled with wellbore heat transfer model (discussed in Chapter 6). To further simplify the calculation of P_{wf} and T_{wf}, we developed a two-steps calculation algorithm.

The two-steps calculation algorithm is:

1. Calculate μ at outer boundary ($\mathrm{r} = \mathrm{r_e}$): $\mu(P_e, T_{ei})$
2. At wellbore ($\mathrm{r} = \mathrm{r_w}$), assume $\mu_{\mathrm{wb2}} = \mu(P_e, T_{ei})$, calculate $\mathrm{P_{wb}}$ and $\mathrm{T_{wb}}$
3. Calculate μ_{wb} at $\mathrm{P_{wb}}$ and $\mathrm{T_{wb}}$ condition: $\mu_{\mathrm{wb3}}(P_{wb}, T_{wb})$
4. At wellbore ($\mathrm{r} = \mathrm{r_w}$), with $\mu_{\mathrm{wb}} = \mu_{\mathrm{wb3}}(P_{wb}, T_{wb})$, calculate $\mathrm{P_{wb}}$ and $\mathrm{T_{wb}}$ again
5. At wellbore, assume $\mu_{\mathrm{wb}} = x * \mu_{wb3} + (1 - x)\mu_{wb2}$, calculate $\mathrm{P_{wb}}$ and $\mathrm{T_{wb}}$; x is defined as viscosity coefficient: if x =0, it means that initial viscosity $\mu(P_e, T_{ei})$ is used at wellbore; if x=1, it means that one-step calculated viscosity $\mu_{\mathrm{wb3}}(P_{wb}, T_{wb})$ is used at wellbore.

Noticed that the two-steps calculation is not applicable to gas reservoir since gas is compressible fluid. Its properties are a strong function of both temperature and pressure. The two steps calculation is not able to capture the gas properties variances. In this part, we will only show how to use two-steps calculation to estimate P_{wf} and T_{wf} simultaneously for single-phase oil reservoir.

The transient pressure behavior is given by the following equation:

$$\mathrm{P(r,t)} = \mathrm{P_i} - \frac{70.6qB\mu}{kh}\left[-E_i\left(-\frac{948\phi\mu c_t r^2}{kt}\right)\right] \tag{19}$$

At the wellbore, if skin factor is considered, the following equation is used:

$$\mathrm{P}_{wf} = P_i - \frac{162.6q\mu B}{kh}[\log(t) + \log\left(\frac{k}{\phi\mu c_t r_w}\right) - 3.23 + 0.87S \tag{20}$$

The analytical transient temperature behavior is given by Eq. 16. If $\mathrm{t} > \mathrm{t}_{\mathrm{pss}} = \frac{1200\phi\mu c_t r_e^2}{k}$, the pseudo-steady condition is reached, the pressure can be calculated by:

$$\mathrm{P} = \mathrm{P}_{\mathrm{i}} - \frac{141.2qB\mu}{kh}[\ln\left(\frac{r_e}{r}\right) + \frac{r^2}{2r_e^2} - \frac{1}{2}] \tag{21}$$

If steady-state condition is reached, the steady-state pressure is given by

$$\mathrm{P} = \mathrm{P}_{\mathrm{i}} - \frac{141.2qB\mu}{kh}\ln\left(\frac{r_e}{r}\right) \tag{22}$$

The steady-state temperature can be obtained if time is longer enough so that the second term in Eq. 16 is equal to zero. The steady-state temperature is written as:

$$T = T_{ei} - \frac{C}{2B}\, e^{\frac{Dr^2}{2B}} Ei\left[-\frac{Dr^2}{2B}\right] \tag{23}$$

Using the data from Mao and Zeidouni (2017). An oil reservoir with $P_i = 21{,}000$ psi and $T_{ei} = 302$ °F. The constant production rate is 2,080 STB/D and production time is $50 \text{ days} < \mathrm{t}_{\mathrm{pss}}$. Transient pressure and temperature models are used. Figure 25 and Figure 26 show the results. At x=0.814, the T_{wf} between two-steps calculation and multi-steps calculation matched and the pressure difference at wellbore is 105 psi. Compared with the total pressure drop of 3,200 psi, this pressure difference is relative small. The value of x during transient period is changing with time.

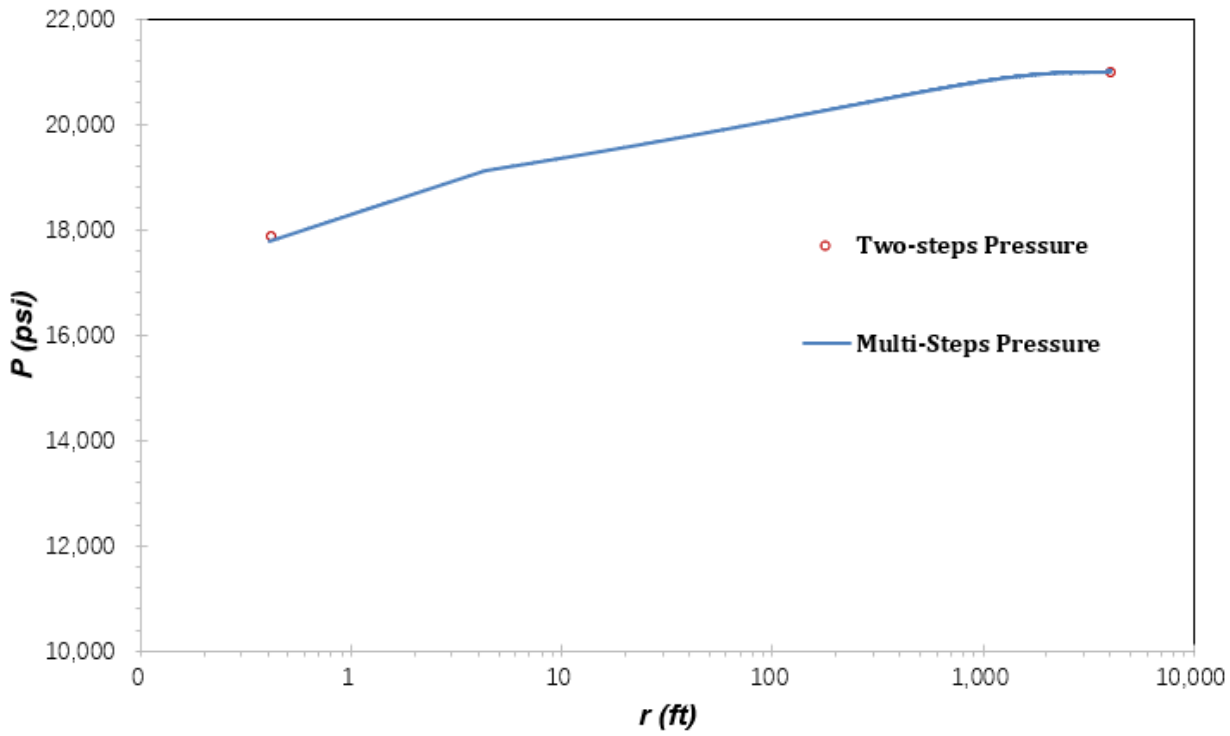

Figure 25-Pressure distribution in the reservoir: comparing multi-steps calculation versus. Two-steps calculation

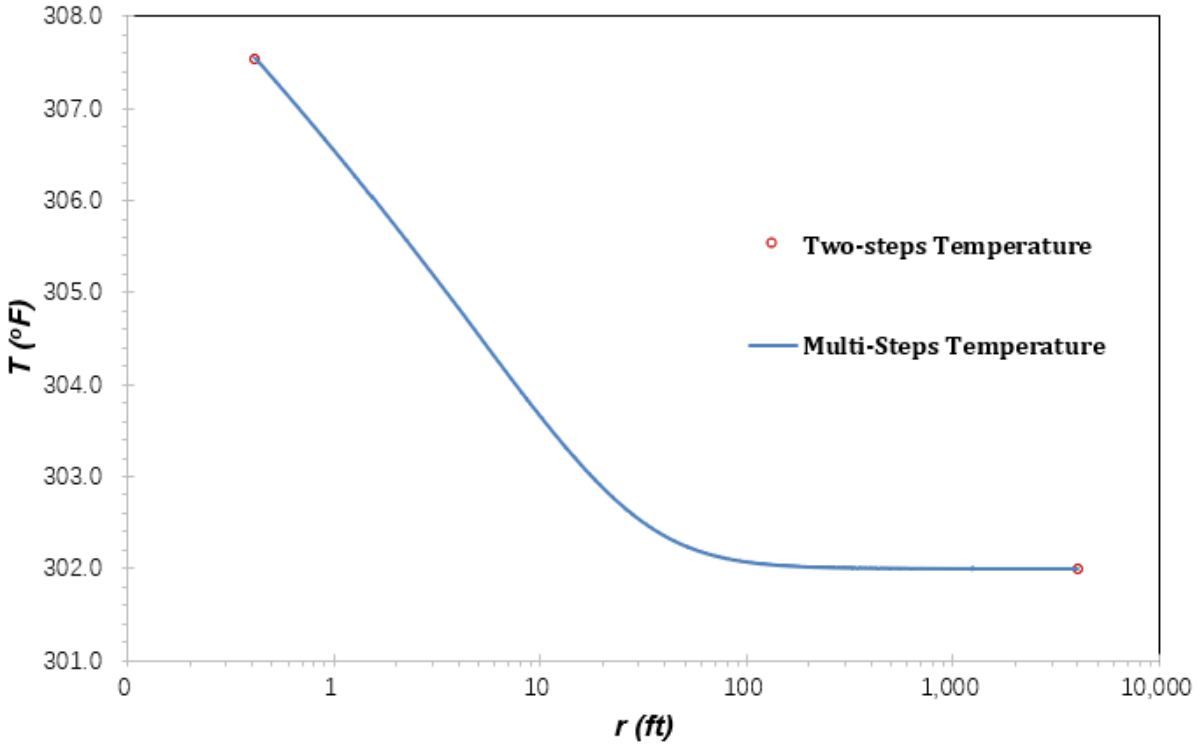

Figure 26-Temperature distribution in the reservoir: comparing multi-steps calculation versus. Two-steps calculation

For different producing time and production rate, the value of x is not fixed. Can we give a good approximate number or simple empirical correlation to represent x in that case P_{wf} and T_{wf} becomes easier? Usually, the life of a deepwater asset is long because of its high production rate and large capital cost. For a well with more than 10 years life, the steady-state pressure and temperature in the reservoir have been reached. We can use Eq. 22 and Eq. 23 with consideration of variance of viscosity and J-T coefficient to estimate pressure and temperature distribution in the reservoir (no time dimension). By using two-steps calculation, the approximate x value at different production rate is shown in Figure 27. The x value is obtained by honor the temperature calculation. In other words, the optimal x value is obtained by minimizing $\mathrm{T}_{\mathrm{wf}_{multi-steps}} - T_{wf\,_{two-steps}}$. The

orange line in Figure 27 represents the pressure difference at wellbore compared with original multi-steps calculation and proposed two-steps calculation.

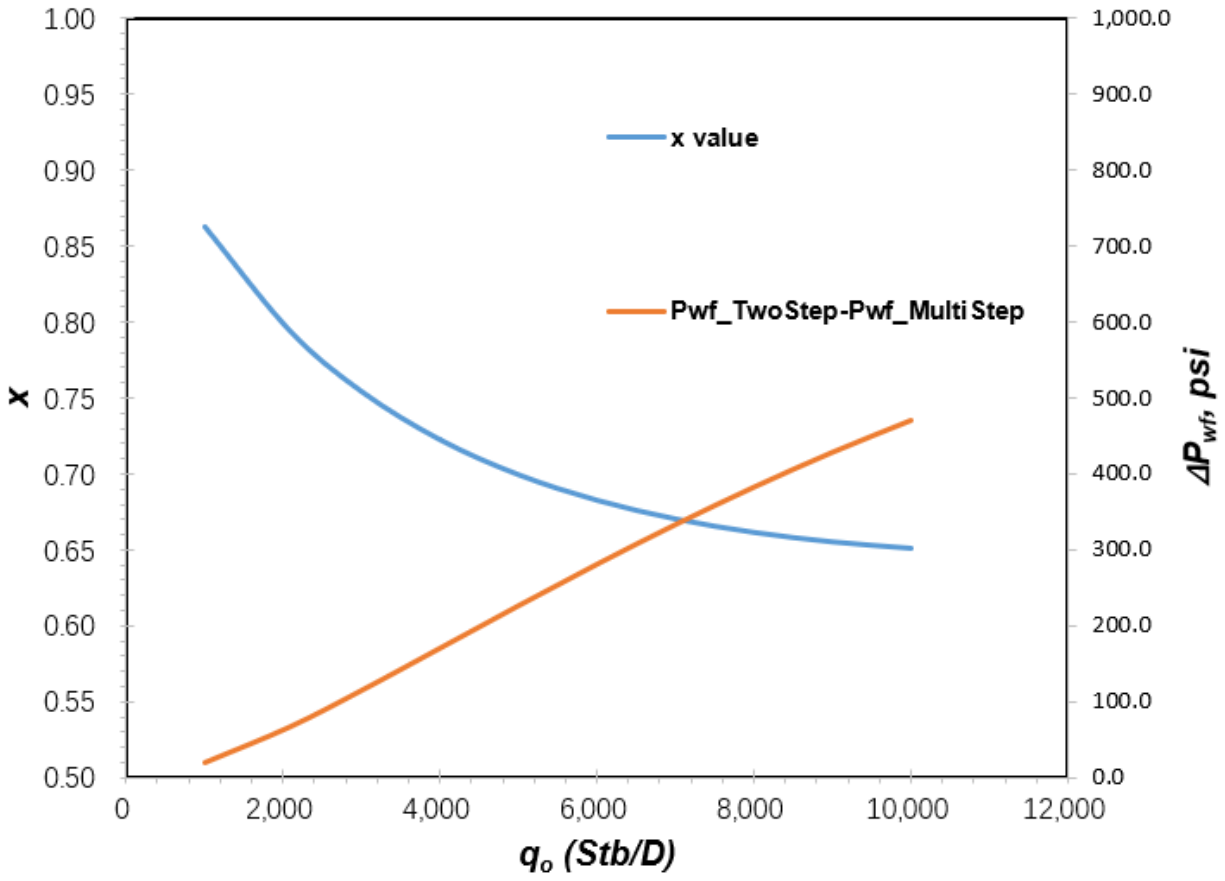

Figure 27-x value for steady-state condition and pressure difference at wellbore compared with multi-steps calculation

It is observed from Figure 27 that x value has an exponential relationship with production rate. We can use the following correlation between x and q_o for this oil reservoir, shown in Figure 28

$$x = a * exp(b * q_o) + c \tag{24}$$

Where

$$a = 0.316$$

$$b = -3.41 \times 10^{-4}$$

$$c = 0.641$$

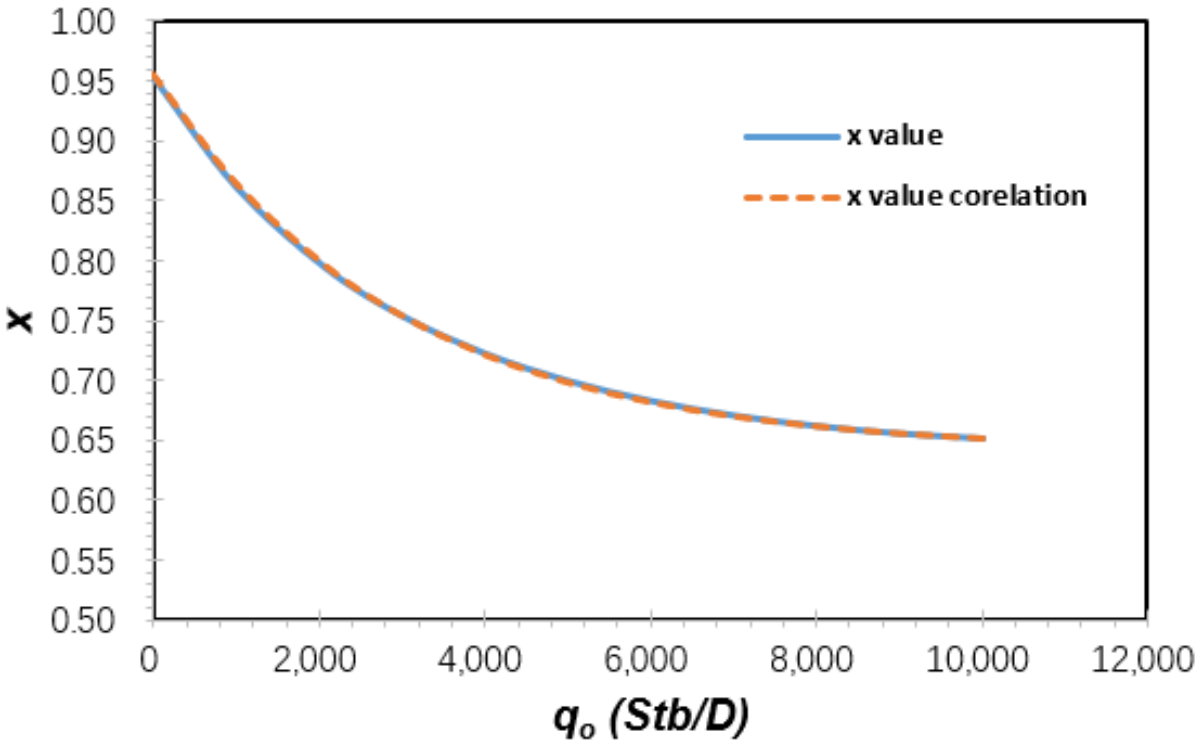

Figure 28-x value correlation

For different reservoir, it may have different parameters. However, the exponential relationship between x value and production rate q_o still exists. To further simplify we can used constant value x=0.65 for approximation without sacrificing two much accuracy. Figure 29 and Figure 30 show the pressure and temperature difference at wellbore compared two-steps calculation and multi-steps calculation with x=0.65. The maximum P_{wf} difference is 450 psi and maximum T_{wf} difference is 0.5 ^{o}F.

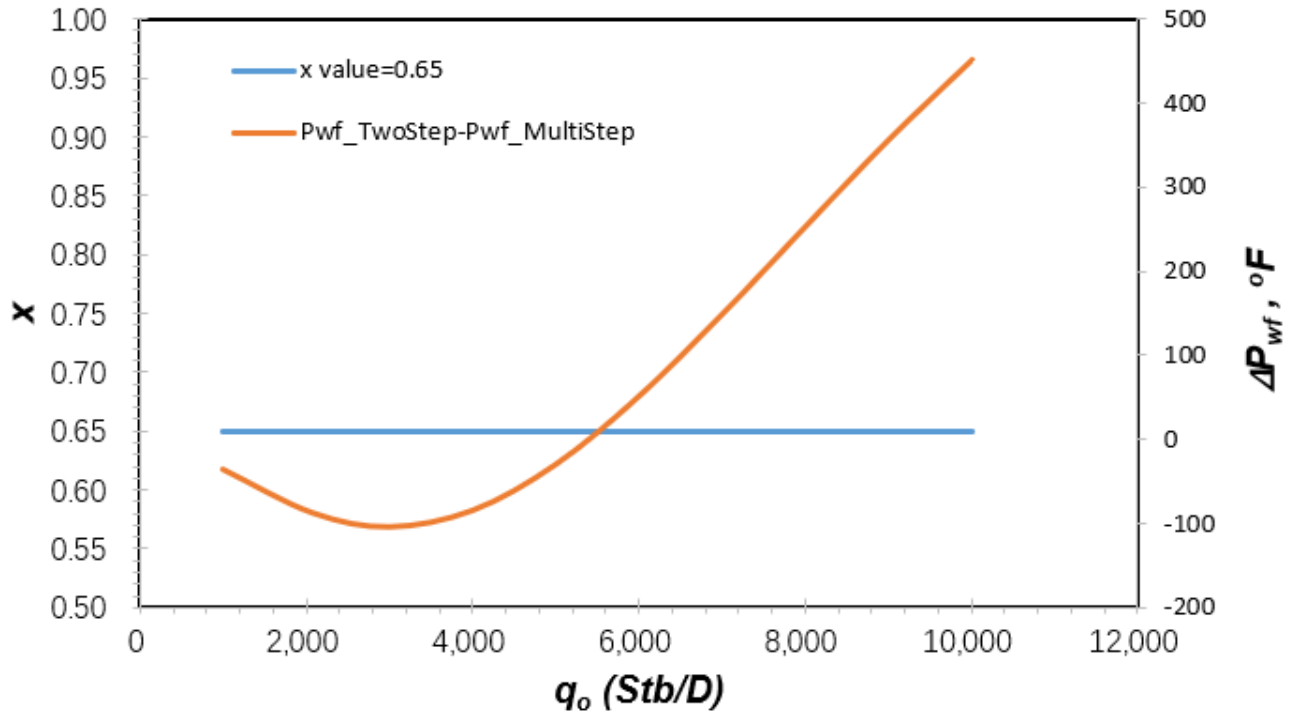

Figure 29-Pressure difference at wellbore compared two-steps and multi-steps calculation with x=0.65

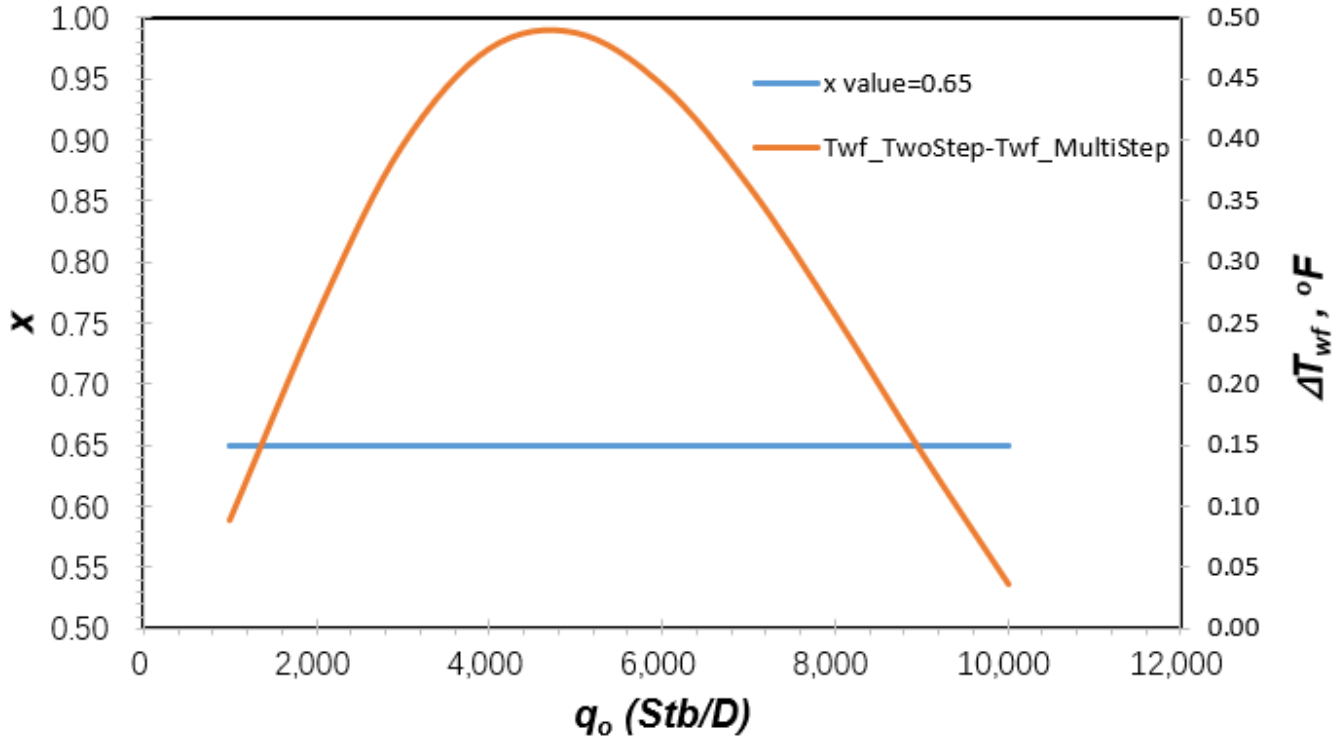

Figure 30-Temperature difference at wellbore compared two-steps and multi-steps calculation with x=0.65

6. COUPLED RESERVOIR/WELLBORE HEAT TRANSFER

6.1 Wellbore heat transfer model

The hydrocarbon fluid is flowing through the reservoir into the wellbore. Most wellbore heat transfer models include commercial software OLGA and Pipesim presumed that the fluid enters the wellbore at initial formation temperature, T_{ei}. According to the discussions in chapter 4, this assumption is not always true. We want to couple the reservoir/wellbore heat transfer model together since the fluid entering temperature at wellbore (r_w) is a variable. Hasan et al. (2009) presented a steady-state wellbore heat transfer model to estimate flowing fluid temperature in the wellbore. Consider a small control volume as Figure 31, the general energy balance equation is:

$$\frac{\mathrm{d}H}{\mathrm{d}z} - \frac{gsin\alpha}{Jg_c} + \frac{v}{Jg_c}\frac{\mathrm{du}}{\mathrm{d}z} = -\frac{Q}{w} \tag{25}$$

We set $z=0$ at wellhead and $z=L$ at bottomhole and the fluid is flowing in the upward direction. Combining Eq. 25 and Eq. D-1, we could obtain:

$$\frac{\mathrm{d}T_f}{\mathrm{d}z} = C_{JT}\frac{\mathrm{dP}}{\mathrm{d}z} + \frac{1}{c_p}\left(-\frac{Q}{w} + \frac{gsin\alpha}{Jg_c} - \frac{v}{Jg_c}\frac{\mathrm{du}}{\mathrm{d}z}\right) \tag{26}$$

The heat influx from the formation to the wellbore fluid per unit length of wellbore is written as:

$$Q = -L_R w c_p (T_f - T_{ei}) \tag{27}$$

For a wellbore section surrounded by earth, L_R is given by Eq. 28, whereas Eq. 29 represents L_R for a section submerged in sea water:

$$L_R = \frac{2\pi}{c_p w}\left(\frac{r_{to}U_{to}k_e}{k_e + r_{to}U_{to}T_D}\right) \tag{28}$$

$$L_R = \frac{2\pi U_{to}}{c_p w} \tag{29}$$

Where r_{to} is tubing outside radius while U_{to} represent overall heat transfer coefficient based on tubing outside area. For the heat transfer during production in the sea water part, the natural current makes the forced convection the most likely heat transfer mechanism. The estimation of overall heat transfer coefficient, U_{to} is described by Hasan and Kabir (2018). We divide the entire wellbore into many computational nodes. We represent the temperature surrounding the wellbore, T_{ei}, as a linear function of measured depth, z. To account for different temperature gradient in various sections of the formation or seawater, multiple linear representation T_{ei} is used. Thus,

$$T_{ei} = T_{ei_j} - (L_j - z)g_{G_j}sin\alpha \tag{30}$$

In Eq. 30, T_{ei}, L_j, and g_{Gj} represent the values of geothermal temperature, measured depth, and surrounding temperature gradient applicable to the jth section. Combining Eq. 26 to Eq. 30, we can obtain the following governing differential equation:

$$\frac{\mathrm{d}T_f}{\mathrm{d}z} = L_R(T_f - T_{ei}) - L_R(T_{ei_j} - z_j g_{G_j} sin\alpha) + \frac{gsin\alpha}{c_p J g_c} - \phi' \tag{31}$$

Where the variable ϕ' lumps the kinetic energy and J-T effect term, which is given by:

$$\phi' = \frac{v}{c_p J g_c}\frac{\mathrm{d}u}{\mathrm{d}z} - C_{JT}\frac{\mathrm{d}p}{\mathrm{d}z} \tag{32}$$

Assuming terms other than T_f in Eq. 31 are invariant with well depth, Eq. 31 becomes a first-order linear-differential equation with the following solution (Hasan et al., 2009):

$$T_f = T_{ei} + \frac{1 - e^{(z-L)L_R}}{L_R}\left[g_G sin\alpha + \phi' - \frac{gsin\alpha}{c_p}\right] + e^{(z-z_j)L_R}(T_{f_i} - T_{ei_j}) \qquad (33)$$

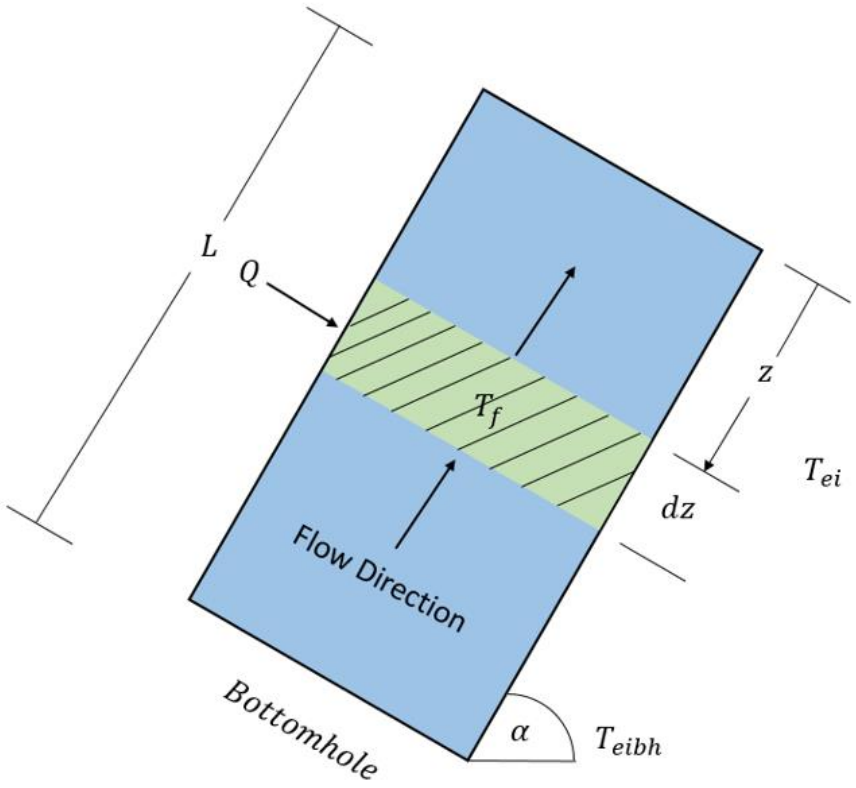

Figure 31-A control volume: energy balance for the wellbore flowing fluid

6.2 Model validation

Earlier, Kabir et al. (2014) presented a case study of offshore wells in West Australia with multi-depth temperature sensors installed in the relay stations at about 1,000 ft depth interval for transmitting downhole pressure data; Figure 32 depicts the relay stations. These temperature sensors constitute a part of acoustic telemetry system designed to transmit transient pressure and temperature measurements that are being made at the well bottom to surface in real time during the conduct of the drillstem test. Note that these discrete temperature sensors have a resolution of 0.03125^{o}C with an accuracy of ±1.5^{o}C. A drillstem test was conducted involving measurement of

transient pressure and temperature data at the well bottom. Followed by a 12-hour shut-in period, the well flowed for 50 hours with four different flow rates: 14.4, 25, 35, and 44 MMscf/D, as Figure 33 shows.

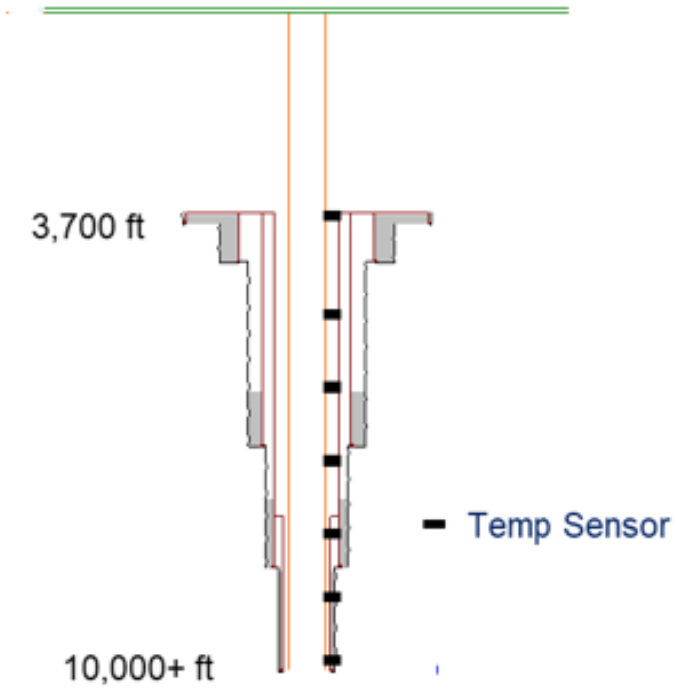

Figure 32-Typical wellbore setting with relay station

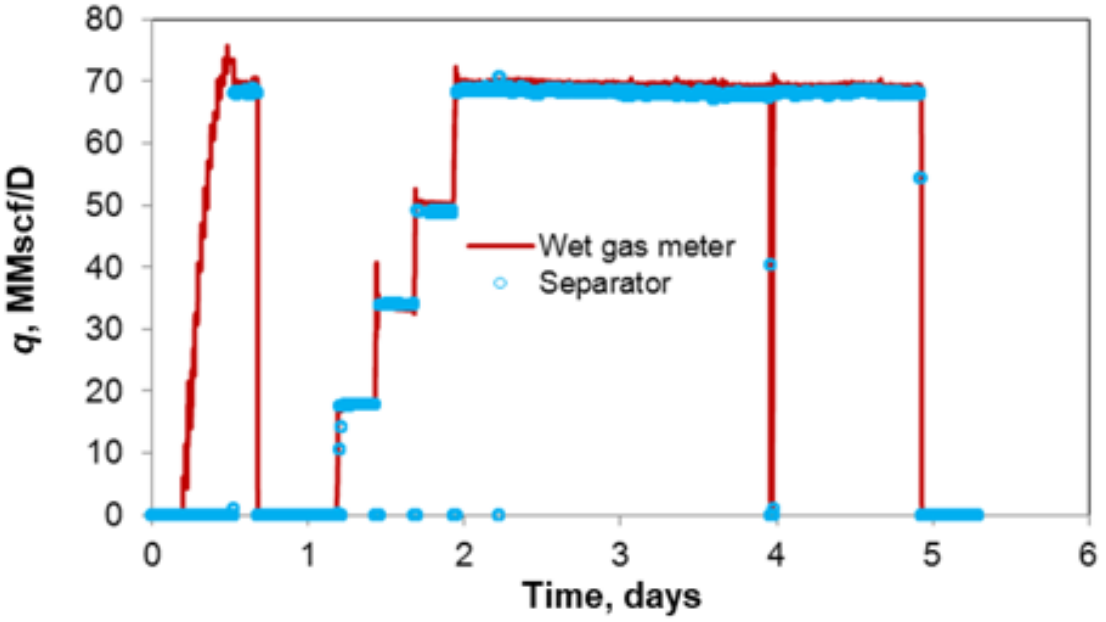

Figure 33-Validation of flow rates with two independent measurements

The initial pressure and temperature were reported to be 4,021 psi and 182 ^{o}F. Table 5 shows the related reservoir properties in this field study.

Parameter	Value	Unit
Permeability	35	md
Porosity	10	%
Formation Thickness	150	ft
Initial Formation Temp.	182	^oF
Initial Formation Pressure	4021	psi
Gas Saturation	70	%
Wellbore Radius	0.5	ft
External Formation Radius	4000	ft
Gas Specific Heat	0.7	Btu/(lb-^oF)
Formation Specific Heat	0.24	Btu/(lb-^oF)
Formation heat transfer coeff.	0.92	Btu/(hr-ft^2-^oF)

Table 5-Reservoir properties in this field study

Figure 34 shows the temperature distribution in the reservoir. Clearly, the gas entering the wellbore is somewhat cooler than the initial formation temperature. As expected, at the highest flow rate of 44 MMscf/D, this system exhibits the most J-T cooling effect in a relative scale.

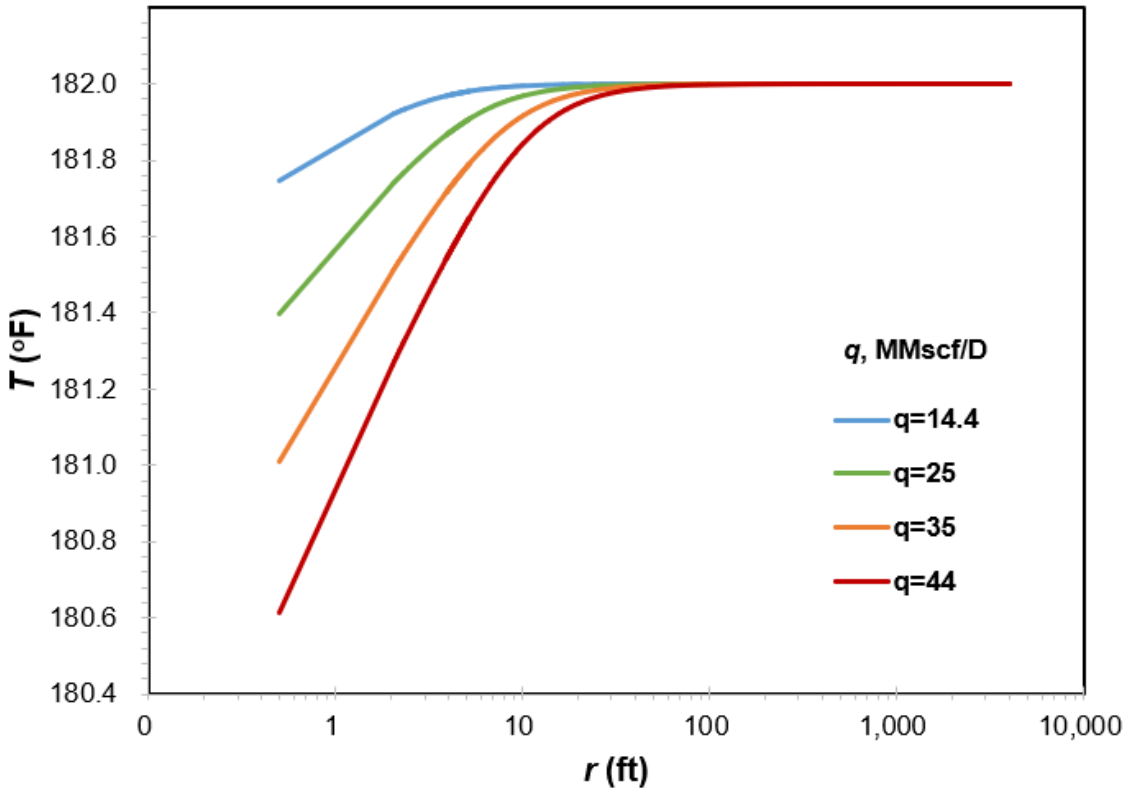

Figure 34-Field case study: temperature distribution with different flow rates

The wellbore heat transfer model is then coupled to the reservoir model. Figure 35 shows the wellbore fluid temperature distribution with variant bottomhole temperature profiles with the solid lines representing the simulated temperature and the symbols represent the PDG measurements. An error analysis followed and compared with the previous study of Kabir et al. (2014); we observed an improved accuracy of about 2%. We contend that whenever the J-T effect plays a more significant role, the use of the coupled wellbore/reservoir modeling will become imperative. In this case, the high reservoir permeability precipitated this insignificant temperature variance at the sandface.

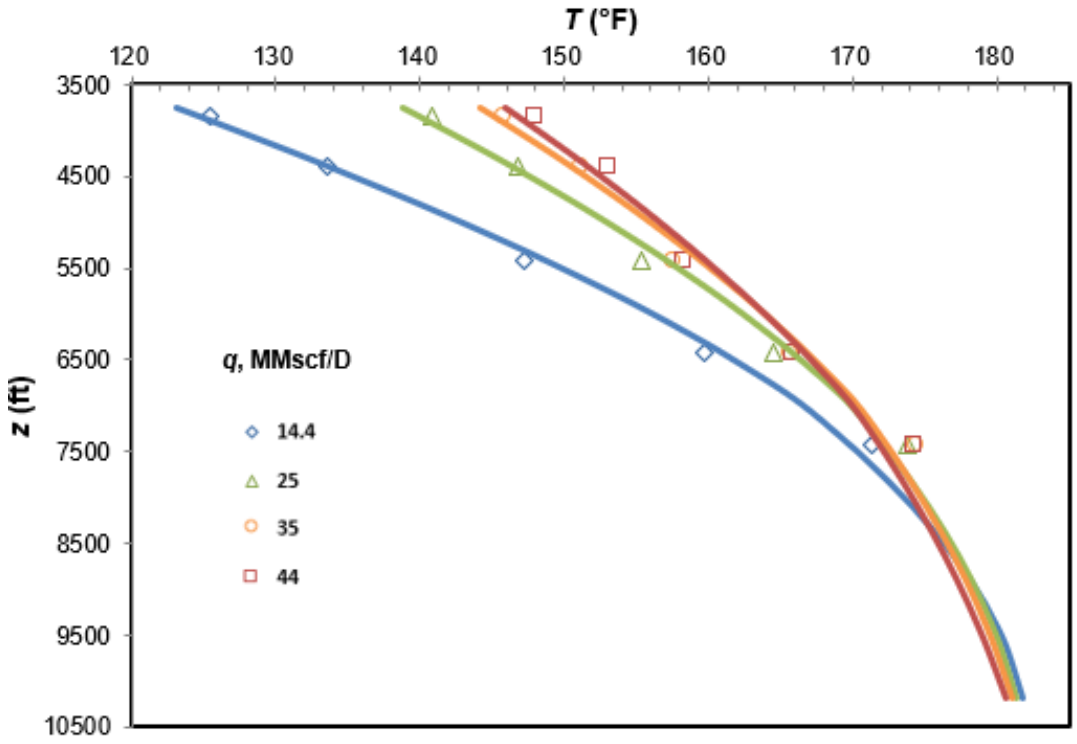

Figure 35-Field case study: temperature distribution along the wellbore

6.3 Coupled reservoir/wellbore application

After reservoir heat transfer model validation, we could apply the model to Well A. The main flow period for Well A is about 30 hours. The single-phase gas is flowing from the reservoir to the wellbore and from wellbore to the surface. The measured flow rate during this period is 10,000 *Mscf/D*. By using the nonisothermal reservoir flow model we developed, the temperature distribution for Well A is shown in Figure 36. The fluid temperature enters the wellbore at 139. 1 ^{o}F. Coupling the nonisothermal reservoir flow model with the wellbore heat transfer model, the temperature distribution in the wellbore is shown in Figure 37. The producing fluid continuously loses heat in the formation portion and begins to receive heat from seawater near the surface.

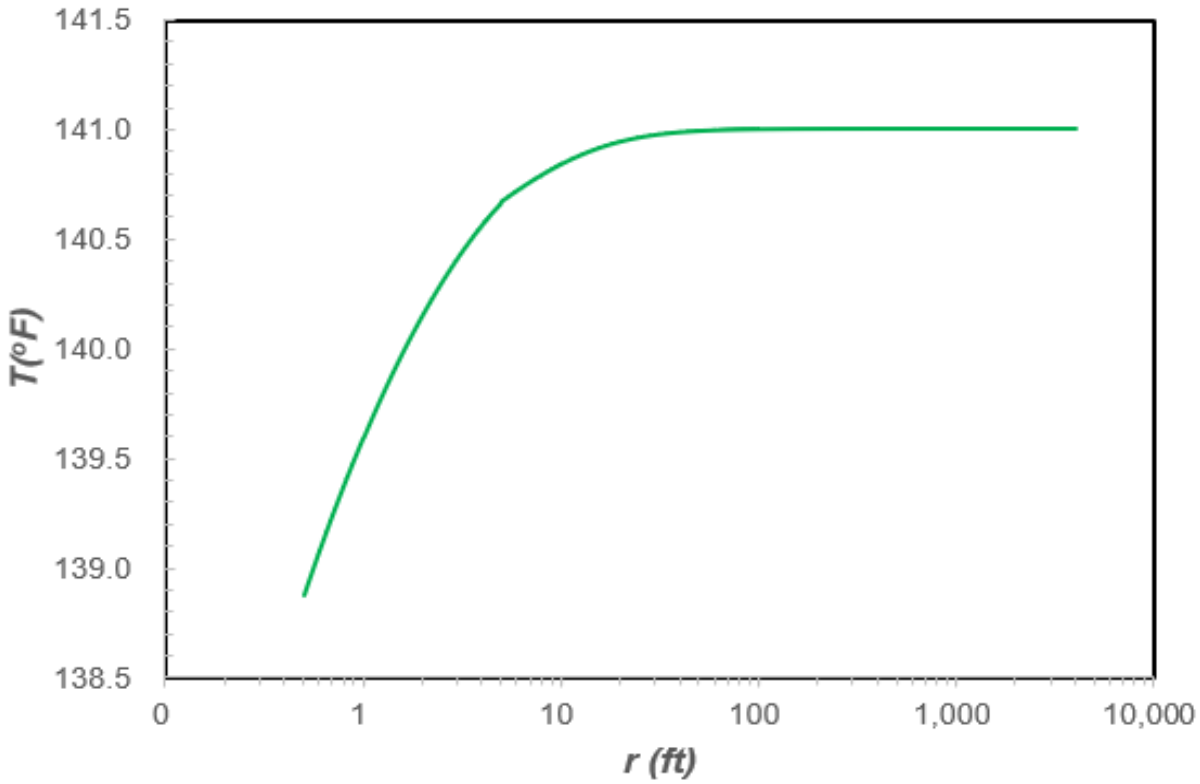

Figure 36-Well A: Temperature distribution in the reservoir with 30-hours producing time

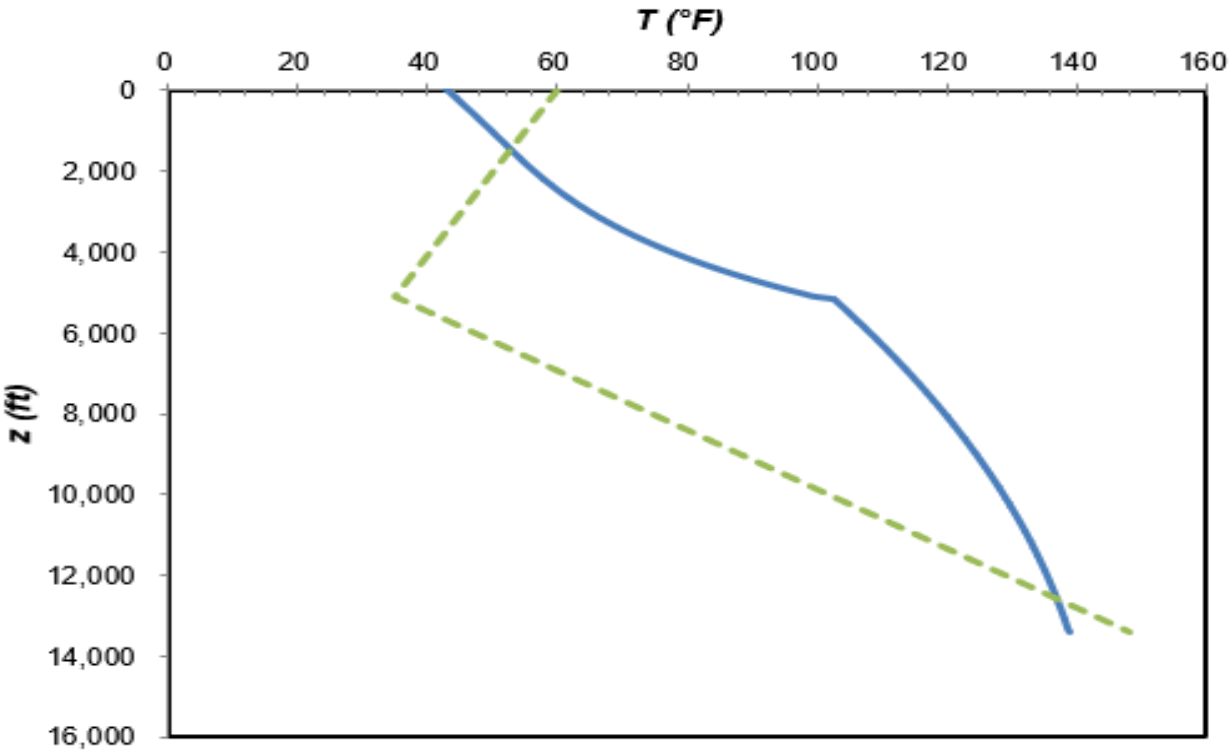

Figure 37-Well A: Temperature distribution in the wellbore with 30-hours producing time

7. GEOTHERMAL RECOVERY FROM ABANDONDED OIL WELLS

7.1 Introduction

The schematic of an abandoned petroleum is recompleted and serves as a coaxial double-pipe heat exchanger, shown in Figure 38. For vertical cased-hole abandoned wells, the recompletion includes sealing the well bottom and installing the insulation layer around the tubing pipe. The insulation layer between the inner tubing and outer tubing can be air-gaps, foams or other insulation materials. The working fluid is injected through the annulus between the casing and the outer tubing. The fluid is heated by the formation and flows back to the surface through the inner tubing. During flowing back, the fluid in the tubing consciously lose heat to the annulus. The amount of heat loss dependent on the temperature difference and the overall heat transfer coefficient between tubing and annulus. Production tubing insulation is crucial for the design of abandoned wells for geothermal energy production. The heat extraction efficiency is directly influenced by the material and thickness of the insulation layer. In an ideal situation, a thick insulation layer with a small thermal conductivity is favorable.

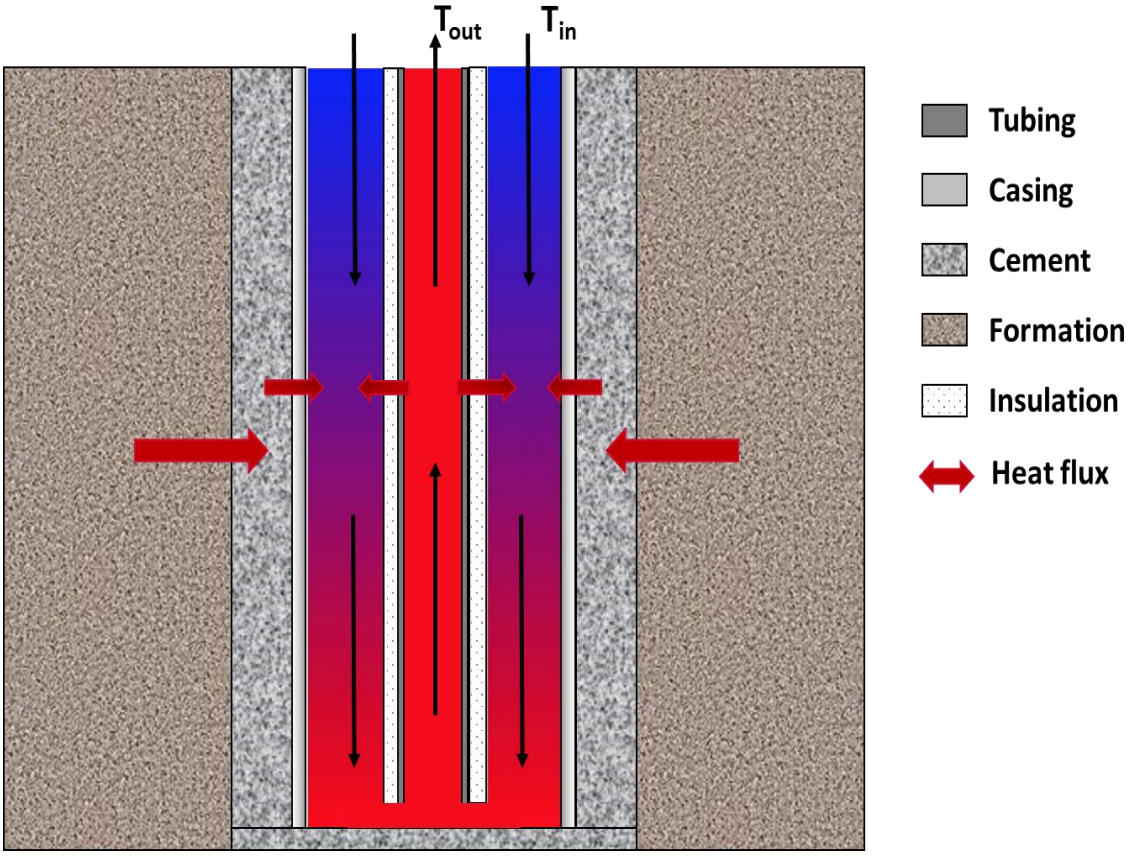

Figure 38-Schematic of the geothermal energy production system recompleted from abandoned wells

7.2 Model development

In this study, we developed three models for analyzing the geothermal recovery from abandoned petroleum wells: fully numerical model, semi-numerical model and fully analytical model. The fully numerical model solved a coupled wellbore formation system numerically. The semi-numerical model solved the wellbore system numerically and the formation system analytically. The analytical model solved both wellbore and formation systems analytically. To set up the mathematical model, the following assumptions are made:

- Constant formation thermal properties
- Constant working fluid properties in the wellbore

- Kinetic energy is ignored
- No wellbore heat storage effect
- Stable injecting condition during fluid circulation

7.2.1 Fully numerical model

The fully rigorous numerical model is first discussed to given a comprehensive understanding. The following semi-numerical and fully analytical are developed based on the simplifications of the numerical model. The formation and the wellbore are considered as two separated media and coupled at wellbore formation interface. The formation portion only has heat conduction and Eq. 32 shows the two-dimensional governing equation of formation heat transfer:

$$\rho_e c_e \frac{\partial T_e}{\partial t} - K_e \left(\frac{\partial^2 T_e}{\partial r^2} + \frac{1}{r} \frac{\partial T_e}{\partial r} + \frac{\partial^2 T_e}{\partial z^2} \right) = 0 \tag{34}$$

In Eq. 34, T_e is the formation temperature, $\rho_e c_e$ is the formation volumetric heat capacity, and K_e is the formation heat conductivity. Two energy balance equations are set up for the wellbore: producing tubing and injecting tubing. For the production tubing in the wellbore (subscript with *p*), the energy conservation equation is:

$$A_p \rho_f c_f \frac{\partial T_p}{\partial t} + A_p \rho_f c_f v_{fp} \frac{\partial T_p}{\partial z} - 2\pi r_{to} U_{to} \left(T_i - T_p \right) = 0 \tag{35}$$

In Eq. 35, A_p is the cross-section area of the production tubing, v_{fp} is the fluid velocity in the tubing, $\rho_f c_f$ is the fluid volumetric heat capacity, T_p and T_i are the temperatures of producing and injecting fluid and r_{to} is the tubing outside radius. The overall heat transfer coefficient, U_{to}, between the producing pipe and the injecting pipe, is calculated by:

$$\frac{1}{U_{to}} = \frac{r_{to}}{r_{ti}h_f} + \frac{r_{to}\ln\left(\frac{r_{to}}{r_{ti}}\right)}{K_t} + \frac{r_{to}\ln\left(\frac{r_{inso}}{r_{to}}\right)}{K_{ins}} + \frac{r_{to}}{r_{inso}h_f} \tag{36}$$

In Eq. 36, K_t and K_{ins} are heat the conductivities of tubing and insulation, r_{ti} is the tubing inside radius. For the injecting tubing in the wellbore (subscript with *i*), the energy conservation equation is:

$$A_i\rho_f c_f \frac{\partial T_i}{\partial t} + A_i\rho_f c_f v_{fi}\frac{\partial T_i}{\partial z} + 2\pi r_{to}U_{to}(T_i - T_p) + 2\pi r_{co}U_{co}(T_i - T_{wb}) = 0 \tag{37}$$

In Eq. 37, A_i is the cross-section area of the injecting annulus, v_{fi} is the fluid velocity in the annulus, and r_{co} is the casing outside radius. The overall heat transfer coefficient between the injecting fluid and the formation, U_{co}, is calculated as follows:

$$\frac{1}{U_{co}} = \frac{r_{co}}{r_{ci}h_f} + \frac{r_{co}\ln\left(\frac{r_{co}}{r_{ci}}\right)}{K_c} + \frac{r_{co}\ln\left(\frac{r_{wb}}{r_{co}}\right)}{K_{cem}} \tag{38}$$

In Eq. 38, K_c and K_{cem} are the heat conductivities of casing and cement, r_{wb} is the wellbore radius, and r_{ci} is the casing inside radius. h_f in Eq. 36 and Eq. 38 is the convective heat coefficient which can be calculated using the Dittus-Boelter correlation:

$$h_f = \frac{0.023K_eR_e^{0.8}P_r^{0.4}}{d_e} \tag{39}$$

In Eq. 39, K_f is the fluid heat conductivity, R_e is the Reynolds number, and P_r is the Prandtl number. The feature size (equivalent diameter), d_e, for the producing pipe is $\mathrm{d_e} = 2r_{to}$, and for the injecting

pipe is $d_e = 2\sqrt{r_{ci}^2 - r_{to}^2}$. Eq. 36 and Eq. 39 are coupled through the heat flow boundary condition at the wellbore:

$$r\frac{\partial T_e}{\partial r}\Big|_{r=r_{wb}} = \frac{r_{co}U_{co}}{K_e}(T_i - T_{wb}) \tag{40}$$

where T_{wb} is the temperature at wellbore formation interface. Equations 34, 35 and 37 form a single set of nonlinear equations and can be solved simultaneously by the Newton Raphson method.

7.2.2 Semi-numerical model

In the semi-numerical model, the heat transfer in the formation is calculated by analytically solving the formation energy balance equation in radial direction:

$$\frac{\partial^2 T_e}{\partial r^2} + \frac{1}{r}\frac{\partial T_e}{\partial r} = \frac{\rho_e c_e}{K_e}\frac{\partial T_e}{\partial t} \tag{41}$$

The initial and boundary conditions are:

$$T_e = T_{ei}(t = 0) \tag{42}$$

$$Q = 2\pi K_e r\frac{\partial T_e}{\partial r}\Big|_{r=r_{wb}} \tag{43}$$

$$\frac{\partial T_e}{\partial r}(r \to \infty) = 0 \tag{44}$$

Eq. 41-44 is known as infinite cylindrical-surface source model and can be solved by Laplace transform in terms of dimensionless variables, $r_D = r/r_{wb}$ and $t_D = K_e t/(\rho_e c_e r_{wb}^2)$. The temperature at wellbore and formation interface (r_D=1) can be written as:

$$T_{wb} = T_{ei} + \frac{Q}{\pi^2 K_e}\int_0^1 \frac{1 - \exp(-t_D u^2)}{u^2}\cdot\frac{Y_1(u)J_0(u) - J_1(u)Y_0(u)}{J_1^2(u) + Y_1^2(u)}du \tag{45}$$

In Eq. 45, J_0 is the zero-order Bessel function of the first kind, J_1 is the first-order Bessel function of the first kind, Y_0 is the zero-order Bessel function of the second kind, and Y_1 is the first-order Bessel function of the second kind. We define the dimensionless transient heat conduction function, T_D, as follows:

$$T_D = \frac{2\pi K_e}{Q}(T_{ei} - T_{wb}) \tag{46}$$

Evaluation of T_D from Eq. 46 involves the integration of modified Bessel functions. Hasan and Kabir (2018) proposed the following algebraic expression for T_D, which accurately represents the solutions,

$$T_D = \ln[\exp(-0.2t_D) + (1.5 - 0.3719\exp(-t_D)\sqrt{t_D})] \tag{47}$$

Incorporating Eq. 46 into Eq. 37 can lead to a new energy conservation equation for the injecting fluid, with T_{wb} being eliminated:

$$A_i\rho_f c_f \frac{\partial T_i}{\partial t} + A_i\rho_f c_f v_{fi}\frac{\partial T_i}{\partial z} + 2\pi r_{ito}U_{ito}(T_i - T_p) + \frac{2\pi r_{co}U_{co}}{K_e + r_{co}U_{co}T_D}(T_i - T_{ei}) = 0 \tag{48}$$

The semi-numerical model numerically solves Eq. 35 and Eq. 48 simultaneously to obtain the temperature of injecting and producing fluids. In the derivation of analytical transient formation heat conduction solution (Eq. 47), it is assumed that the heat flow rate Q is constant. It is the major difference between the fully numerical model (that avoids the constant heat transfer assumption) and the semi-numerical model. The following model comparisons validate that this is a reasonable assumption.

7.2.3 Fully analytical model

In the fully analytical model, we assume the heat transfer in the wellbore is steady-state. Therefore, the energy conservation equations for the producing and injecting fluid are expressed as:

$$A_p \rho_f c_f v_{fp} \frac{\partial T_p}{dz} = 2\pi r_{to} U_{to} (T_p - T_i) \tag{49}$$

and

$$A_p \rho_f c_f v_{fp} \frac{\partial T_p}{dz} = 2\pi r_{to} U_{to} \left(T_p - T_i\right) + \frac{2\pi r_{co} U_{co}}{K_e + r_{co} U_{co} T_D} (T_i - T_{ei}) \tag{50}$$

The boundary conditions for above equations are:

$$\left.\frac{dT_p}{dz}\right|_{z=L} = 0 \tag{51}$$

$$T_i = T_{inj} (z = 0) \tag{52}$$

The analytical solution of the above equations is solved:

$$T_p = \alpha e^{\lambda_1 z} + \beta e^{\lambda_2 z} + M g_D + T_{ei} \tag{53}$$

$$T_i = (1 - \lambda_1 M) \alpha e^{\lambda_1 z} + (1 - \lambda_2 M) \beta e^{\lambda_2 z} + T_{ei} \tag{54}$$

The expressions of constant M, α, β, λ_1 and λ_2, and the detailed solution procedure are provided in Appendix E. In all three models, the fluid pressure along the wellbore is estimated by solving the continuity equation and pressure drop equation:

$$w = \rho_f v A = const \tag{55}$$

$$\frac{dp}{dz} = \rho_f g - \frac{f\rho_f v^2}{2d_e} \tag{56}$$

Where friction factor, *f*, is calculated as:

$$\frac{1}{\sqrt{f}} = -1.8\log_{10}[\left(\frac{\varepsilon}{3.7d_e}\right)^{1.11} + \frac{6.9}{R_e}] \tag{57}$$

In Eq. 57, ε is the tubing steel absolute roughness.

7.3 Case study

In this part, we presented a case study to illustrate the applications of the developed models. The related wellbore and formation parameters are summarized in Table 6. To be consistent with Geothermal Energy Association (GEA), we used SI unit in this part. The abandoned oil well is a vertical well with 3000 m depth. The thickness of the insulation layer is 0.01 m. The formation geothermal gradient is 0.035 K/m. The injecting fluid is water with 283.5 K and 2 MPa injecting temperature and pressure.

Parameter	Value	Unit
Well Depth	3000	m
Fluid Inlet Pressure	2	Mpa
Fluid Inlet Temperature	283.5	K
Bottom Formation Temper.	400	K
Formation Thermal Conduc.	1.8	$Wm^{-1}K^{-1}$
Formation Thermal Diffu.	1×10^{-6}	m^2s^{-1}
Geothermal Gradient	0.035	Km^{-1}
Inner Tubing ID	0.06	m
Inner Tubing OD	0.07	m
Outer Tubing ID	0.09	m
Outer Tubing OD	0.14	m
Cement OD	0.24	m
Steel Thermal Conduc.	57	$Wm^{-1}K^{-1}$
Cement Thermal Conduc.	2.3	$Wm^{-1}K^{-1}$
Insulation Thermal Conduc.	0.023	$Wm^{-1}K^{-1}$
Steel Absolute Roughness	0.0003	m

Table 6-Related parameters in case study

7.3.1 Model validation

First, the numerical model for transient formation heat transfer solution is compared with the analytical solution. A constant heat flow rate boundary of 100 W/m is used in both solutions. In the numerical solution, a cylindrical formation with a radius of 100 m is discretized into 200 grids with logarithmic spacing. Figure 39 shows the comparison of temperature at wellbore and formation interface by the numerical solution and analytical solution. The temperature difference by the two solutions is less than 0.3 K in a period of 100 days. The comparison verifies that the

numerical discretization and implementation of formation model is valid. It also indicates that the influence of heat transfer in z direction is small and could be ignored.

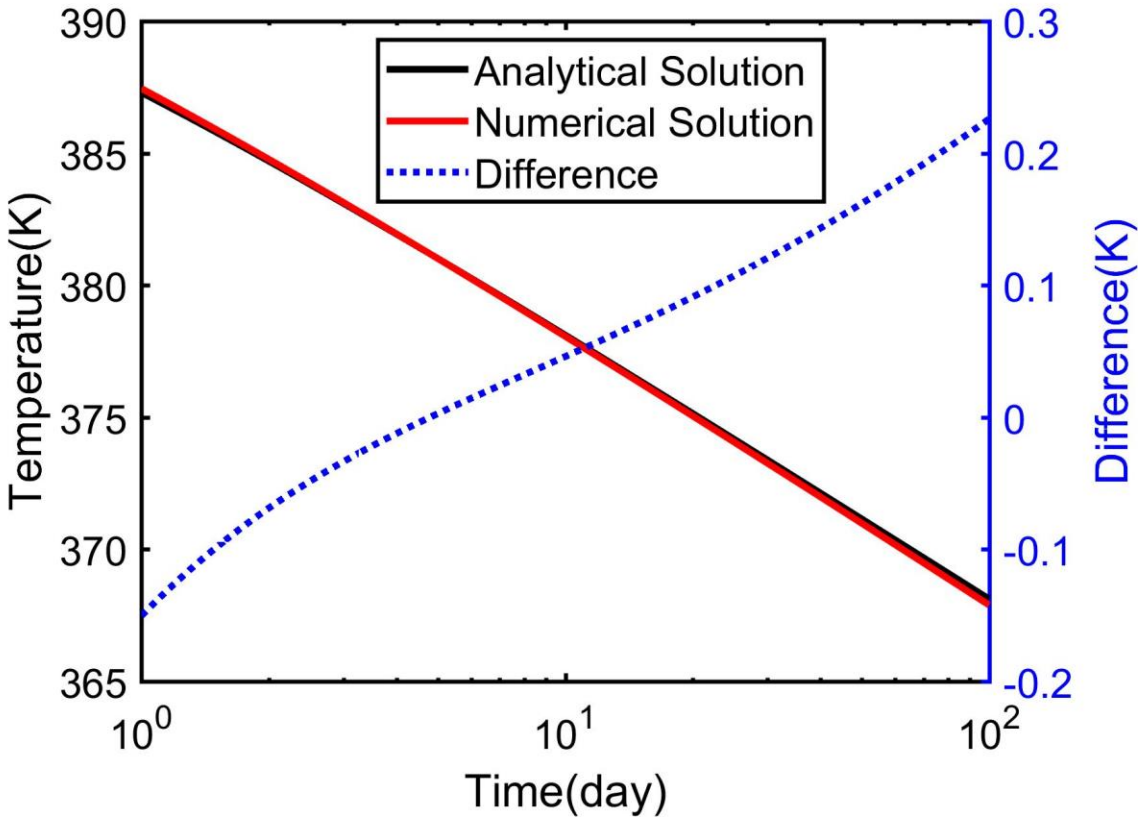

Figure 39-Comparing numerical solution and analytical solution for formation heat transfer

Next, the wellbore heat transfer model is verified by comparing the semi-analytical model with the fully analytical model. The only difference between the two models is the transient term. In analytical model, the time dependent term is ignored. This means that these two models should predict the same result if producing time is long and reaches the steady-state production period. The temperature profile along the wellbore after 100 days is shown in Figure 40. First, the vertical wellbore is discretized with 150 segments (dz=20 m). The temperature difference of the two

models during production and injecting is less than 0.09 K at 100 days of heat production. The steady-state has been reached at this time and the temperature difference between numerical and analytical model is very small. Then we want to find the transient temperature behavior period. Figure 41 compares the semi-numerical solution with difference discretized depth, *dz*. It is observed that for all difference *dz* values, the transient temperature behavior is within 1 day. The numerical solution converges to steady-state and the analytical model is adequate accurate to use.

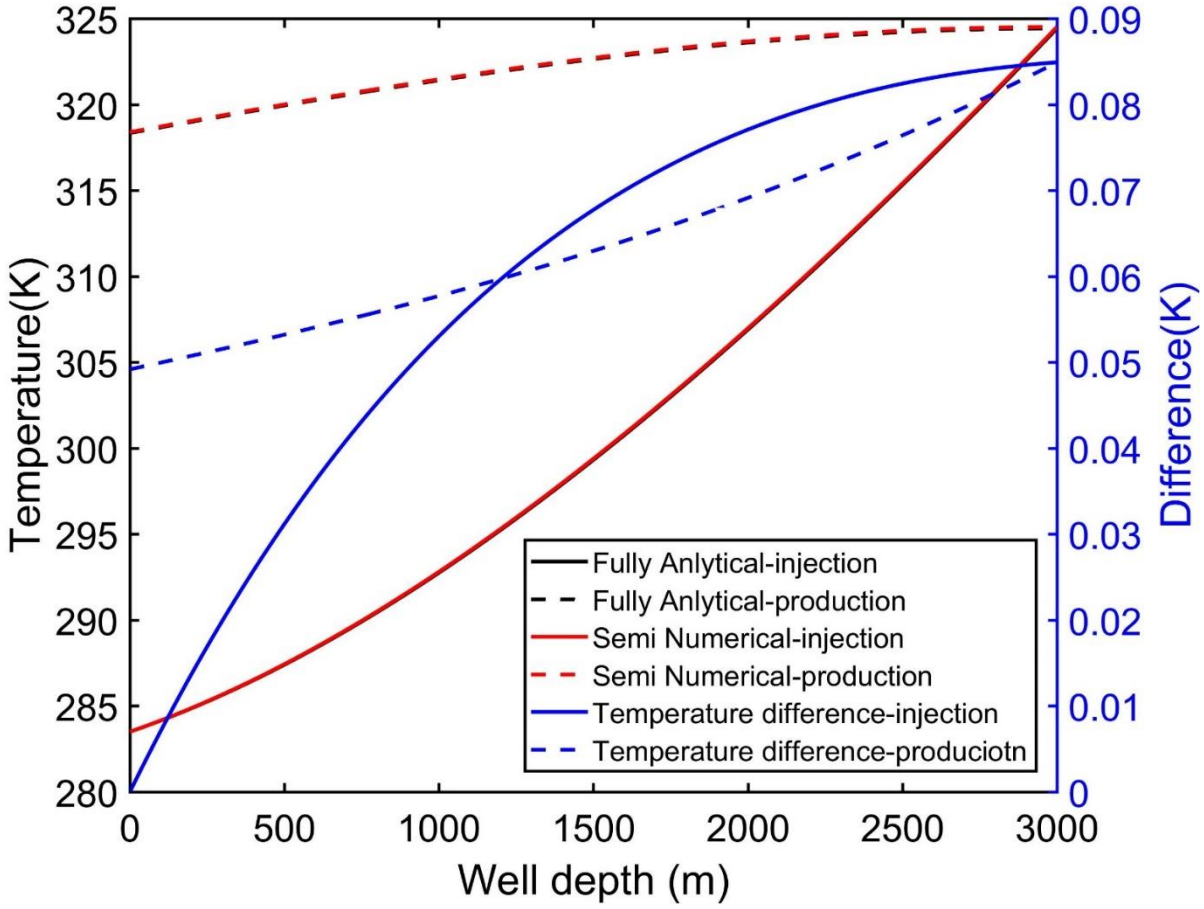

Figure 40-Comparing numerical model and analytical model for wellbore heat transfer

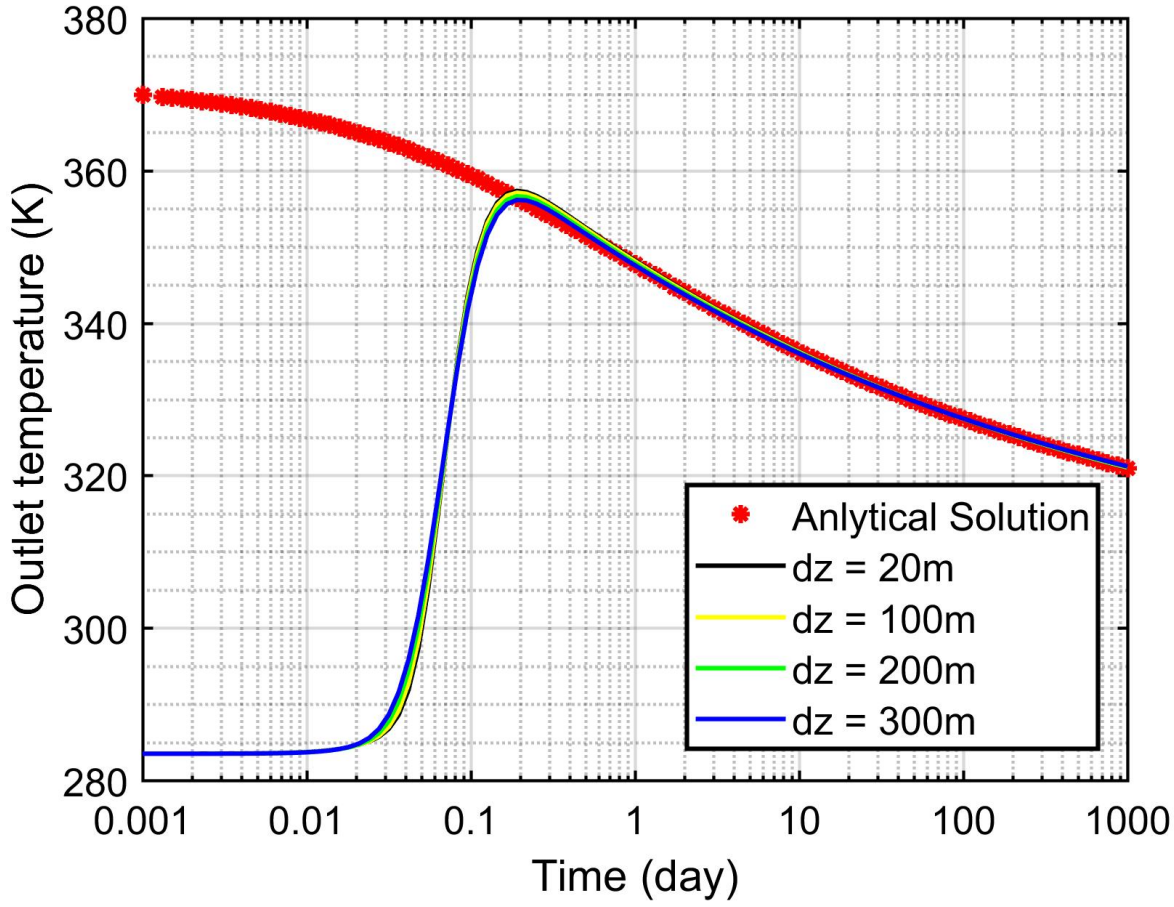

Figure 41-Comparing numerical model and analytical model for wellbore heat transfer with different dz

To further compare the three models. We apply the three models to evaluate a 100 days production cycle of the geothermal well described in Table 6. The inlet velocity of the working fluid is 0.2 m/s. Figure 42 compares the outlet temperature predicted by the fully numerical model with that predicted by the semi-numerical model. The T_D function is evaluated through the original Bessel integration. The outlet temperature of the working fluid decreases continuously throughout the production period. Initially, the fully numerical model predicts a slightly higher temperature than the semi-numerical model. At the later time, the semi-numerical model predicts a slightly

higher outlet temperature. The differences in estimation by the two models remain less than 1K, which is acceptable for the engineering design.

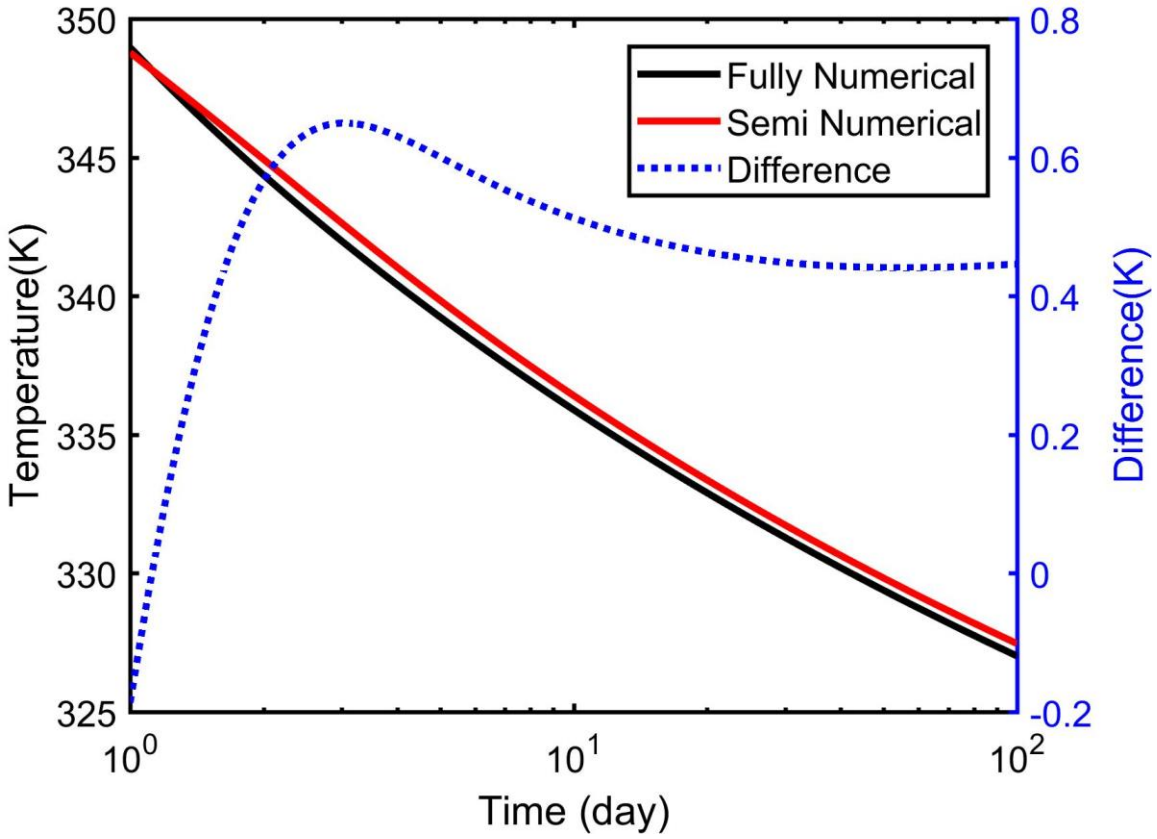

Figure 42-Outlet temperature comparison: fully numerical model and semi-numerical model

Figure 43 compares the outlet temperature predicted by the fully numerical model with that predicted by the fully analytical model. The fully analytical model applies the T_D function proposed by Hasan and Kabir. Similar to the semi-numerical model, the fully analytical model predicts a lower temperature initially, and a higher temperature at the later time. The results also demonstrate the feasibility of applying a simplified T_D function in modeling geothermal energy production from abandoned wells.

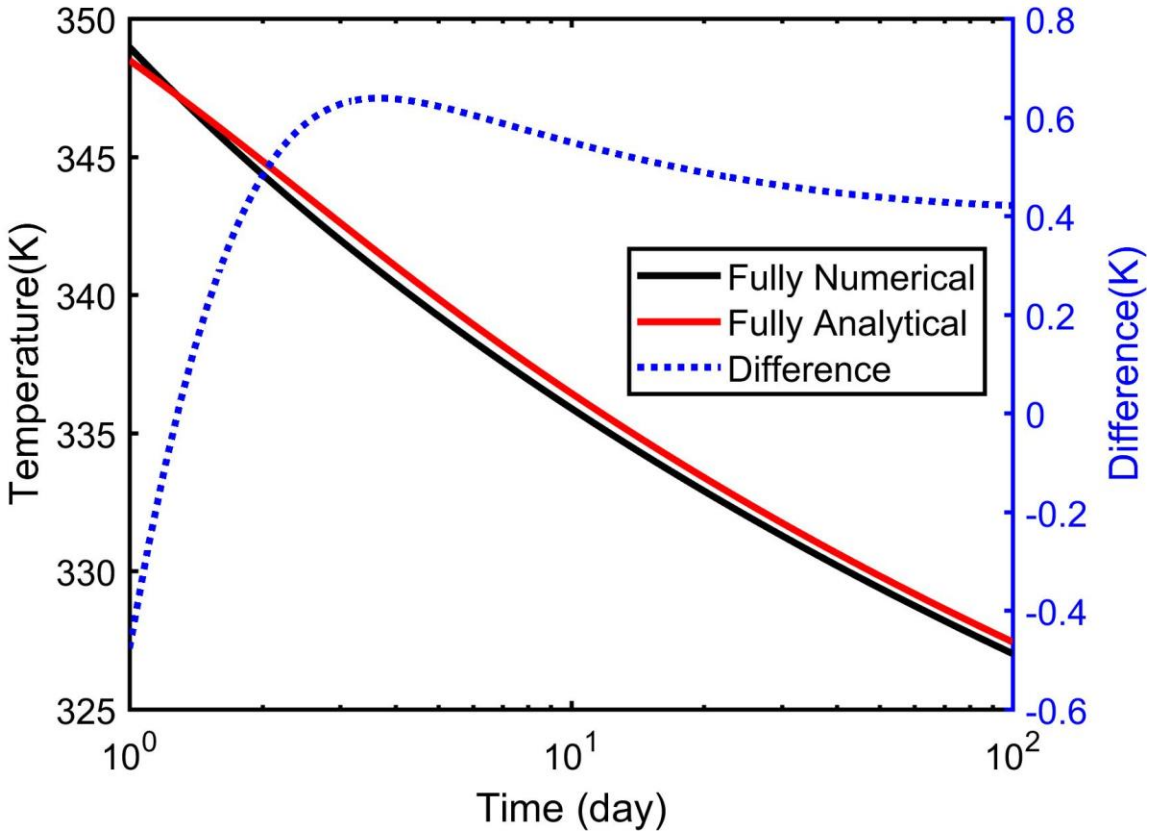

Figure 43-Outlet temperature comparison: fully numerical model and fully analytical model

Figure 44 presents the temperature distribution along the injecting pipe and the producing pipe at the 40th day of production. All three models predict a temperature increase from 283.5K to around 342.5K for the injecting pipe and a temperature loss of around 12K as the heated fluid being produced through the producing pipe. These comparisons indicate that, for the investigated geothermal production scenario, a steady state fully analytical model can estimate the simulation results of a transient fully numerical model with acceptable accuracy.

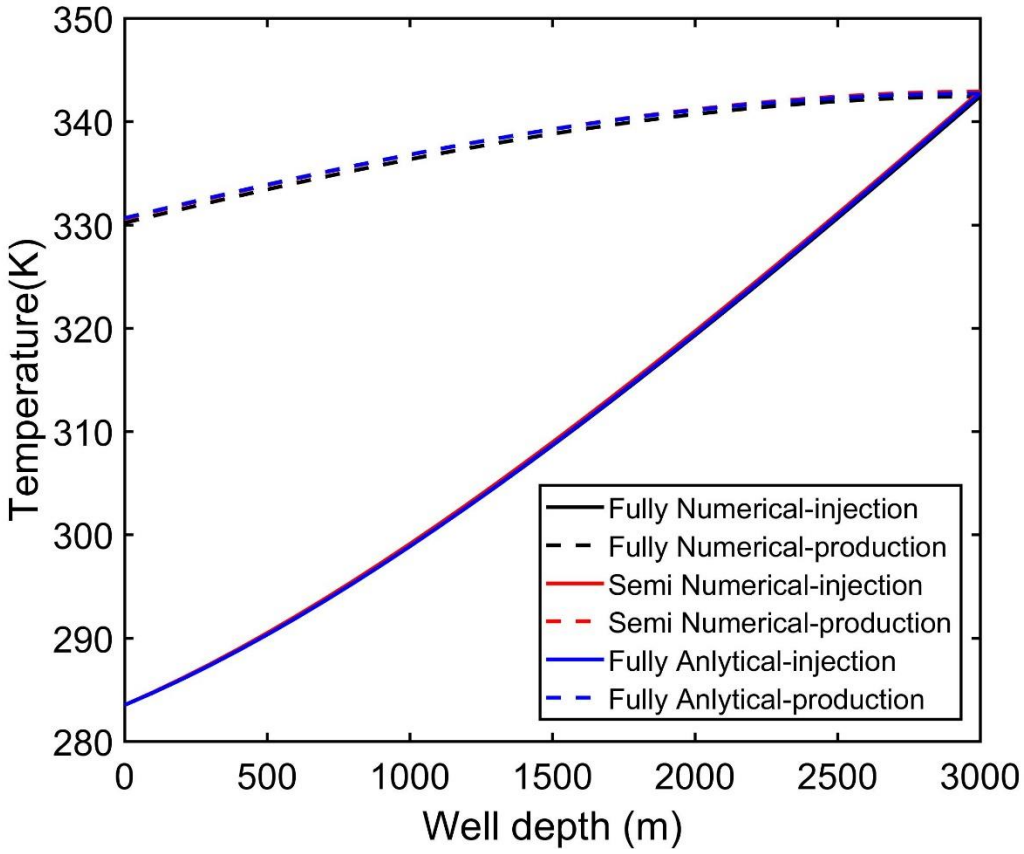

Figure 44-Temperature distribution comparison with 40 days circulation: fully numerical, semi-numerical and fully analytical

7.3.2 The effect of mass flow rates

The inlet mass flow rate of the working fluid is an important design parameter, which significantly influences the outlet temperature and the heat extraction rate. We apply two models to evaluate the impact of mass flow rate: one is the fully analytical model, and the other is the semi-numerical model with transient fluid properties. Figure 45 shows the outlet temperature at the 100^{th} day of production for mass flow rates from 0.27 kg/s to 4.5kg/s. Both models indicate the existence of a maximum outlet temperature of about 337.5K at a mass flow rate around 0.9kg/s. The explanation of the reversal in outlet temperature with mass flow rates lies in the fact that the system employed is a double-pipe heat exchanger. A low mass flow rate allows a longer time for

the injecting fluid to be heated by the formation, but also results in a longer time for the producing fluid to be cooled down. As the mass flow rate increases from 0.9kg/s to 4.5kg/s, the outlet temperature decreases to about 307.5K. The difference of the two models also increases to 0.4K at a mass flow rate of 4.5kg/s. Figure 46 depicts the total heat extraction rate at different mass flow rates. As the mass flow rate increases, the heat extraction increases monotonously, but the rate increase slows down. At higher mass flow rates, although the heat extraction still increases, fluid energy gained per unit mass decreases, leading to gradually lowering outlet temperature with increasing mass rates. The difference of the heat extraction rate predicted by the two models also increases to 5.5KW as the mass flow rate reaches 4.5kg/s.

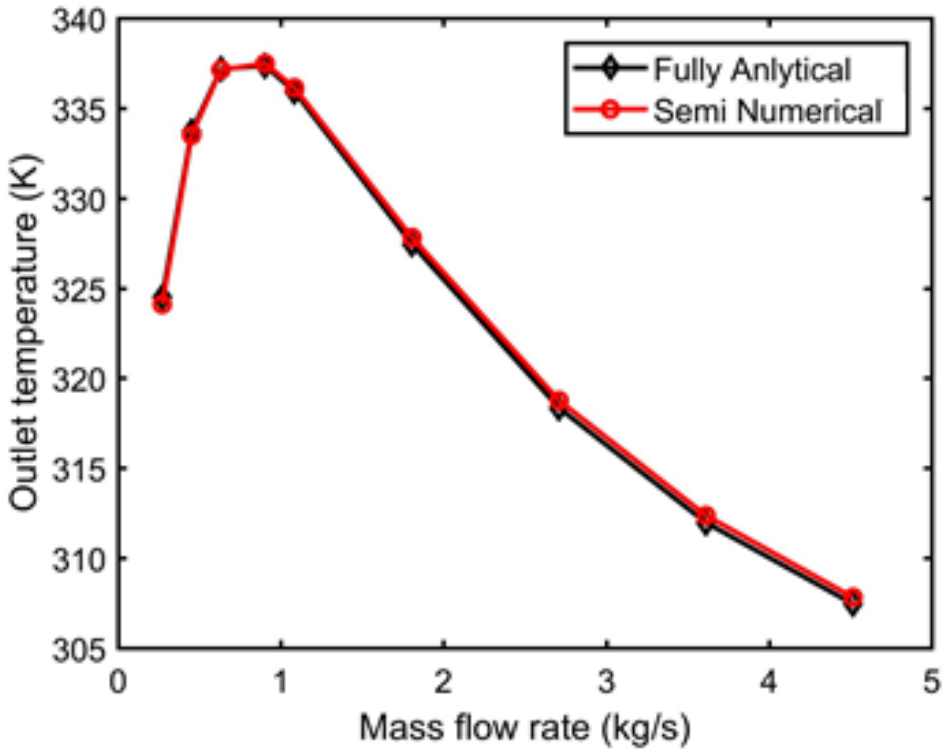

Figure 45-Outlet temperature at 100 days of production for different mass flow rates

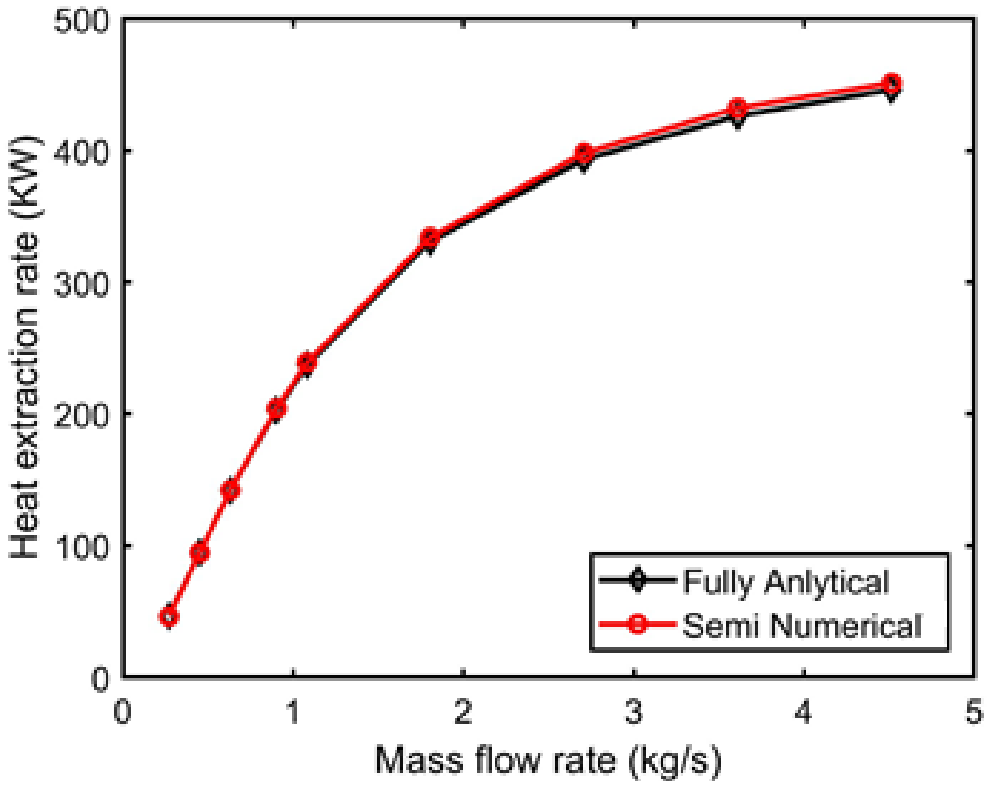

Figure 46-Heat extraction rate at 100 days of production for different mass flow rates

7.3.3 The effect of insulation layer properties

Production tubing insulation is crucial for the design of abandoned wells for geothermal energy production. The heat extraction efficiency is directly influenced by the material and thickness of the insulation layer. In an ideal situation, a thick insulation layer with a small thermal conductivity is favorable. However, it may not be an economic option when we consider the price of those materials. In this part, we would like to apply our model to give a reasonable range for the selection of the insulation material. The fully analytical model with an inlet velocity of 0.1m/s is applied for the analysis. Figure 47 presents the wellbore temperature distribution at 100 days with the insulation material of different thermal conductivities, $0.02 Wm^{-1}K^{-1}$, $0.05 Wm^{-1}K^{-1}$ and $0.1\ Wm^{-1}K^{-1}$. The thickness of the insulation layer is set as 1cm. The insulation material with high

thermal conductivity can lead to a quicker temperature increase for the injecting fluid, but also a higher temperature loss for the producing fluid. The outlet temperature is 56K, 41K and 29K higher than the inlet temperature for the 3 thermal conductivities from small to large respectively. Figure 48 presents the wellbore temperature distribution at 100 days with the insulation layer thickness of 0.5cm, 1cm and 2cm. The thermal conductivity of the insulation material is set as 0.06 $Wm^{-1}K^{-1}$. Similar to Figure 47, a quicker temperature increase for the injecting fluid and a higher temperature loss for the producing fluid can be observed for a thinner insulation layer. The outlet temperature is 26K, 38K and 50K higher than the inlet temperature for the insulation layer thickness of 0.5cm to 2cm respectively. The hot water produced from the abandoned wells can be directly used to heat the nearby residential buildings. For this application purpose, the thermal conductivity of the insulation material can be around $0.05Wm^{-1}K^{-1}$, and an appropriate thickness of the insulation layer should be around 1cm.

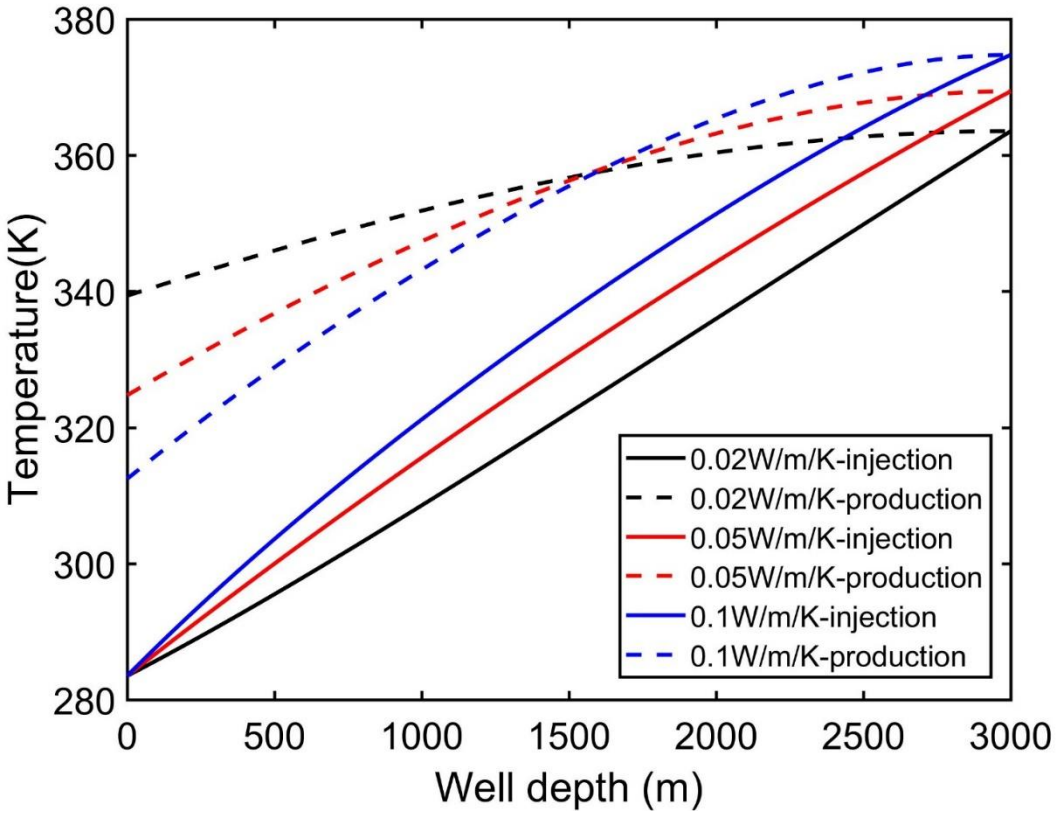

Figure 47-Temperature distribution along the injecting pipe and the producing pipe at 100 days of production for different thermal conductivities of the insulation material

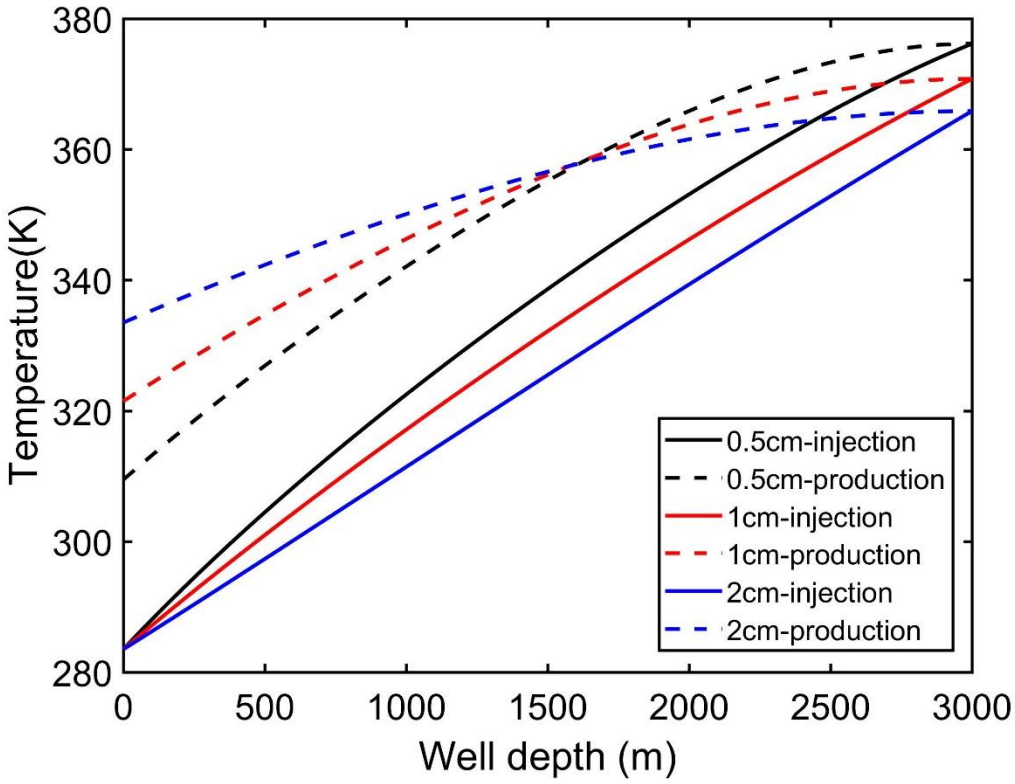

Figure 48-Temperature distribution along the injecting pipe and the producing pipe at 100 days of production for different insulation layer thickness

7.3.4 Economic analysis

The fully analytical solution is applicable for economic analysis and its simple and continuous format. In this section, we present how to use this analytical model to determine the optimal insulation width and mass flow rate to minimize the cost to generate geothermal power.

Define the cost of per unit generated power *C* as follows (Cui et al. 2017; Nian and Cheng, 2018):

$$C = \frac{TCI/CRF + AOC}{P_{net}} \tag{58}$$

In Eq. 58, *TCI* is the total capital investment estimated by the cost of heat exchanger (CC_h) and insulation (CC_i). Based on the analyzing results of Nian and Cheng (2018), we assume the pump purchasing and operation costs are 0.1 of the other equipment purchasing and operation costs.

$$TCI = 6.95 \times (CC_h + CC_I) \tag{59}$$

$$CC_h = \frac{280.74Q}{2200(T_{out} - T_{in})} + 746w \tag{60}$$

$$CC_i = \pi(r_{inso}^2 - r_{to}^2) \times L \times C_i \tag{61}$$

In Eq. 61, C_i is the cost of insulation and L is the length of the insulation. We consider two common applied insulation materials: urethane fiberglass and extruded polystyrene. Urethane fiberglass has a thermal conductivity of 0.021W/m/K with a cost of 214\$/m^3. The thermal conductivity of extruded polystyrene is 0.029W/m/K and the cost is 182\$/m^3 (Mahlia et al., 2007). The annual operation cost, *AOC*, is given as:

$$AOC = 1.1 \times (0.005 \times TCI + 24 \times V \times D \times F \times 0.022) \tag{62}$$

In Eq. 62, V is the volume flow rate in m^3 h^{-1}, D is the operation days each year, and F is the load factor. *CRF* is the cost recovery factor defined as follows:

$$CRF = \frac{i_{eff}(1 + i_{eff})^n}{(1 + i_{eff})^n - 1} \tag{63}$$

In Eq. 63, i_{eff} is effective rate of return and n is the project lifetime in years. The net power generation, P_{net}, is estimated by:

$$\mathrm{P_{net}} = \eta \times \int_0^D wc_f(T_{out} - T_{in})dt \tag{64}$$

Where η is the energy conversion efficiency. We intend to minimize the objective function, Eq. 58, under the following constraints:

$$\begin{cases} T^* - T_{out} \leq 0 \\ 0.002 \leq r_{inso} - r_{to} \leq 0.03 \\ 1 \leq w \leq 4 \end{cases} \tag{65}$$

In Eq. 65, T^* is the target outlet temperature. Table 7 gives the parameters for economic analysis. Figure 49 (a) shows the total cost of per unit generated power under different values of insulation thickness and mas flow rates with urethane fiberglass as insulation material. The range of total cost lies between 0.30$/KWh to 0.74$/KWh. Figure 49 (b) presents the relevant outlet temperature at 120 days. The maximum outlet temperature can be achieved in the investigation range is 345.6K. The nonlinear optimization problem is solved with the sequential quadratic programming algorithm. For the two insulation materials, the minimum total cost and the relevant optimal parameters for different target temperatures are presented in Table 8. The comparison between the two materials indicates that urethane fiberglass is better than extruded polystyrene from the economic perspective. With urethane fiberglass being used, the minimum cost increases from 0.297$/KWh to 0.429$/KWh for target outlet temperature from 320K to 340K.

Parameter	Value
Operation days each year	120
Load factor	0.9
Effective rate of return	0.08
Project lifetime (years)	20
Energy conversion efficiency	0.75

Table 7-Input parameters for economic analysis

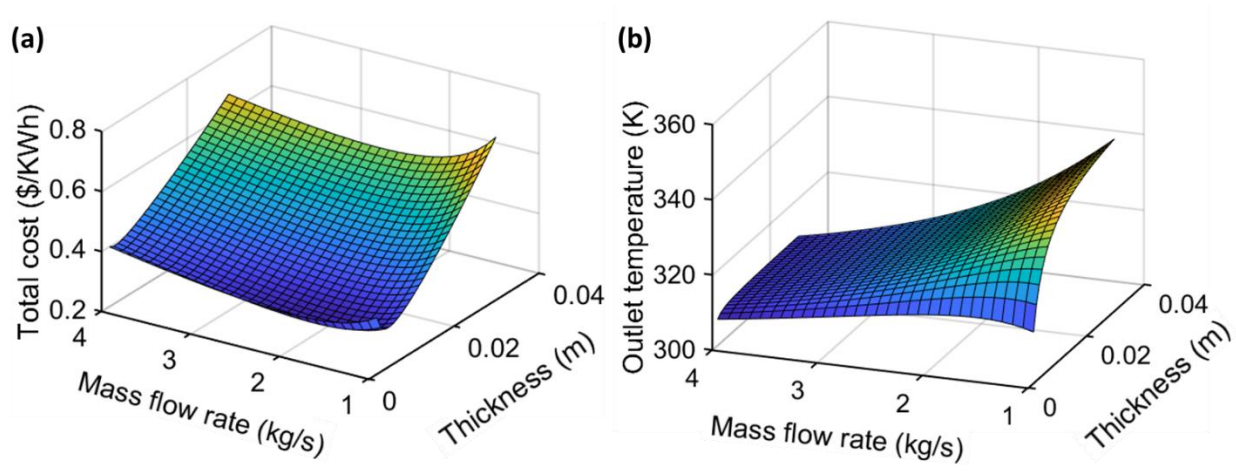

Figure 49-(a) Total cost and (b) outlet temperature at 120days for different mass flow rates and insulation thickness with urethane fiberglass as insulation material

Target outlet temperature (K)	Urethane Fiberglass			Extruded Polystyrene		
	Minimum total cost ($/KWh)	Optimal insulation thickness (m)	Optimal mass flow rate (kg/s)	Minimum total cost ($/KWh)	Optimal insulation thickness (m)	Optimal mass flow rate (kg/s)
320	0.297	0.0043	1.64	0.309	0.0053	1.73
325	0.298	0.0048	1.53	0.314	0.0066	1.52
330	0.314	0.0066	1.28	0.339	0.0091	1.27
335	0.352	0.0090	1.09	0.392	0.0126	1.08
340	0.429	0.0135	1.00	0.497	0.0192	1.00

Table 8-Minimum total costs for different insulation materials at different target outlet temperatures

8. SUMMARY AND CONCLUSIONS

This dissertation presents an approach to study heat transfer during drilling, completion and reservoir development periods. The temperature profile during deepwater drilling circulation, near wellbore formation temperature disturbance by drilling circulation, temperature recovery during clean-up period, fluid nonisothermal behavior in the reservoir, and fluid flow in the wellbore during production are presented.

The specific conclusions for deepwater drilling circulation are:

- Transient temperature behavior happens during the first hour circulation; the wellbore fluid temperature reaches pseudo-steady state after 6 hours of circulation.
- The maximum annulus fluid temperature is at the depth above the bottomhole; the minimum annulus fluid temperature is at the depth between surface and mudline.
- Drilling circulation rate, fluid injecting temperature and geothermal gradient are three important factors affect circulation fluid temperature and near-wellbore formation: lower circulation rate causes higher fluid temperature in formation portion; every 10 ^{o}F increment in injecting fluid temperature raises about 5 ^{o}F fluid temperature in formation portion; higher geothermal gradient increases the fluid temperature difference between drill pipe and annulus.
- During clean-up period, cooled near-wellbore formation is heated up by the warmer reservoir fluid and approaching undisturbed formation temperature in an exponential relationship with reservoir fluid flowing time. The flow rate during clean-up period can be estimated by matching with MDTS measured data.

Simulations and field studies are conducted for nonisothermal fluid flow in the reservoir and coupled with the wellbore heat transfer model, conclusions are presented below:

- The Joule-Thomson (J-T) heating or cooling dominates in the near-wellbore region.
- The J-T effect induces heat in oil reservoirs and also for gas reservoirs when the reservoir pressure exceeds 10,000 psia. However, cooling occurs in gas reservoirs for pressures less than 7,000 psia. Negligible heating or cooling occurs when the reservoir pressure operates within the 7,000 to 10,000 psia range.
- The adiabatic expansion (AE) effect appears less critical than the J-T effect and heat exchange with the over- and under-burden formations. For high-production rates, ignoring the AE effect appears justified. A fully analytical solution including the heat exchange and ignoring the AE effect is available for rapid estimation of the transient temperature.
- The transient sandface temperature estimated from the proposed reservoir heat-transfer model can be coupled with the wellbore heat-transfer model to generate the time-dependent wellbore temperature profiles to assist production monitoring.

In addition, we applied the concept of heat transfer between wellbore and formation to the geothermal recovery from the abandoned oil well. We developed three models, a fully numerical model, a semi-numerical model and a fully analytical model for analyzing. Energy extraction from a 3000 m deep abandoned well was investigated using the three models and the model performances were compared. The major contribution of this study is to demonstrate the feasibility of applying a simple fully analytical model in evaluating the geothermal production from

abandoned wells. This observation is of significant value for the engineering design and optimization of such a geothermal production system. The main conclusions are:

- The assumption of constant heat flow rate in the analytical solution of formation heat conduction is applicable to the geothermal heat production from abandoned wells. Considering the high computational load associated with the numerical model, the analytical treatment of formation heat conduction is recommended.
- The fully analytical model, which assumes steady-state heat transfer and constant fluid properties in wellbore, can accurately estimate the simulation results of the fully numerical model and the semi-numerical model with transient fluid properties. The differences in estimated temperatures are within 1K.
- There exists a maximum outlet temperature for different mass flow rates. The heat extraction rate increases as the mass flow rate increases, but the rate of increase slows down.
- To let the hot water produced from this geothermal energy production system fulfill the purpose of space heating, the heat conductivity of the insulation material should be around 0.05 $Wm^{-1}K^{-1}$, and the thickness of the insulation layer should be around 1cm.
- The proposed fully analytical solution is ideal for engineering design and optimization. The economic analysis with the fully analytical solution indicates that the minimum total cost per unit generated power of the evaluated system lies between 0.3$/KWh and 0.43$/KWh for target outlet temperature from 320K to 340K with urethane fiberglass as insulation material.

REFERENCES

Alimonti, C. and Soldo, E. 2016. Study of geothermal power generation from a very deep oil well with a wellbore heat exchanger. *Renewable energy*, **86**; 292-301.

Alimonti, C. and Soldo, E., et al. 2018.The wellbore heat exchangers: A technical review. *Renewable energy*, **123**: 353-381.

Akhmadullin, I. and Tyagi, M. 2014. Design and analysis of electric power production unit for low enthalpy geothermal reservoir applications. *Int. J. Mech Mechatron Eng*, **1**: 6.

App, J.F. 2009. Field cases: Nonisothermal behavior due to Joule-Thomson and transient fluid expansion/compression effects. Paper SPE-124338-MS presented at the 2009 SPE Annual Technical Conference and Exhibition, New Orleans, Louisiana, 4-7 October..

App, J.F. 2010. Nonisothermal productivity behavior of high-pressure reservoirs. *SPE J*., **15** (1): 50-63.

App, J.F. and Yoshioka, K. 2013. Impact of reservoir permeability on flowing sandface temperatures: dimensionless analysis, *SPE J*., **18** (4): 685-694.

Avdonin, N.A. 1964. Some formulas for calculating the temperature fields of a stratum subject to thermal injection, *Neft'I Gaz*, **7** (3):37-41.

Avdonin, N.A. 1964. On the different methods of calculating the temperature fields of a stratum during thermal injection. *Neft'I Gaz*, **7** (8): 39-44.

Barbier, E. 2002. Geothermal energy technology and current status: an overview. *Renewable and Sustainable Energy Reviews*, **6** (1-2): 3-65.

Bertani, R. 2012. Geothermal power generation in the world 2005-2010 update report. Geothermics, **41**: 1-29.

Bergman, T.L. and Incropera, F.P. 2011. Fundamentals of heat and mass transfer. *John Wiley & Sons*.

Beirute, R.M. 1991. A circulating and shut-in wellbore temperature profile simulator. *Journal of Petroleum Technology*, **43** (09): 1-140.

Bourgoyne, A.T., Chenevert, M.E., Millheim, K.K., and Young, F.F. 1986. Applied drilling engineering. Chp 2: 42-45. Richardson, Texas, *Society of Petroleum Engineers*.

Bu X, Ma W, Li H. 2012. Geothermal energy production utilizing abandoned oil and gas wells. *Renew Energy*, **41**: 80-85.

Cheng W-L, Li T-T, Nian Y-L, Wang C-L. 2013. Studies on geothermal power generation using abandoned oil wells. *Energy*, **59**: 248-254.

Cheng W-L, Li T-T, Nian Y-L, Wang C-L. 2014. Evaluation of working fluids for geothermal power generation from abandoned oil wells. *Applied Energy*, **118** 238-245.

Chevarunotai, N., Hasan, R.R., and Kabir, C.S. 2015. Transient flowing fluid temperature modeling in oil reservoirs for flow associated with large drawdowns. Paper SPE-175008-MS presented at the SPE Annual Technical Conference and Exhibition. Houston, Texas, 28-30 September.

Cui, G. Ren, S. et al. 2017. Geothermal exploitation from hot dry rocks via recycling heat transmission fluid in a horizontal well. *Energy*, **128**: 366-377.

Cei, M. Bertani, R. et al. 2013. Evaluation of heat exchange in a geothermal well. In Proceedings of European Geothermal Congress, Pisa, Italy, 3-7 June, 2013.

Davis, A.P, Michaelides, E.E. 2009. Geothermal power production from abandoned oil wells. *Energy*, **34**: 866-872.

Durrant, J.J., and Thambynayagam, R.K.M. 1986. Wellbore heat transmission and pressure drop for steam/water injection and geothermal production: A simple solution technique. *SPE Reservoir Engineering*, **1** (2): 148-162.

Dranchuk, P.M. and Abou-Kassem, H. 1975. Calculation of Z factors for natural gases using equations of state. *Journal of Canadian Petroleum Technology*, **14** (3): 34.

Duru, O.O. and Horne, R.N. 2010. Modeling reservoir temperature transients and reservoir-parameter estimation constrained to the model. *SPE Reservoir & Engineering*, **13** (6): 873-883.

Edwardson, M.J., et al. 1962. Calculation of formation temperature distributions caused by mud circulation, *JPT*, **14** (04): 416-426.

Feng, J., Fu, J., Chen, P. et al. 2016. Experimental study and molecular simulation of gas dissolution and diffusion behavior in drilling fluid. *JNGSE*, **36**: 424-433.

Feng, Y. and Tyagi, M. 2015. A downhole heat exchanger for horizontal wells in low-enthalpy geopressured geothermal brine reservoirs. *Geothermics*, **5**: 368-378.

Gallup, D.L. 2009. Production engineering in geothermal technology: a review. *Geothermics*, **38**: 326-334.

Galoppi, G. et al. 2015. Feasibility study of a geothermal power plant with a double-pipe heat exchanger. *Energy Procedia*, **81**: 193-204.

Gao, Y.H., Sun, B.J., Xu, B. et al. 2017. A wellbore/formation-coupled heat-transfer model in deepwater drilling and its application in prediction of hydrate-reservoir dissociation, *SPE J.*, **22** (03): 756-766.

Gupta, H.K. and Roy, S. 2006. Geothermal energy: an alternative resource for the 21st century. *Elsevier*.

Guo, X. Song, H. Killough,J. et al. 2018. Numerical investigation of the efficiency of emission reduction and heat extraction in a sedimentary geothermal reservoir: a case study of the daming geothermal field in China. *Environ. Sci. and Pollu. Res.* **25** (5): 4690-4706.

Hagoort, J. 2004. Ramey's wellbore heat transmission revisited. *SPE J*., **9** (04): 465-474.

Hasan, A.R., and Kabir, C.S., 1994. Aspects of wellbore heat transfer during two-phase flow. *SPE Production & Facilities,* **9** (03): 211-216.

Hasan, A.R., and Kabir, C.S., 2018. Fluid flow and heat transfer in wellbores. 2nd edition. Richardson, Texas, *Society of Petroleum Engineers*.

Hasan, A.R., and Kabir, C.S., Ameen, M.M. et al. 1996. A mechanistic model for circulating fluid temperature. *SPE J*., **1**: 133-144.

Hashmi, G.G., Kabir, C.S. and Hasan, A.R. 2015. Estimating reliable gas rate with transient temperature modeling for interpreting early-time cleanup data during transient testing. *JPSE,* **133**: 285-295.

Holmes, C.S. and Swift, S.C. 1970. Calculation of circulating mud temperatures. *J. of Petroleum Technology,* **22** (06): 670-674.

Horne, R.N. and Shinohara K. 1979. Wellbore heat loss in production and injection wells. *J. of Petroleum Technology*, **31** (01): 116-118.

Horne, R.N. 2007. Listening to the reservoir-interpreting data from permanent downhole gauges. *J. of Petroleum Technology*, **59** (12): 78-86.

Huenges, E. and Ledru, P. 2011. Geothermal energy systems: exploration, development, and utilization, *John Wiley & Sons*.

Keller, H.H., Couch E.J. and Berry, P.M. 1974. Temperature distribution in circulating mud columns, *SPE J.*, **13** (01): 23-30.

Konopczynski, M.R., Moore, W.R. and Hailstone, J.J. 2002. ESPs and intelligent completions. Paper SPE-77656-MS presented at SPE Annual Technical Conference and Exhibition, San Antonio, Texas, 29 Sep-2 Oct.

Kuhl, T., Brenni, R. and Eugster, W. 2002. System performance of a deep borehole heat exchanger, *Geothermics*, **31** (6): 687-708.

Kutasov, I.M. 1989. Application of the horner method for a well produced at a constant bottomhole pressure. *SPE Formation Evaluation*, **4** (01): 90-92.

Kujawa, T., Nowak, W. and Stachel, A.A. 2006. Utilization of existing deep geological wells for acquisitions of geothermal energy. *Energy*, **31**: 650-664

Lauwerier, H.A. 1995. The transport of heat in an oil layer caused by the injection of hot fluid. *Applied Scientific Research, Section A*, **5** (203): 145-150.

Li, B., et al. 2017. A new numerical solution to predict the temperature profile of gas-hydrate-well drilling. *SPE J.*, **22** (04).

Li, Z., et al. 2011. Using downhole temperature measurement to assist reservoir characterization and optimization, *JPSE*, **78**: 454-463.

Le Lous, M. AND Larroque, F. et al. 2015. Thermal performance of a deep borehole heat exchanger: insights from a synthetic coupled heat and flow model. *Geothermics*, **57**: 157-172.

Mahlia, T.M., Taufiq, B.N., Masjuki, H.H., et al. 2007. Correlation between thermal conductivity and thickness of selected insulation materials for building wall. *Energy and Buildings*, **39** (2): 182-187.

Mao, Y. and Zeidouni, M. 2017. Analytical solutions for temperature transient analysis and near wellbore damage zone characterization. Paper SPE-185990-MS presented at the SPE Reservoir Characterization & Simulation Conference, Abu Dhabi, UAE, 08-10 May.

Maruyama, K., Tsura, E et al. 1990. An experimental study of casing performance under thermal cycling conditions, *SPE Drilling Engineering*, **5** (02):156-164.

Muradov, K. and Davies, D. 2012. Early-time asymptotic, analytical temperature solution for linear non-adiabatic flow of a slightly compressible fluid in a porous layer. *Transport in Porous Media*, **91** (3): 791-811.

Muradov, K. and Davies, D. 2012. Temperature transient analysis in horizonal wells: application workflow, problems and advantages. *JPSE*, **92**: 11-23.

Nalla, G., Shook, G.G. et al. 2005. Parametric sensitivity study of operating and design variables in wellbore heat exchangers. *Geothermics*, **34** (3): 330-346.

Nian, Y-L and Cheng, W-L. 2018. Evaluation of geothermal heating from abandoned oil wells. *Energy*, **142**: 592-607.

Noorollahi, Y. Pourarshad M. et al. 2015. Numerical simulation of power production from abandoned oil wells in Ahwaz oil field in southern Iran. *Geothermics*, **55**: 16-23.

Onur, M. and Cinar, M. 2017. Analysis of sandface temperature transient data for slightly compressible, single-phase reservoirs. *SPE J*., **22** (4): 1134-1155.

Onur, M. and Palabiyik, Y. 2015. Nonlinear parameter estimation based on history matching of temperature measurements for single-phase liquid-water geothermal reservoirs. *In Proceedings, World Geothermal Congress in Melbourne*, Australia, 19-25, April.

Oster, C.A., and Scheffler, W.A. 1876. Well hole temperature distribution in the presence of aquifers. Paper presented at Joint Petroleum Mechanical Engineering and Pressure Vessels and Piping Conference, Mexico City, Mexico, 19-24 September.

Imomoh, E. 2013. Innovation: The intelligence behind intelligent completion. *JPT*, **65** (04).

Raymond, L.R. 1969. Temperature distribution in a circulating drilling fluid, *JPT*, **21** (03): 333-341.

Rubinshtein, L.I. 1959. The total heat losses in injection of a hot fluid into a stratum. *Neft'I Gaz*, **2** (9): 41.

Ramazanov, A. Valiullin, R.A. et al. 2010. Thermal modeling for characterization of near wellbore zone and zone allocation. Paper SPE-136256-ru presented at the SPE Russian Oil and Gas Conference and Exhibition, Moscow, Russia, 26-28 Oct.

Riberiro, P.M. and Horne, R.N. 2016. Detecting fracture growth out of zone by use of temperature analysis, *SPE J*, **21** (04): 1-263.

Robinson, M. 2003. Intelligent well completions, *JPT*, **55** (08): 57-59.

Sayigh, A. 1999. Renewable energy-the way forward. *Applied Energy*, **64**: 15-30.

Spillette, A.G. 1965. Heat transfer during hot fluid injection into an oil reservoir. *J. of Canadian Petroleum Technology*, 4(04): 213-218.

Satman, A., Brigham, W.E., Zolotukhin, A.b. 1979. A new approach for predicting the thermal behavior in porous media during fluid injection. *Geothermal Resour. Council Trans.*, **3**: 623-624.

Schoeppel, R.J., and Bennett, R.E. 1971. Numerical simulation of borehole and formation temperature distributions while drilling to total depth. In Fall Meeting of the Society of Petroleum Engineers of AIME. New Orleans, Louisiana, 3 October.

Sliwa, A.S., Rosen, M.A. and et al. 2015. Deep borehole heat exchangers – a conceptual review. In Proceedings World Geothermal Congress, Melbourne, Australia, 19-25 April.

Schetz, J.A. and Fuhs, A.E. 1999. Fundamentals of fluid mechanics. *John Wiley & Sons*.

Tardy, P.M.J, Ramondenc, P., et al. 2012. Inversion of distributed temperature sensing logs to measure zonal coverage during and after wellbore treatments with coiled tubing. *SPEPO*, **27** (1): 78-86.

Taleghani, A.D. 2013. An improved closed-loop heat extraction method for geothermal resources, *J. of Energy Resources Technology*, **135** (4): 042904.

Templeton, J.D., et al. 2014. Abandoned petroleum wells as sustainable sources of geothermal energy. *Energy*, **70**: 366-373.

Thomas, D.C., Lea Jr, J.R., and Turek, E.A. 1984. Gas solubility in oil-based drilling fluids: effects on kick detection. *JPT*, **36** (06): 959-968.

U.S. Energy Information Administration. 2016. Offshore production nearly 30% of global crude oil output in 2015. https://www.eia.gov/todayinenergy/detail.php?id=28492.

Wang, Z., McClure, M.W., and Horne, R.N. 2009. A single-well EGS configuration using a thermosiphon. In Proceedings of Thirty-fourth Workshop on Geothermal Reservoir Engineering Sandford University, Stanford, California, 1-11 February.

Wooley, G.R. 1980. Computing downhole temperatures in circulation, injection, and production wells. *JPT*, **32** (09): 1-509.

Wong, R.C.K, and Yeung, K.C. 2006. Structural integrity of casing and cement annulus in thermal well under steam stimulation. *J. of Canadian Petroleum Technology*, **45** (12): 6-9.

Wu, X., Xu, B and Ling, K. 2015. A semi-analytical solution to the transient temperature behavior along the vertical wellbore. *JPSE*, **131**: 122-130.

Xu, B., Kabir, S., and Hasan, A.R. 2018. Modeling coupled nonisothermal reservoir/wellbore flow behavior in gas reservoir systems. Paper SPE=190067-MS presented at the 2018 SPE Western Regional Meeting, Garden Grove, California, USA, 22-6 April.

Yang, Y., Huo, Y. et al. 2017. Construction and preliminary test of a geothermal ORC system using geothermal resource from abandoned oil wells in the Huabei oilfield of China. *Energy*, **140**: 633-645.

Zayed, S., et al. 2017. Zohr field: enhanced characterization of productive intervals by means of an innovative temperature monitoring application during well testing. Presented at the 2017 Offshore Mediterranean Conference and Exhibition, Ravenna, Italy, 29-31 Match.

Zhang, S. and Zhu, D. 2017. Inversion of downhole temperature measurements in multistage fracture stimulation in horizontal wells. SPE Annual Technical Conference and Exhibition, San Antonio, Texas, USA, 9-11 October.

Zhu, D., Hill, D., and Zhang, S. 2018. Using temperature measurements from production logging/downhole sensors to diagnose multistage fractured well flow profile. SPWLA 59TH Annual Logging Symposium, London, UK, 2-6 June.

APPENDIX A

Offshore deepwater drilling circulation model

Transient heat transfer in the formation

During drilling circulation, the wellbore is acting as a heat sink. An energy balance of the formation in a cylindrical system can be expressed as:

$$\frac{\partial^2 T}{\partial r^2} + \frac{1}{r}\frac{\partial T}{\partial r} = \frac{c_{pe}\rho_e}{K_e}\frac{\partial T}{\partial t} \tag{A-1}$$

The initial and boundary conditions are:

$$T(t = 0, r) = T_{ei} \tag{A-2}$$

$$T(t, r = \infty) = T_{ei} \tag{A-3}$$

$$\frac{\partial T}{\partial r}(r = r_{wb}) = \frac{2\pi K_e}{r} Q \tag{A-4}$$

Define dimensionless temperature T_D to connect the formation and wellbore:

$$T_D = -\frac{2\pi K_e}{Q}(T_{wb} - T_{ei}) \tag{A-5}$$

Hasan and Kabir (1994) gave an approximate solution to the constant rate solution at the wellbore:

$$T_D = \ln[e^{-0.2t_D} + (1.5 - 0.3719e^{-t_D})\sqrt{t_D}] \tag{A-6}$$

Where T_{wb} is the wellbore formation interface temperature and t_D is the dimensionless time, defined as $K_e t/(\rho_e c_{pe} r_{wb}^2)$.

Steady-state heat transfer in the wellbore

Drilling fluid is flowing down the drill pipe and flowing back in the annulus. Define z is positive in the downward direction. In the drill pipe, the heat enters the element by convection

$Q_{dp}(z)$ at depth z and heat flow from annulus to the drill pipe by Q_{ta}; heat leaves the element by convection $Q_{dp}(z+dz)$ at depth $z+dz$, mathematically expressed as:

$$Q_{dp}(z) - Q_{dp}(z+dz) = -Q_{ta} \tag{A-7}$$

or

$$c_{pm}[T_{dp}(z) - T_{dp}(z+dz)] = -Q_{ta}$$

In the annulus, the heat enters the element by convection $Q_a(z+dz)$ and heat flows from formation to annulus by conduction Q_F; heat leaves annulus by convection $Q_a(z)$, and heat flow from annulus to the drill pipe by Q_{ta}, mathematically expressed as:

$$Q_a(z+dz) - Q_a(z) = Q_{ta} - Q_F \tag{A-8}$$

or

$$c_{pm}[T_a(z+dz) - T_a(dz)] = Q_{ta} - Q_F$$

The transient heat transfer from the formation to the wellbore is rewritten from Eq. A-5:

$$Q_F = \frac{2\pi K_e}{T_D}(T_{ei} - T_{wb}) \tag{A-9}$$

The wellbore formation interface temperature is related to the annular fluid temperature by the annulus overall heat transfer coefficient for annulus, U_a:

$$Q = 2\pi r_c U_a (T_{wb} - T_a) \tag{A-10}$$

Due to the fact that the heat transfer in the radial direction is same, equaling Eq. A-9 and Eq. A-10, we could obtain:

$$Q_F = c_{pm} L_R (T_{ei} - T_a) \tag{A-11}$$

Where

$$L_R = \frac{2\pi}{c_{pm} w}\left[\frac{r_{co} U_a K_e}{K_e + r_{co} U_a T_D}\right] \tag{A-12}$$

Similarly, heat transferred from the annular fluid to the fluid in the drill pipe is:

$$Q_{ta} = \frac{c_{pm}}{B}\left(T_a - T_{dp}\right) \tag{A-13}$$

Where

$$B = \frac{wc_{pm}}{2\pi r_{dpo} U_{dp}} \tag{A-14}$$

U_{dp} in Eq. A-14 is the heat transfer coefficient for drill pipe. The calculations of U_a and U_{dp} are presented in Hasan and Kabir (2018). Plugging Eq. A-11 and A-13 into Eq. A-8 and rearranging,

$$\frac{1}{L_R}\frac{dT_a}{dz} = T_a - T_{ei} + \left(T_a - T_{dp}\right)\frac{1}{L_R B} \tag{A-15}$$

Plugging Eq. A-13 into Eq. A-7 and rearranging:

$$\frac{dT_{dp}}{dz} = \frac{T_a - T_{dp}}{B} \tag{A-16}$$

Combing Eq. A-15 and Eq. A-16, the following second order linear partial differential equation is obtained:

$$\frac{B}{L_R}\frac{d^2T_{dp}}{dz^2} - B\frac{dT_{dp}}{dz} - T_{dp} + T_s + g_G z = 0 \tag{A-17}$$

Analytical solutions of the PDE

The governing equation for circulating fluid temperature is given by Eq. A-17. A direct solution of Eq. A-17 for deepwater drilling circulation system is complicated by the fact that the seawater has a very different thermal gradient than the formation. To overcome this problem, the deepwater circulation system is separated into two portions: seawater portion and formation portion. The governing equation under different boundary conditions are solved separately.

Seawater portion

Eq. A-17 is first solved for the seawater section by rewriting it as follows:

$$\frac{B_s}{L_{R,s}}\frac{d^2T_{dp}}{dz^2} - B_s\frac{dT_{dp}}{dz} - T_{dp} + T_{s,s} + g_{G,s}z = 0 \tag{A-18}$$

In the followings, additional subscript *s* is used to denote seawater portion. Using the method of characteristic, Eq. A-18 could be solved as:

$$T_{dp} = \alpha_s e^{\lambda_{1,s}z} + \beta_s e^{\lambda_{2,s}z} + g_{G,s}z - B_s g_{G,s} + T_{s,s} \tag{A-19}$$

Relating annulus and fluid temperature through the heat transfer between them:

$$T_a = T_{dp} + B\frac{dT_{dp}}{dz} \tag{A-20}$$

Hence,

$$T_a = \left(1 + \lambda_{1,s}B_s\right)\alpha_s e^{\lambda_{1,s}z} + (1 + \lambda_{2,s}B_s)\beta_s e^{\lambda_{2,s}z} + g_{G,s}z + T_{s,s} \tag{A-21}$$

$\lambda_{1,s}$ and $\lambda_{2,s}$ are the characteristic roots, defined as:

$$\lambda_{1,s} = \frac{L_{R,s}}{2} + \frac{L_{R,s}\sqrt{1 + \frac{4}{L_{R,s}B_s}}}{2} \tag{A-22}$$

$$\lambda_{2,s} = \frac{L_{R,s}}{2} - \frac{L_{R,s}\sqrt{1 + \frac{4}{L_{R,s}B_s}}}{2} \tag{A-23}$$

The constants α_s and β_s are obtained from boundary conditions. Drill pipe fluid temperature at wellhead is known and drill pipe fluid temperature at the mudline (denoted by subscript *ml*) is an unknown constant:

$$T_{dp}(z = 0) = T_{inj} \tag{A-24}$$

$$T_{dp}(z = L_w) = T_{dpml} \tag{A-25}$$

Solving Eq. A-24 and Eq. A-25 simultaneously, one obtainsα_s and β_s:,

$$\alpha_s = -\frac{\left(T_{inj} - T_{s,s} + B_s g_{G,s}\right)e^{\lambda_{2,s}L_w} + (T_{s,s} + g_{G,s}L_w - T_{dpml} - g_{G,s}B_s)}{e^{\lambda_{1,s}L_w} - e^{\lambda_{2,s}L_w}} \tag{A-26}$$

$$\beta_s = \frac{\left(T_{inj} - T_{s,s} + B_s g_{G,s}\right)e^{\lambda_{1,s}L_w} + \left(T_{s,s} + g_{G,s}L_w - T_{dpml} - g_{G,s}B_s\right)}{e^{\lambda_{1,s}L_w} - e^{\lambda_{2,s}L_w}} \qquad \text{(A-27)}$$

Formation portion

In the formation portion, the governing equation is same where additional subscript *e* indicates formation parameters:

$$\frac{B_e}{L_{R,e}}\frac{d^2T_{dp}}{dz^2} - B_e\frac{dT_{dp}}{dz} - T_{dp} + T_{s,e} + g_{G,e}z = 0 \qquad \text{(A-28)}$$

The fluid temperature at the mudline T_{dpml} is unknown in the seawater portion. However, the fluid temperature in the drilling pipe and annulus are continuous. In other words, the drill pipe/annulus fluid temperatures at the mudline are same in both the seawater portion and the formation portion. Eq. A-28 has a solution similar to Eq. A-19:

$$T_{dp} = \alpha_e e^{\lambda_{1,e}(z-L_w)} + \beta_e e^{\lambda_{2,e}(z-L_w)} + g_{G,e}(z - L_w) - B_e g_{G,e} + T_{s,e} \qquad \text{(A-29)}$$

The expressions for characteristic roots are same as the seawater portion, except that it uses the formation thermal properties. The constants α_e and β_e are obtained from boundary condition of formation portion. In the formation, the drill pipe fluid temperature at the bottomhole is equal to the annulus fluid temperature, or the derivative of drill pipe fluid temperature is equal to zero. Mathematically expressed as:

$$T_{dp}(z = L_w) = T_{dpml} \qquad \text{(A-30)}$$

$$\frac{dT_{dp}}{dz}(z = z_L) = 0 \qquad \text{(A-31)}$$

z_L is wellbore total depth, which includes the seawater depth. Solve Eq. A-30 and Eq. A-31 to obtain α_e and β_e:

$$\alpha_e = -\frac{\left(T_{dpml} - T_{s,e} + B_e g_{G,e}\right)\lambda_{2,e} e^{\lambda_{2,e}(z_L - L_w)} + g_{G,e}}{\lambda_{1,e} e^{\lambda_{1,e}(z_L - L_W)} - \lambda_{2,e} e^{\lambda_{2,e}(z_L - L_w)}} \tag{A-32}$$

$$\beta_e = \frac{\left(T_{dpml} - T_{s,e} + B_e g_{G,e}\right)\lambda_{1,e} e^{\lambda_{1,e}(z_L - L_w)} + g_{G,e}}{\lambda_{1,e} e^{\lambda_{1,e}(z_L - L_w)} - \lambda_{2,e} e^{\lambda_{2,e}(z_L - L_w)}} \tag{A-33}$$

Computational Approach

The computation is initiated with an assumed value for the drill pipe fluid temperature at the mudline, T_{dpml}. Since the temperatures are continuous: T_{dpml} is same on both sides of the mudline. This allows calculation of drill pipe and annulus fluid temperatures in the seawater and the formation portions using Eq. A-19, Eq. A-21 and Eq. A-29. However, if the assumed T_{dpml} value is off, the computed mudline annulus fluid temperature, T_{aml}, would not be continuous at the mudline. Trial and error method could be used until estimations by the two methods agrees within a given tolerance, 1×10^{-3} °F. An alternative approach is to solve the T_{dpml} by equaling Eq. A-19 and Eq. A-29. A complicated but rigorous analytical expression for T_{dpml} is shown in Eq. A-34:

$$T_{dpml} = \frac{a_s C_1 C_5 C_7 - b_s C_2 C_5 C_7 - a_f C_3 C_4 C_7 + b_f C_3 C_5 C_6 - C_3 C_5 C_7 C_8}{a_s C_5 C_7 - b_s C_5 C_7 + a_f C_3 C_7 - b_f C_3 C_5} \tag{A-34}$$

Where

$$a_s = (1 + \lambda_{1,s} B_s) e^{\lambda_{1,s} L_w} \tag{A-35}$$

$$b_s = (1 + \lambda_{2,s} B_s) e^{\lambda_{2,s} L_w} \tag{A-36}$$

$$a_e = 1 + \lambda_{1,e} B_e \tag{A-37}$$

$$b_e = 1 + \lambda_{2,e} B_e \tag{A-38}$$

$$C_1 = \left(T_{inj} - T_{s,s} + B_s g_{G,s}\right)\lambda_{2,s} e^{\lambda_{2,s} L_w} + (T_{s,s} + g_{G,s} L_w - g_{G,s} B_s) \tag{A-39}$$

$$C_2 = \left(T_{inj} - T_{s,s} + B_s g_{G,s}\right)\lambda_{1,s} e^{\lambda_{1,s} L_w} + \left(T_{s,s} + g_{G,s} L_w - g_{G,s} B_s\right) \quad \text{(A-40)}$$

$$C_3 = e^{\lambda_{1,s} L_w} - e^{\lambda_{2,s} L_w} \quad \text{(A-41)}$$

$$C_4 = \frac{g_{G,e}}{\lambda_{2,e} e^{\lambda_{2,e}(z_L - L_w)}} - T_{s,e} + B_e\, g_{G,e} \quad \text{(A-42)}$$

$$C_5 = \frac{\lambda_{1,e} e^{\lambda_{1,e}(z_L - L_w)}}{\lambda_{2,e} e^{\lambda_{2,e}(z_L - L_w)}} - 1 \quad \text{(A-43)}$$

$$C_6 = \frac{g_{G,e}}{\lambda_{1,e} e^{\lambda_{1,e}(z_L - L_w)}} - T_{s,e} + B_e\, g_{G,e} \quad \text{(A-44)}$$

$$C_7 = 1 - \frac{\lambda_{2,e} e^{\lambda_{2,e}(z_L - L_w)}}{\lambda_{1,e} e^{\lambda_{1,e}(z_L - L_w)}} \quad \text{(A-45)}$$

$$C_8 = g_{G,s} L_w + T_{s,s} - T_{s,e} \quad \text{(A-46)}$$

APPENDIX B

Semianalytical solution of heat transfer in the reservoir

The general energy balance equation for the reservoir system is:

$$\left[\phi s_f \rho_f c_{pf} + \phi s_w \rho_w c_{pw} + (1-\phi)\rho_e c_{pe}\right]\frac{\partial T}{\partial t} + \rho_f u_r c_{pf}\frac{\partial T}{\partial r} + \rho_f u_r \sigma_f \frac{\partial P}{\partial r} +$$

$$\left(\phi s_f \rho_f \sigma_f + \phi s_w \rho_w \sigma_w - 1\right)\frac{\partial P}{\partial t} = \frac{1}{r}\frac{\partial}{\partial r}\left(\lambda r \frac{\partial T}{\partial r}\right) + \dot{Q} \qquad \text{(B-1)}$$

The initial conditions are $T(r, t=0) = T_{ei}$ and $p\,(r, t=0) = P_i$; the boundary conditions are $T(r = r_e, t) = T_{ei}$ and $P(r = r_e, t) = P_i$.

The heat conduction term is neglected and heat transfer to surrounding formation $\dot{H}$ is written as:

$$\dot{H} = -\frac{2h_c}{h}(T - T_s) \qquad \text{(B-2)}$$

where h_c is the heat transfer coefficient of the reservoir, h is the thickness of the reservoir and T_s is the surrounding formation temperature. It reasonable to assume $T_s \approx T_{ei}$. The fluid velocity u_r in term of low rate is $\frac{q}{2\pi r h}$ and $\frac{\partial P}{\partial r}$ in term of flow rate is $-\frac{qu}{2\pi r h k} \cdot \frac{\partial \mathrm{P}}{\partial \mathrm{t}}$ and can be written as $-\frac{q\mu B}{4\pi k h t}\exp\left(-\frac{r^2}{4\eta t}\right)$, η is the formation diffusivity. Taking all these terms into Eq. B-1 and upon simplification, we have

$$Ar^2\frac{\partial T}{\partial t} - Br\frac{\partial T}{\partial r} - C - F\frac{r^2}{t}\exp\left(-\frac{r^2}{4\eta t}\right) = -Dr^2T + Er^2 \qquad \text{(B-3)}$$

where

$$A = \left[\phi s_f \rho_f c_{pf} + \phi s_w \rho_w c_{pw} + (1-\phi)\rho_e c_{pe}\right]\left(\frac{2\pi h}{q}\right) \tag{B-4}$$

$$B = \rho_f c_{pf} \tag{B-5}$$

$$C = \frac{q\rho_f \sigma_f \mu_f}{2\pi hk} \tag{B-6}$$

$$D = \frac{4h_c\pi}{q} \tag{B-7}$$

$$E = \frac{4h_c\pi}{q} T_{ei} \tag{B-8}$$

$$F = \frac{\left(\phi s_f \rho_f \sigma_f + \phi s_w \rho_w \sigma_w - 1\right)\mu_f}{2k} \tag{B-9}$$

The third term on the left side of Eq. B-3 containing the parameter *C* includes fluid convection (through rate, *q*) and J-T heating (through σ). σ_f is the fluid throttling coefficient and it is related to J-T coefficient by the following relationship:

$$\sigma_f = -C_{JT} c_{pf} \tag{B-10}$$

To solve Eq. B-3, it is necessary to transfer it into Laplace Domain as:

$$Ar^2 s\bar{T} - Ar^2 T_i - Br\frac{\partial \bar{T}}{\partial r} - \frac{C}{s} - 2Fr^2 K_o\left(\sqrt{\frac{r^2 s}{\eta}}\right) = -Dr^2\bar{T} + \frac{Er^2}{s} \tag{B-11}$$

K_o is the modified Bessel function of second kind with zero-order. Rearranging Eq. B-11, we have

$$\frac{\partial \bar{T}}{\partial r} - \frac{AS+D}{B} r\bar{T} = -\frac{Er^2 + Ar^2 T_i s + 2Fr^2 K_o\left(\sqrt{\frac{r^2 s}{\eta}}\right)s + C}{Brs} \qquad \text{(B-12)}$$

Multiplying the integration factor $\exp(-\frac{AS+D}{2B}r^2)$ on both side of Eq. B-12 and solving for $\bar{T}$:

$$\bar{T}(r,s) = \frac{T_i}{s}\exp\left[-\frac{As+D}{2B}(r_e^2 - r^2)\right] + \exp\left[\frac{AS+D}{2B}r^2\right]\int_r^{r_e} \mathrm{M(x,s)}dx \qquad \text{(B-13)}$$

where

$$M(x,s) = \exp\left[-\frac{As+D}{2B}x^2\right]\left[\frac{Ex^2 + Ax^2 T_i s + 2Fx^2 K_o\left(\sqrt{\frac{x^2 s}{\eta}}\right)s + C}{Bxs}\right] \qquad \text{(B-14)}$$

Eq. B-13 is the final solution of the general energy-balance equation. Thereafter, we used the Gaver-Stehfest algorithm to numerically convert Eq. B-13 to the real-time domain. If the adiabatic expansion term (defined by parameter *F* in Eq. B-9) is ignored, the results obtained by the semianalytical solution (Eq. B-12) will be same as the fully analytical solution shown in Eq. 14.

APPENDIX C

Analytical solution of heat transfer in the reservoir

If the adiabatic expansion term is ignored, Eq. B-3 can be simplified as:

$$Ar^2\frac{\partial T}{\partial t} - Br\frac{\partial T}{\partial r} - C = -Dr^2T + Er^2 \tag{C-1}$$

Rearrange Eq. C-1, it can be written as:

$$\frac{\partial T}{\partial t} - \frac{B}{Ar}\frac{\partial T}{\partial r} = -\frac{D}{A}T + \frac{E}{A} + \frac{C}{Ar^2} \tag{C-2}$$

Using the method of characteristic, Eq. C-2 is written as:

$$\frac{\partial T}{\partial t} + \frac{D}{A}T = \frac{E}{A} + \frac{C}{Ar^2} \tag{C-3}$$

Along the characteristic curve:

$$\frac{\partial r}{\partial t} = -\frac{B}{Ar} \tag{C-4}$$

Integrate both sides of Eq. C-4 to get a relationship between *r* and *t*:

$$r^2 = -\frac{2B}{A}t + \varepsilon_1 \tag{C-5}$$

Plugging Eq. C-5 into Eq. C-3:

$$\frac{\partial T}{\partial t} + \frac{D}{A}T = +\frac{E}{A} + \frac{C}{A\varepsilon_1 - 2Bt} \tag{C-6}$$

Eq. C-6 is a first order ODE can be solved. Define $\mathrm{H} = \mathrm{D}/\mathrm{A}$ and $\mu = \mathrm{e}^{Ht}$. Multiplying μ on both side of Eq. C-6, we could obtain:

$$\frac{\partial(T \cdot \mathrm{e}^{Ht})}{\partial t} = (\mathrm{e}^{Ht})\frac{E}{A} + (\mathrm{e}^{Ht})\frac{C}{A\varepsilon_1 - 2Bt} \tag{C-7}$$

Rearranging and integrating both sides of Eq. C-7 with respect to time, solve for *T*:

$$\mathrm{e}^{Ht} \cdot T = \mathrm{e}^{Ht} \cdot \frac{E}{AH} - \frac{C}{2B} e^{\frac{AH\varepsilon_1}{2B}} E_i\left[-\frac{H(A\varepsilon_1 - 2Bt)}{2B}\right] + g'(\varepsilon_1) \tag{C-8}$$

Where $g'(\varepsilon_1)$ is a function of ε_1 .Next, applying the initial condition to evaluate $g'(\varepsilon_1)$: $\mathrm{T(r, t = 0) = T_{ei}}$. Taking into Eq. C-8:

$$g'(\varepsilon_1) = T_{ei} - \frac{E}{AH} + \frac{C}{2B} e^{\frac{AH\varepsilon_1}{2B}} E_i\left[-\frac{AHr^2}{2B}\right] \tag{C-9}$$

Plugging Eq. C-9 into Eq. C-8:

$$\begin{aligned}\mathrm{e}^{Ht} \cdot T = \mathrm{e}^{Ht} \cdot \frac{E}{AH} - \frac{C}{2B} e^{\frac{AH\varepsilon_1}{2B}} E_i\left[-\frac{H(A\varepsilon_1 - 2Bt)}{2B}\right] + T_{ei} - \frac{E}{AH} \\ + \frac{C}{2B} e^{\frac{AH\varepsilon_1}{2B}} E_i\left[-\frac{AHr^2}{2B}\right]\end{aligned} \tag{C-10}$$

Recall Eq. C-5:

$$\varepsilon_1 = r^2 + \frac{2B}{A}t \tag{C-11}$$

Taking Eq. C-11 into Eq. C-10 and rearrange:

$$\begin{aligned}T = -\frac{C}{2B} e^{\frac{AHr^2}{2B}} E_i\left[-\frac{AHr^2}{2B}\right] + \frac{C}{2B} e^{\frac{AHr^2}{2B}} E_i\left[-\frac{H(Ar^2 + 2Bt)}{2B}\right] + T_{ei} e^{-Ht} \\ + \frac{E}{AH} - \frac{E}{AH} e^{-Ht}\end{aligned} \tag{C-12}$$

Recall previous parameter definition $\mathrm{E/D} = \mathrm{T_{ei}}$ and $\mathrm{H} = D/A$ to further simplify Eq. C-12, the final analytical solution is:

$$T = T_{ei} + \frac{C}{2B} e^{\frac{Dr^2}{2B}} Ei\left[-\frac{D(Ar^2 + 2Bt)}{2AB}\right] - \frac{C}{2B}\, e^{\frac{Dr^2}{2B}} Ei\left[-\frac{Dr^2}{2B}\right] \qquad \text{(C-13)}$$

APPENDIX D

PVT relationship for the J-T coefficient

For a liquid undergoing no phase, the enthalpy is a function of pressure and temperature and is given as:

$$\mathrm{d}H = \left(\frac{\partial H}{\partial T}\right)_P \mathrm{d}T + \left(\frac{\partial H}{\partial P}\right)_T \mathrm{d}p = c_p \mathrm{d}T - c_p C_{JT} \mathrm{d}p \qquad \text{(D-1)}$$

Where C_{JT} represents the Joule-Thomson coefficient and c_p is the heat capacity of the fluid at constant pressure. We use symbol V for specific volume, which is the inverse of density ρ. From Maxwell equations:

$$\left(\frac{\partial H}{\partial P}\right)_T = V + T\left(\frac{\partial S}{\partial P}\right)_T \text{ and } \left(\frac{\partial S}{\partial P}\right)_{\boldsymbol{T}} = -\left(\frac{\partial V}{\partial T}\right)_{\boldsymbol{p}}$$

$$\mathrm{d}H = c_p \mathrm{d}T - \left[V - T\left(\frac{\partial V}{\partial T}\right)_p\right] \mathrm{d}p \qquad \text{(D-2)}$$

Comparing Eq. D-1 and Eq. D-2:

$$c_p C_{JT} = -\left[V - T\left(\frac{\partial V}{\partial T}\right)_p\right] \qquad \text{(D-3)}$$

For liquids, using volume expansion coefficient, $\beta = \left(\frac{1}{V}\right)\left(\frac{\partial V}{\partial T}\right)_p = -\left(\frac{1}{\rho}\right)\left(\frac{\partial \rho}{\partial T}\right)_p$, we write:

$$c_p C_{JT} = -V(1 - T\beta) \qquad \text{(D-4)}$$

For constant enthalpy process, $dT = C_{JT}\mathrm{d}p$. V increases with T, so β is positive but small. $1 - T\beta$ is usually positive for liquids and making C_{JT} negative for liquids. For real gases, according the equation of state:

$$V = \frac{ZRT}{p} \tag{D-5}$$

$$\left(\frac{\partial V}{\partial T}\right)_p = \left(\frac{ZR}{p}\right) + \left(\frac{RT}{p}\right)\left(\frac{\partial Z}{\partial T}\right)_p = \left(\frac{V}{T}\right) + \left(\frac{V}{Z}\right)\left(\frac{\partial Z}{\partial T}\right)_p \tag{D-6}$$

Hence,

$$c_p C_{JT} = -\left[V - V - \left(\frac{VT}{Z}\right)\left(\frac{\partial Z}{\partial T}\right)_p\right] = \left(\frac{VT}{Z}\right)\left(\frac{\partial Z}{\partial T}\right)_p \tag{D-7}$$

We used Dranchuk and Abou-Kassem (1975) equation-of-state to estimate Z factor and $\left(\frac{\partial Z}{\partial T}\right)_p$ in Eq. D-7. For non-ideal gas at moderate pressures, $1 - T\beta$ is usually negative (because β is much larger for gases than for liquids), making C_{JT} positive for gases. However, at high pressures, gases behave much like liquids and have negative C_{JT}.

APPENDIX E

Fully analytical solution of geothermal model

Define

$$\mathrm{M} = \frac{\mathrm{A_p}\rho_f c_f v_{fp}}{2\pi r_{ito} U_{ito}} = \frac{w c_f}{2\pi r_{ito} U_{ito}} \tag{E-1}$$

$$\mathrm{N} = \frac{A_i \rho_f c_f v_{fi}(K_e + r_{co} U_{co} T_D)}{2\pi r_{co} U_{co} K_e} = \frac{w c_f (K_e + r_{co} U_{co} T_D)}{2\pi r_{co} U_{co} K_e} \tag{E-2}$$

Eq. 49 and Eq. 50 can be expressed as:

$$\frac{\mathrm{dT_p}}{dz} = \frac{1}{M}(T_p - T_i) \tag{E-3}$$

$$N\frac{dT_i}{dz} = \frac{N}{M}\left(T_p - T_i\right) + (T_{ei} - T_i) \tag{E-4}$$

Plugging Eq. E-3 into Eq. E-4 to eliminate T_i:

$$MN\frac{d^2 T_p}{dz^2} + M\frac{dT_p}{dz} - T_p + T_{ei} \tag{E-5}$$

Considering $\mathrm{T_{ei}} = T_{eio} + g_G z$, a particular solution of Eq. E-5 can be obtained:

$$\widehat{T_p} = g_G z + T_{eio} + M g_G \tag{E-6}$$

The homogeneous solution of Eq. E-5 is in the form of :

$$\bar{T}_p = \alpha e^{\lambda_1 z} + \beta e^{\lambda_2 z} \tag{E-7}$$

λ_1 and λ_2 are obtained by solving the characteristic equation:

$$MN\lambda^2 + M\lambda - 1 = 0 \tag{E-8}$$

Where

$$\lambda_1 = -\frac{1}{2N} + \frac{1}{2N}\sqrt{1 + \frac{4N}{M}} \tag{E-9}$$

$$\lambda_2 = -\frac{1}{2N} - \frac{1}{2N}\sqrt{1 + \frac{4N}{M}} \tag{E-10}$$

The complete solution is:

$$T_p = \alpha e^{\lambda_1 z} + \beta e^{\lambda_2 z} + M g_D + T_{ei} \tag{E-11}$$

$$T_i = (1 - \lambda_1 M)\alpha e^{\lambda_1 z} + (1 - \lambda_2 M)\beta e^{\lambda_2 z} + T_{ei} \tag{E-12}$$

Where α and β can be obtained by incorporating the boundary conditions shown in Eq. E-13 and E-14.

$$\alpha = -\left[\frac{(T_{in} - T_{eio})\lambda_2 e^{\lambda_2 L} + g_G(1 - \lambda_2 M)}{\lambda_1 e^{\lambda_1 L}(1 - \lambda_2 M) - \lambda_2 e^{\lambda_2 L}(1 - \lambda_1 M)}\right] \tag{E-13}$$

$$\beta = \frac{(T_{in} - T_{eio})\lambda_1 e^{\lambda_1 L} + g_G(1 - \lambda_1 M)}{\lambda_1 e^{\lambda_1 L}(1 - \lambda_2 M) - \lambda_2 e^{\lambda_2 L}(1 - \lambda_1 M)} \tag{E-14}$$